MULTISCALE POROUS FUEL CELL ELECTRODES

By

Hao Wen

A DISSERTATION

Submitted to
Michigan State University
in partial fulfillment of the requirements
for the degree of

DOCTOR OF PHILOSOPHY

Materials Science and Engineering

2012

ABSTRACT

MULTISCALE POROUS FUEL CELL ELECTRODES

By

Hao Wen

Porous electrodes are widely used in fuel cells to enhance electrode performance due to their high surface area. Increasingly, such electrodes are designed with both micro-scale and nano-scale features. In the current work, carbon based porous materials have been synthesized and utilized as bioelectrode support for biofuel cells, analysis of such porous electrodes via rotating disk electrode has been enhanced by a numerical model that considers diffusion and convection within porous media. Finally, porous perovskite metal oxide cathodes for solid oxide fuel cell have been modeled to simulate impedance response data obtained from symmetric cells.

Carbon fiber microelectrodes (CFME) were fabricated to mimic the microenvironment of carbon fiber paper based porous electrodes. They were also miniature electrodes for small-scale applications. As observed by scanning electron microscopy (SEM), carbon nanotubes (CNTs) formed a homogeneously intertwined matrix. Biocatalysts can fully infiltrate this matrix to form a composite, with a significantly enhanced glucose oxidation current - that is 6.4 fold higher than the bare carbon fiber electrodes.

Based on the CNT based porous matrix, polystyrene beads of uniform diameter at 500 nm were used as template to tune the porous structure and enhance biomolecule transport. Focused ion beam (FIB) was used to observe the morphology both at the surface and the cross-section. It has been shown that the template macro-pores enhanced the fuel transport and the current density has been doubled due to the improvement.

Like commonly used rotating disk electrode, the porous rotating disk electrode is a system with analytically solved flow field. Although models were proposed previously with first order kinetics and convection as the only mass transport at high rotations, some recent findings indicated that diffusion could play an important role at all disk rotation rates. In the current proposed model, enzymatic kinetics that follow a Ping Pong Bi Bi mechanism was considered, diffusional transport included, and the electrolyte transport of substrate outside the porous media discussed as well.

Composite solid oxide fuel cells have good power generation due to enhanced ion conductivity in the cathode achieved by inclusion of high oxygen ion conductivity materials. Impedance spectroscopies of such cathodes were modeled to study the underlying transport and kinetic mechanisms. The effects of electronic conductor loading were studied, including loading values below the percolation threshold. The conductivity and oxygen surface exchange reaction rate were fitted to experimental data and percolation theory was utilized to explain the fitted trends.

DEDICATED
TO
FRIENDS AND FAMILY

ACKNOWLEDGEMENTS

I still remember the old days when I was a four-year old little boy. My mother's biggest pride was to have his son become a scientist someday. As I grow up, gradually as I learned, being a scientist means being able to think critically, sensing the possible from unknown wilderness, and work hard to transfer ideas to realities. Since then, getting higher education to become one of the scientific pioneers has always been my dream of life.

I would like to thank Dr. Andre Lee, who accepted me to Department of Chemical Engineering and Materials Science in 2006. The dream would not have become true without his kindness.

The acceptance to graduate school is only halfway towards the doctoral degree. Dr. Scott Calabrese Barton has been a fabulous advisor to me. He is patient, supportive, and diligent as a role model to me. I am especially thankful for his support when my research was in a stalemate and when I am looking for jobs. He is also a very good friend. I enjoyed the time spent in his lovely home with his family and friends.

Teamwork is essential to get things done in the lab. I want to take this opportunity to thank my colleagues Deboleena Chakraborty, Vijayadurga Nallathambi, Hanzi Li, Harshal Bambhania, and Nate Leonard for being such great co-workers. The unforgettable moments we spent together are among most valuable treasures I earned in graduate school. I also would like to thank undergraduate student Erik McClellan for fabricating and testing the electrodes for me.

I want to thank department staff members JoAnn Peterson, Lauren Brown, Donna Fernandez, Jennifer Peterman and Nicole Shook. You all did a wonderful job helping me out on all the order forms, room reservations, travel reimbursements and appointment letters. I could focus on research because you took care of the rest so well. Thank you all so much.

I also would like to thank all my friends in MSU. You are the gems that make my life here shiny. Lei Zhang, you are the best roommate I ever had. A drink with you leaves all the troubles behind and put smiles on me again. Rui Lin, you are the one asking me out for a dinner to comfort me from the distress of experimental failure. Thank you for being so considerate and heart-warming. I am also truly happy for your marriage, and sincerely hope you have a wonderful life ahead.

All of you made my doctoral life and study in Michigan State University a truly amazing experience. Thank you.

TABLE OF CONTENTS

LIST OF TABLES

LIST OF FIGURES

Chapter 1 Introduction

1.1 Overview

Energy consumption is essential to modern human life, and sustainable energy supply is crucial for long-term stability of human societies. Fossil fuels, including crude oil, coal, and gas, currently providing more than 80 % of global energy.[1] Unfortunately, fossil fuels are not considered to be sustainable energy sources. Due to limited supply regions and possible depletion of current known reserves, the consumption of fossil fuels have led to geopolitical issues and military conflicts.[2–4] It has been predicted that coals can last to year 2112, and may also be the only fossil fuel available after 2042.[5] Moreover, greenhouse gas emissions from fossil fuel combustion have been connected to climate change and other concerns.[1] Renewable energy sources, such as wind power, solar, geothermal, and tidal action are possible solutions to those challenges.

Fuel cells are electrochemical devices that generate power from a continuous supply of fuel and oxygen. Fuel cells produce no greenhouse gas emissions if hydrogen is used as fuel, and are thus efficient to utilize renewable energy sources like hydrogen and other hydrocarbons including conventional fossil fuels.[6] Besides, glucose, plant saps, and juices could also be used as renewable fuels for biofuel cells.[7] Fuel cells have been developed for applications ranging from portable devices to automotive power sources ever since their invention by William Grove in 1891.[8]

Commercialization of fuel cells has accelerated during the past 10 years. Based on the report by Fuel Cell Review, the total shipment of fuel cell units has increased more than 20 fold to over 285,000 in year 2011 comparing to year 2007.[9] The total power capacity shipped increased by more than two fold to 86.2 MW comparing to 2007, since the majority of increased units are portable devices. The power density of fuel cells has increased significantly during this period of time. For example, catalyst utilization in polymer electrolyte membrane fuel cell (PEMFC) has improved from 2.8 kW/g in 2008 to 5.6 kW/g in 2011, as reported by the U.S. Department of Energy's annual progress report.[10]

Depending on the electrolyte and catalyst, common fuel cell platforms can be categorized as solid oxide fuel cell (SOFC, electrolyte), biofuel cell (catalyst), direct methanol fuel cell (DMFC, fuel), polymer electrolyte membrane fuel cell (PEMFC, electrolyte) etc.[11] This work focuses on the porous electrode utilized in biofuel cells and SOFCs.

SOFCs are usually electrochemically active at temperatures above 500 °C and rely on oxygen ion conduction within perovskite crystals to transport charge within electrolyte.[12] Figure 1.1 shows a general scheme of SOFCs. The high operating temperature is comparable to automotive engines and thus it is considered a promising transportation power source.[13] The all-solid feature leads to very good flexibility in cell-design, including tubular, planar, and corrugated structures.[14–16] The SOFC oxygen reduction cathode, which usually consists of composite of mixed ionic and electronic conductor (MIEC) and ionic conductor (IC), contributes the most to resistance losses in operating cells.[17] It is therefore important to understand the mechanisms of reaction and transport within composite cathodes, find rate-limiting steps, and develop new designs to improve cathode efficiency.

Biofuel cells are fuel cell devices that utilize biocatalysts to conduct electrochemical conversions.[7,18,19] Two main types of biocatalysts are reported in literature: enzymes and microbes. Microbial fuel cells have relatively long stability and fuel efficiency, but mass transfer through cell membranes significantly limits power output. They are primarily applicable in wastewater treatment facilities to decompose organic chemicals. Enzymatic fuel cells, without the mass transfer limitation found in microbial fuel cells, produce much higher power density, and are thus applicable in smaller-scale electronic devices.[7] They are active at room temperature and neutral pH, and are reactant selective, leading to minimal device complexity, lower cost and smaller size.[7] Major challenges in such electrodes include the low power output and long term stability, which are both due to limited enzyme loading, enzyme stability and electron transfer.[20]

Porous electrodes greatly increase available surface area for heterogeneous electrochemical reactions within given electrode volumes, and thus is an essential feature in any commercially viable fuel cells.[21–24] Important characteristics of a porous support include the surface area per unit volume, hydrophilicity, pore size distribution, stability and biocompatibility (for biofuel cells).[7] Carbon materials such as chitosan scaffold,[25–27] carbon nanotube,[23,28,29] graphite platelets,[30,31] and activated carbon,[32] are intensively studied as porous bioelectrode support due to their superior physical and electrochemical properties. In this work, carbon nanotubes were used as porous support, and bioelectrodes thus fabricated were studied.

Modeling of fuel cells in this work focuses on single working electrodes instead of complete cells, since experiments on single electrodes are easily conducted, and analysis of individual components enhances the understanding of underlying mechanisms. The inputs to the models can be generalized as kinetics, transport, and structure/morphology; and the outputs to be current, power, and cost. Optimization efforts usually focus on porous media geometry, porosity;[33–36] enzymatic or microbial catalyst activity;[37–39] and reactant supply conditions.[40–42]

1.2 Porous electrodes as support for bioelectrodes

Typical biomolecules, like glucose oxidase, which is a dimer, have dimensions of 5 nm × 8 nm,[43] thus mesoporous materials with pore size larger than 10 nm are suitable for bioelectrodes. Large pore size allows transport of biomolecules around 10 nm and provides large surface area. Various carbon materials with such pore sizes have been utilized as supports due to carbon's biocompatibility and stability under wide range of temperature and solutions.[26,44,45] The porosity of these supports are usually above 70% so that reasonable amount of catalyst can be immobilized within the electrode volume.[23,26,46] Carbon nanotubes have been intensively studied due to their superior electrochemical and physical properties.[44,47,48] They have been modified to become hydrophilic,[45,49] and/or prepared into fibers or conductive mats.[50] Carbon nanotubes can be made hydrophilic by plasma oxidation under oxygen atmosphrere,[50] by polymer wrapping,[45,51,52] by surfactant,[26,45,53] or by acid treatment.[47,52,54]

Besides CNTs, other carbon forms were also found in literature.[26,55–63] Carbon nanoballs treated with plasma was used for oxygen reduction cathodes and batteries.[64,65] Carbonaceous foam monoliths with interconnected hierarchical porosity were used for mediated glucose oxidation anodes or lithium ion negative electrodes.[60,66] Exfoliated graphite nano-platelets were coated on glassy carbon electrodes to form porous layer as support for glucose biosensors.[31]

Composite porous supports with shape controlling components have been extensively reported.[67,68] The shape controlling component may not even be conductive. Chitosan is a commonly used pore forming structural support. Its hydrophobicity can be tuned with pH, thus enabling well-dispersion with CNTs, and its macropore forming properties in combination with the mechanical and electrical properties of NTs have resulted in many interesting applications.[26] For example, chitosan were doped with CNTs for bioelectrodes.[25,26] Carbon nanofiber / room temperature ionic liquid / chitosan composites could provide a suitable micro-environment for glucose oxidase electron transfers.[25] Other pore forming agents like non-conducting polycarbonate membranes were used as scaffold to coat conductive biocatalysts.[35,69,70]

1.3 Porous electrode models

Porous electrodes were first modeled as "macrohomogenous", in which all physical properties such as porosity and surface area per unit volume were considered to be average quantities throughout the electrode.[71,72] Based on this idea, specific models were discussed for various types of fuel cell electrodes, such as SOFC,[73–77] PEMFC,[78–80] or bioelectrodes.[81–84]

1.4 Modeling of porous composite SOFC oxygen reduction cathode

In a typical porous SOFC oxygen reduction composite cathode, oxygen diffuses into the electrode, and electrons from the current collector conduct through mixed ionic and electronic conductor (MIEC), and ionic conductor (IC), which is the same material as electrolyte, transports oxygen vacancies (or equivalently, oxygen ions).[85] Figure 1.1 shows the scheme of a micron-scale IC scaffold with nano-scale MIEC catalyst particles. At the active sites, oxygen exchange reaction happens with oxygen vacancy, electron, and oxygen gas molecules:

$$\frac{1}{2}O_2\left(g\right)+2e^-+V_O^{\infty}\rightarrow O_O^x \qquad (1)$$

To fabricate such electrodes, micron scale ionic conductor scaffolds are first prepared by partial sintering of IC/polymer compact on IC dense electrolyte. MIEC nanoparticles are then formed via multiple infiltration of aqueous MIEC precursor solution into IC porous scaffold and form a continuous phase.[17,86–88] The cathode performance is usually measured with a symmetric cell setup, where both sides of electrolyte layer are coated with cathode materials.[17,89,90] The symmetric cell setup eliminates the need for a reference electrode while still able to control the potential at zero in the symmetric center. Thus it is convenient to estimate the cathode performance by simply divide the measured responses by two, like polarization resistance read from electric impedance spectroscopy.

Impedance responses from symmetric cells are obtained by applying sinusoidal potential perturbations, and recording the resulting transient currents. Such responses at varying perturbation frequencies, ranging from 0.01 Hz to 100 kHz, constitute electrochemical impedance spectroscopy (EIS).[17,87,91] EIS is unique in its ability to deconvolute multiple electrochemical and physical processes by distinguishing between characteristic time constants. EIS can be recorded at either open circuit or under biased (nonzero current) conditions. The symmetric cell setup is suitable for open-circuit measurements since the electrochemical reactions on both sides of the cell result from the same reaction in exactly opposite directions, thus the contributions from either side of the cell is exactly half of the measured values, and the potential at the center of the electrolyte can thus be considered fixed at 0 V without perturbation, providing great convenience as a reference point.[87,91] EIS under direct current bias to study cathode processes were measured for non-symmetric cells in which only the cathode process was rate-limiting.[92,93] For example, anode-supported thin film cathodes were studied with an equivalent circuit model by Baumann, where low, medium, and high frequency impedance were separately defined to delegate different rate-limiting processes with varying time constants.[92] Huang studied cathode-supported tubular micro-porous electrodes which were measured at varying DC biases, along with oxygen concentration and diffusivity variation, to reveal the gas diffusion impedances.[93,94] It was generally observed that DC bias would lead to reduced polarization resistances due to kinetic activations.

Modeling of SOFC fuel cells has been extensively reported.[40,74,76,95–98] Usually only the electrode has been studied, but Schneider and Shi found that the oscillation of reactant concentration within flow channel could contribute to impedance measurement too.[41,99–101] Gorte attempts to explain transient responses for composite cathode prepared with infiltration technique, but no model was proposed to calculate EIS or compared directly to experimental EIS in Nyquist or Bode plots.[102] In the current work, we focus on two major models that gave reasonable explanation of EIS data: Nicholas' SIMPLE model, and Adler's model, as discussed below.

By considering all the ion transport and oxygen surface exchange reaction as purely ohmic processes,[103] Nicholas proposed a Simple Infiltrated Microstructural Polarization Loss Estimation (SIMPLE) model to interpret EIS data for infiltrated SOFC electrodes at open circuit.[87] Experimental EIS data at open circuit were interpreted in terms of overall polarization resistance, R_p . By using kinetic parameters from simplified thin film electrode experiments,[92,104–107] the SIMPLE model can predict polarization resistance R_p within 30% from that reduced from EIS. However, this model discards information associated with the entire EIS spectrum, and is applicable only at open circuit.

Adler has attempted to correlate EIS to SOFC electrochemical processes.[108–111] The system is an infinitely thick cathode made only of MIEC, and poised at open circuit, thus enabling analytical solution, as shown in Figure 1.2. The only rate limiting steps are the oxygen surface exchange reaction and oxygen ion conduction.[112] These assumptions result in EIS spectra similar to Gerisher type responses.[113] In a Gerisher impedance, the electrochemical surface reaction is preceded with a homogeneous phase (or porous media) chemical reactions.

Thus Adler and Gerisher model are mathematically equivalent. Experimental EIS validates that, for most of the cases, the aforementioned assumptions are reasonable. However, the model breaks down at low MIEC loading in composite electrodes, and at high temperatures above 650 ˚C where gas diffusion becomes a rate-limiting step.

1.5 Three-dimensional reconstruction of porous media

Transport properties of fuel or oxygen within porous media are directly related to the detailed structure, including porosity, tortuosity and pore shapes. Simple approximations to estimate those properties, such as Bruggeman's equation,[71] are useful but do not consider detailed morphology. More precise methods are available to reconstruct the internal three-dimensional structure and numerically solve for the effective diffusivities, conductivities, and even distribution of triple phase boundaries.

Focused ion beam / scanning electron microscopy (FIB-SEM) has been used to reconstruct three-dimensional structure porous media, which greatly enhanced the precision of ion and gas transport modeling.[114–121] In such experiments, the porous structures were infiltrated with resin to strengthen the structure and increase the imaging contrast between pore space and original scaffold materials.[122] Ion beams slice off the structure, revealing cross sections at nanometer scale steps to be recorded. With hundreds of such revealed cross sections, the three-dimensional structure can thus be reconstructed. Resolution is dependent on the slicing step size and image contrast between resins and original structures. A major disadvantage is the destructive nature of this technique, thus it is not suitable for *in-situ* experiments or making comparisons before and after other experiments.

A non-destructive technique, X-ray computerized tomography (XCT), largely compliments the FIB technique.[123–127] In XCT, the X-ray attenuation is recorded at different incoming beam angles, which produces data that can be computerized as 2-D images. Large sequences of these 2-D images may be further assembled into 3-D reconstructions. Compared to FIB tomography, XCT is generally lower in resolution, and its image contrast is limited by X-ray interaction with the material.[121] One major advantage of XCT is the capability to conduct elemental mapping and *in-situ* experiments. In combination with FIB as a shaping tool, high resolution reconstructions with elemental mapping have been obtained for various structures.[128,129]

1.6 Modeling of porous electrodes for biocatalysis

The general modeling processes have been shown in Figure 1.4. The inputs include electrode geometry, kinetic information, and transport properties. Numerical model results can be fitted to experiment, allowing for fitting of model parameters. Based on such calculations, design and optimization of porous electrodes can be conducted.

Porous electrodes for biocatalysis have been modeled in both biofuel cells and single working electrodes.[39,130–138] Biocatalysis in such electrode system can proceed by either direct electron transfer (DET) or mediated electron transfer (MET), depending whether mediators are used.[7] The mass transport of oxygen and fuel substrate in porous media can be studied on mounted porous rotating disk electrodes (PRDE).[139,140] The PRDE configuration is useful since it has controllable mass transport within porous media. The PRDE model can calculate potential, rotation, and species transport dependences of steady-state current responses, thus providing fitting capability to find transport and kinetic parameters. Based on the knowledge obtained from modeling, the electrodes under study can be optimized for improved performances.

1.6.1 Characterization and determination of parameters

It is important to have precise parameter values so that actual rate-limiting steps can be identified, and associated constants can be fitted or studied. Parameter values are usually determined via simplified experimental setups, such as thin catalyst film electrode on flat rotating disk electrode (RDE) surface to focus on kinetics,[141] or porous electrode with a fast redox couple, like ferrocyanide / ferricyanide, to focus on mass transport.[142] However, these simplifications are not always valid, since biocatalysts are known to have kinetic properties which vary by orders of magnitude in varying hosting environments,[143,144] Mass transport of reacting species may also vary to great extents.[145–147]

1.6.2 Mediated electron transfer

The use of mediated electron transfer greatly enhanced the charge transfer between enzyme active sites and current collectors.[7] The choice of mediator considers biocompatibility, redox potential, stability, temperature, and toxicity. Viable mediators found in literature include the diffusional cofactor nicotinamide adenine dinucleotide (NAD^+),[148,149] 2,2'-azino-bis(3-ethylbenzothiazoline-6-sulphonic acid) (ABTS) for the oxygen-reducing laccase enzyme,[64,150] or c-type cytochromes in microbial systems utilizing microbes such as *Geobacter* or

Shewanella.[151] Very high performance for enzymatic electrodes can be obtained using mediators made of conductive redox polymers.[7,152–155] For example, osmium based redox polymer was used as mediator for glucose oxidation with glucose oxidase from *Aspergillus niger*.[156–159] Thus the current discussion will focus on such redox polymers.

Conductive redox polymers have been intensively studied as biocatalyst mediators.[38] Electronic conduction in organic chemicals happens via a mechanism termed "superexchange" by Tender,[160] or "electrical wiring" by Heller,[161,162] in which the electrons are conducted via hopping between adjacent redox centers. Comparing to metallic conduction, such hopping mechanisms require activation energy since electrons are localized on the active redox sites, instead of moving in a conduction band in a metal.[163] As such, electrons are transported at a slower rate, and concentration gradients of the oxidized and reduced species are possible.

Effective electron diffusivity (D_e) is a commonly used transport parameter for mediated electron transfer in redox polymers. In osmium-based redox polymers, D_e is in the order of $1\times10^{-9} cm^2 s^{-1}$.[38] Besides the diffusivity, the redox potential, and redox center concentration are also important to the modeling work. The redox potential can be tuned by polymer synthesis processes,[38,164] and characterized by fast scan cyclic voltammetry (CV).[38] Response of the system usually closely follows the typical semi-infinite diffusion with fast kinetics, which have already been well studied.[165] Redox center concentration can be obtained by metal detection techniques such as atomic absorption or inductively coupled plasma (ICP).[166] However, not all redox centers in the polymer are active. Active redox center concentration may be obtained by integrating a cyclic voltammogram (CV) scan peak. Once this concentration is known, effective diffusivity can be estimated through Randles-Sevcik relationship:[165]

$$i = 0.4463 n^{\frac{3}{2}} F^{\frac{3}{2}} C D_e^{\frac{1}{2}} R^{-\frac{1}{2}} T^{-\frac{1}{2}} \sqrt{v} \tag{2}$$

where i is current density, v is scan rate, n is electron equivalent, C is reactant concentration, R is gas constant, and T is temperature. Based on equation (2), diffusivity can be estimated by finding the linear slope between current density and square root of scan rate v. It is difficult, though, to obtain an accurate active redox center concentration. As mentioned before, the total active concentration can be estimated by integrating through the redox peak. To measure the hydrogel thickness, one could use confocal microscopy,[164] or atomic force microscopy.[167] However, the total polymer matrix volume is hard to evaluate since the formed hydrogel film thickness is not uniform and it is hard to find average thickness throughout a millimeter scale film. The inconsistent density between the edge and center due to precursor solution surface tension when polymer matrix was formed further complicated the issue.

1.7 Kinetics of biocatalyst

Redox enzymes exhibit multiple kinetic mechanisms, leading to complex reaction rate expressions. Oxygen-dependent redox enzymes such as glucose oxidase and laccase appear to follow the ping pong bi bi mechanism,[136] where the substrate and mediator take turns reacting with the enzyme at the active center. In the case of glucose oxidase, electrons from glucose reduce the enzyme, which then transfers electrons to an acceptor such as a mediator redox center. The mathematical expression for the reaction rate is:[130]

$$R = \frac{k_{cat}E}{1 + K_M / M_{red} + K_S / S} \tag{3}$$

where k_{cat} is turnover number, M_{red} and S are the concentration of reduced mediator and substrate respectively. K_M and K_S are Michaelis Menten constants for the mediator and substrate, respectively. The kinetic parameters are usually subject to fitting since they are usually very sensitive to micro-environment.[38,130,168]

1.7.1 Porous rotating disk electrode (PRDE)

In a traditional rotating disk electrode (RDE), a flat disk surface with known surface area are rotated at well-controlled rotation rate in aqueous electrolyte, electrochemical reactions occur at the flat surface, with reactant transported to the surface with analytically solvable fluid flow.[165] With fast kinetics, the electrochemical current is limited by mass transport of the reactant to the electrode surface, and is thus proportional to square root of rotation rate, as described by the Levich equation:[165,169]

$$i = 0.62nFAD^{\frac{2}{3}}\omega^{\frac{1}{2}}\nu^{-\frac{1}{6}}C \tag{4}$$

Porous rotating disk electrode (PRDEs) is constructed by attaching a thin disk made of porous media under study onto a flat RDE surface, coated with catalyst, and have electrochemical response measured under controlled conditions.[139,140] Depending on the porosity and rotation, the transport within the PRDE can be considered as only convection, only diffusion, or the combination of both. Low porosity with small pore size largely limits the hydrodynamic flow, leading to diffusion dominant transport.[170]

Porous rotating disk electrodes enable well-defined internal fluid flow and thus are suitable for studying mass transport within porous media. The fluid flow in such systems has been solved in 1950s,[171] and porous carbon electrode experiments have been constructed in 1980s to investigate mass transport by using ferrocyanide redox couples.[142] However, only Levich type responses (limiting current proportional to square root of rotation) have been observed, which is probably due to the fast kinetics of ferrocyanide redox reactions.

Analytical solution of this system is possible if the surface kinetics are first order with respect to the reactant and diffusion within the system is negligible comparing to convection:[172]

$$I_R = \frac{T_r^\infty}{1+T_r^\infty} = \frac{I_{\text{measure}}}{I_M} \tag{5}$$

where I_R is relative current, I_M is theoretical maximum current when there is no mass transport limitations:

$$I_M = \pi k_r c_\infty n F R^2 h \tag{6}$$

and T_r^{∞} is the reaction time versus residence time considering the flow field volume element entering PRDE from surface and exiting from the side:

$$T_r^{\infty} = \frac{2k\omega^2}{k_r \nu} \tag{7}$$

where k is permeability of the porous media, k_r is first order reaction constant, and ν is electrolyte kinematic viscosity. The current responses thus predicted follow a sigmoidal shape with increasing rotation. At low rotation, by considering diffusion in the PRDE, consistent performance as predicted for flat RDE by Levich equation has been derived.[140]

The original work by Nam et al. already gives multiple experimental results that prove the theory.[140] However, in a setup with carbonaceous monolith coated with glucose oxidase and redox polymer mediator, the observed rotation dependence showed large background that could be attributed to diffusion at all rotations.[60] The inclusion of universal diffusion is necessary to explain the observed trends in such systems.

Porous electrodes that are too thin wouldn't have concentration variations. For example, platinum based thin film porous electrode was observed to follow Levich trend.[173] Since the electrode is too thin, the largely increased surface area is only equivalent of a largely increased reaction constant at the surface. Similarly, when an inactive but very thin polyelectrolyte porous layer is coated on RDE, Levich trend can also be observed.[174]

1.7.2 Mass transport of fuels and oxygen

The transport of fuel and oxygen in porous media is usually treated as macro-homogeneous processes.[71,130] The effective diffusivity can be approximated with Knudsen diffusion accounting for pore geometry and porosity.[175] If porosity of the studied media is not readily available, Bruggman's approximation, $D_{eff} = D_0\varepsilon^{3/2}$, can be used, where ε is porosity.

Since the MET process requires two reactants for immobilized enzymes, it is necessary for the electron conduction and substrate transport to happen in a continuous phase, that is, both electron conduction phase and liquid phase should be above the percolation threshold. In the case of redox hydrogels, this is usually guaranteed since the polymer crosslinking ensured the continuity of mediator electron conduction paths. However, in case these two phases are randomly distributed, Rostokin studied the percolation properties of such multicomponent structures, and it was shown that multiple components of the porous media result in a decrease in current density.[131]

Transport can occur at multiple scales, including diffusion within catalytic film, through porous electrode layer, and even in flow-through channels if a complete fuel cell is modeled. Multiscale models, where the solution of one scale would be used as the source or sink term to a larger scale, can be used to obtain solutions.[130]

1.7.3 Optimization

For a porous electrode, typical design parameters include electrode thickness, porosity (geometry); enzyme reaction constants (kinetics) and flow rate, concentration, rotation rates (mass transport). Plots of these parameters versus current output may yield optimum values. Optimum thickness is a compromise between the total amount of active sites (thicker) and mass transport (thinner). It is useful to study the profile of substrate and mediator concentration along electrode thickness, thus revealing the efficiency of catalyst usage. Other geometry dimensions, such as pore size, porosity is also the focus of optimization.[130] Feeding volumetric flow rate, concentration and/or rotation rate optimization is pursued as mass transport controlling operating conditions.

1.8 Overview of dissertation

The goal of the current work is to study porous materials as supports for fuel cell electrodes. In Chapter 2, carboxylated carbon nanotubes were coated on carbon fiber microelectrode to serve as support for glucose oxidation biocatalysis. The thickness of CNT coating and hydrogel coating were optimized. The geometry of CNT coating was investigated with SEM. Electrochemical response of mediator and glucose oxidation were characterized, and the CNT modified samples showed more than 6 fold increase in limiting current.

In Chapter 3, polystyrene (PS) beads were introduced to further improve the CNT porous support mentioned in Chapter 2. PS beads were available in monodispersed suspensions at uniform diameter of 500 nm. Heat treatment at 450 ˚C can fully remove PS while maintaining CNTs, as proved by TGA analysis.[176] Focused Ion Beam-SEM cuts through microfiber electrodes to reveal the cross section, indicating full infiltration of biocatalyst hydrogel into CNT matrix. PS introduced macropores at 500 nm, the same as the PS bead template, enhanced the accessible surface area and electrode limiting current by two fold.

In Chapter 4, a model for porous rotating disk electrodes was proposed, accounting for advection and diffusion at varying rotation speeds. This model explains the experimental observation of carbonaceous monolith macro-porous rotating disk electrodes coated with mediated glucose oxidase biocatalyst. The inclusion of mass transport outside of the porous media is also discussed.

In Chapter 5, an impedance model for SOFC composite oxygen reduction cathode was proposed. It was based on Adler's model accounting for charge-neutral processes such as diffusion of oxygen ion and oxygen surface exchange, but it also discussed the effect of low loading of MIEC in the composite cathode, which is supposedly below percolation threshold, resulting in significant reduction of MIEC conductivity and surface exchange reaction rate.

In summary, porous electrodes still remain a mainstay of battery and fuel cell development. The optimization of electrode materials such as carbon nanotubes, activated carbon, vitreous carbon and graphite for biocatalysis, or perovskite metal oxide ceramics for SOFCs can greatly improve cell performance. Porosity has large room for improvement as well. Multi-scale porosity, with macro-pore facilitating transport, mero- and micro- pores supplying large surface areas, is becoming the popular geometry for all kinds of fuel cells. The modeling of porous electrodes in biocatalysis and SOFC provide in-depth understanding of underlying mechanisms, and thus help to optimize electrode design.

1.9 Tables

Table 1.1 List of non-dimensional variables and parameters

Symbol	Definition
A	Area
C	Concentration
D	Diffusivity
D_e	Effective electron diffusivity
D_0	Bulk diffusivity
ε	Porosity
F	Faraday constant
i	Current
n	Number of electron transfer
ω	Rotation rate
ν	Kinematic viscosity
k	PRDE permeability
k_r	First order reaction rate
k_{cat}	Turnover number of enzyme
K_M	Ping Pong Bi Bi mediator reaction constant
M_{red}	Reduced mediator concentration
K_S	Ping Pong Bi Bi substrate reaction constant
E	Enzyme concentration
R	Gas constant
S	Substrate concentration
T	Temperature
T_r^{∞}	Reaction time versus residence time in PRDE
ω	PRDE rotation rate

1.10 Figures

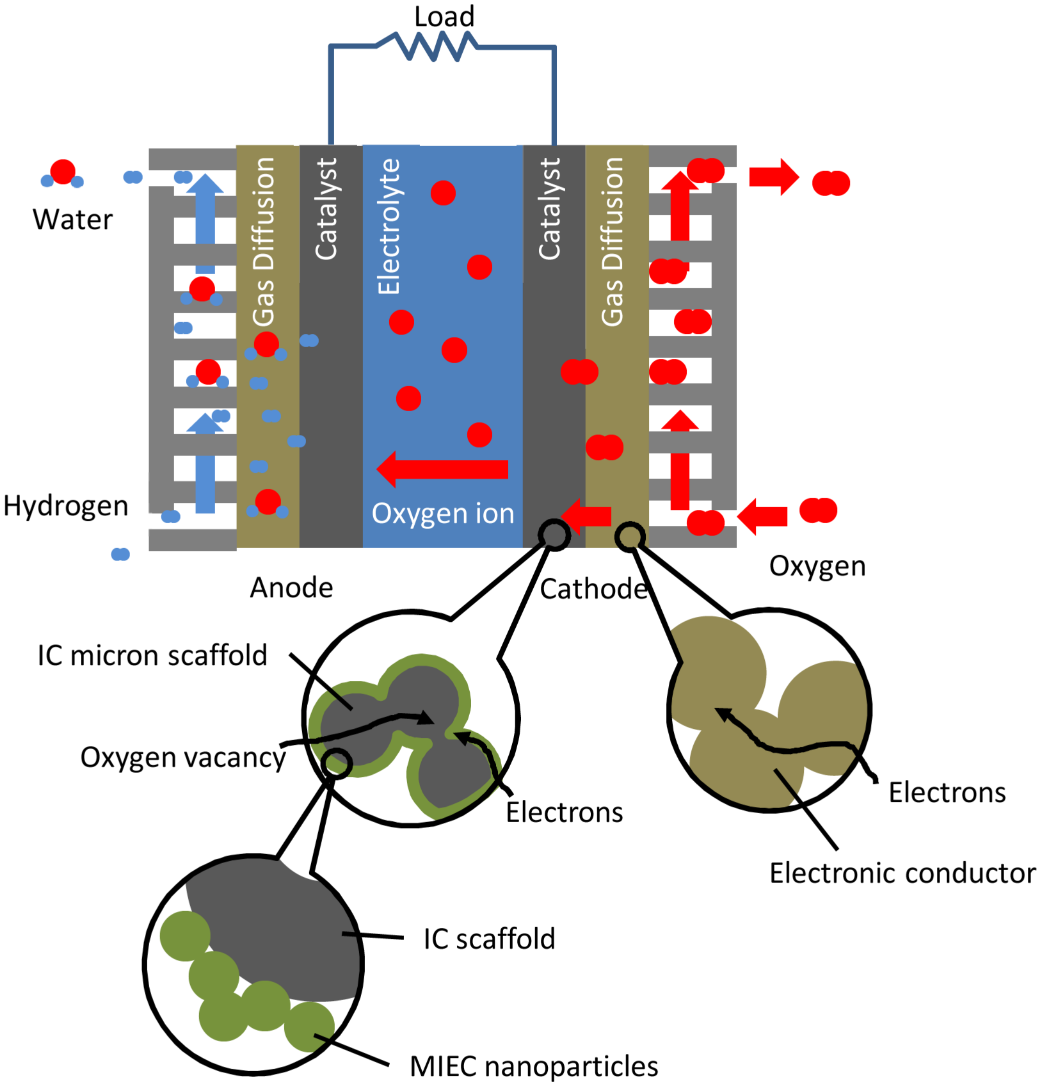

Figure 1.1 Solid oxide fuel cell scheme. (For interpretation of the references to color in this and all other figures, the reader is referred to the electronic version of this dissertation)

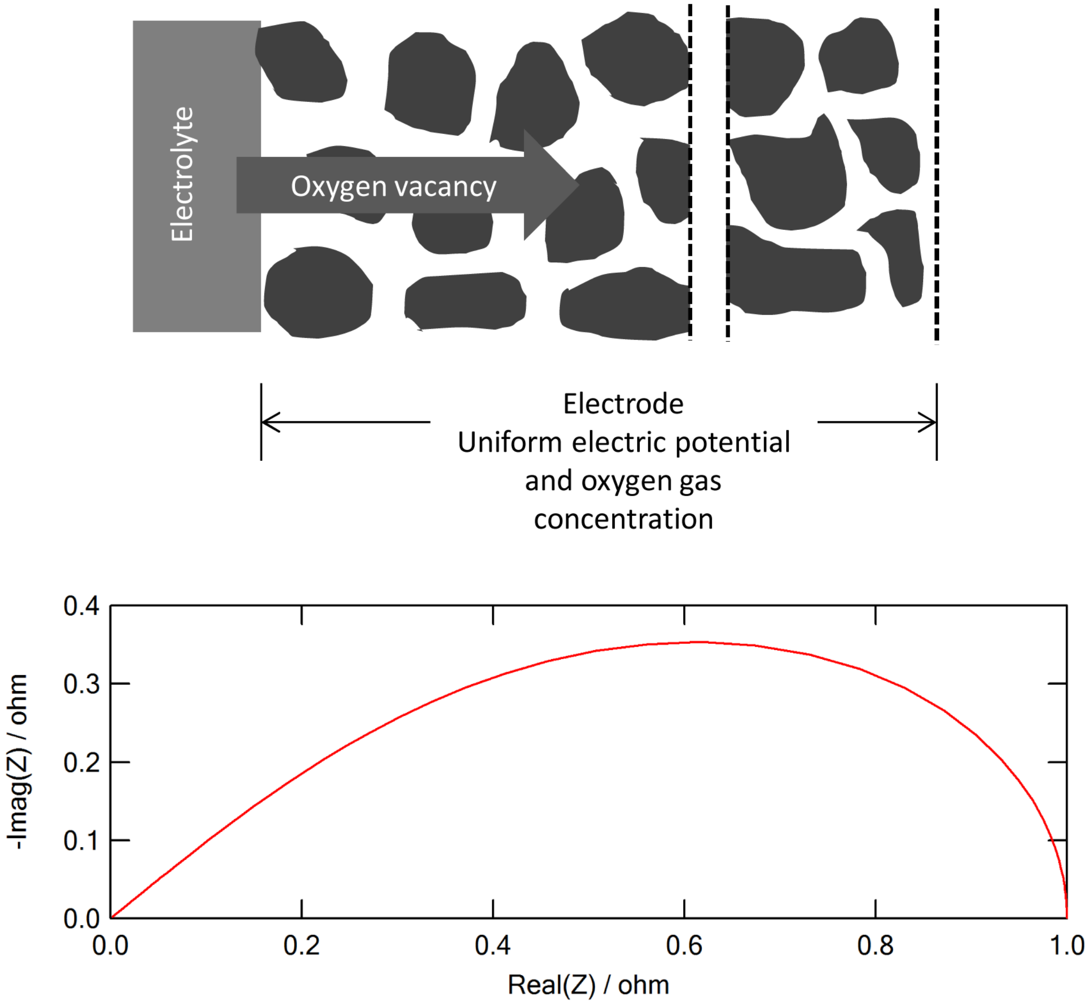

Figure 1.2 Adler's baseline SOFC cathode with mixed ionic and electronic conductor as the only cathode component.

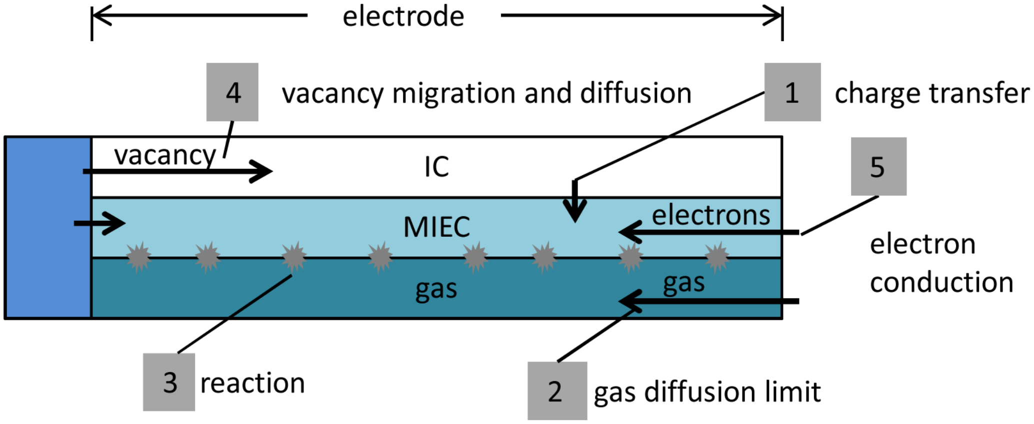

Figure 1.3 Electrochemical processes in a SOFC oxygen reduction cathode. IC stands for ionic conductor, MC stands for Mixed Ionic and Electronic Conductor.

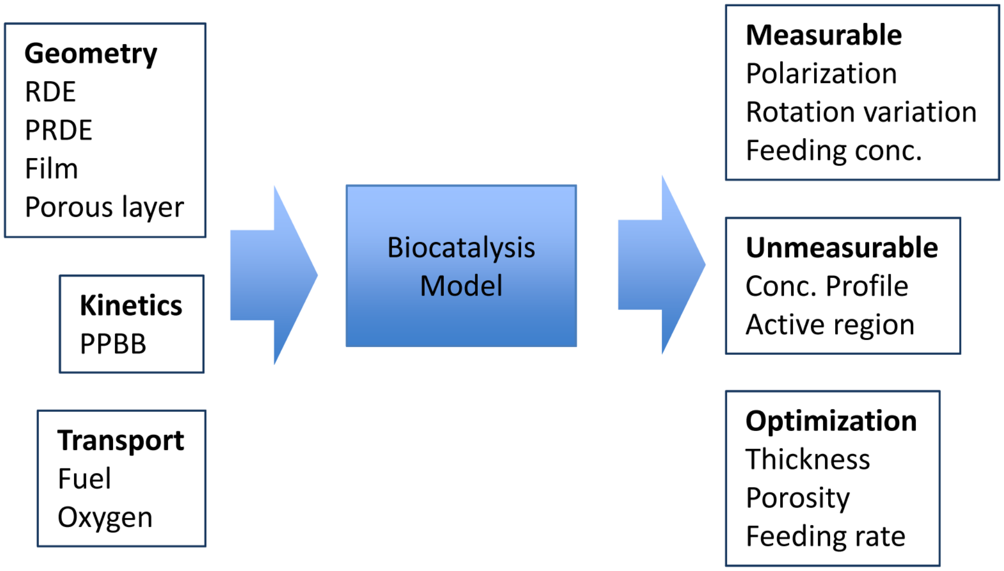

Figure 1.4 Scheme of modeling for porous electrode for biocatalysis. It is not absolutely impossible to measure those quantities, but they are usually hard to obtain.

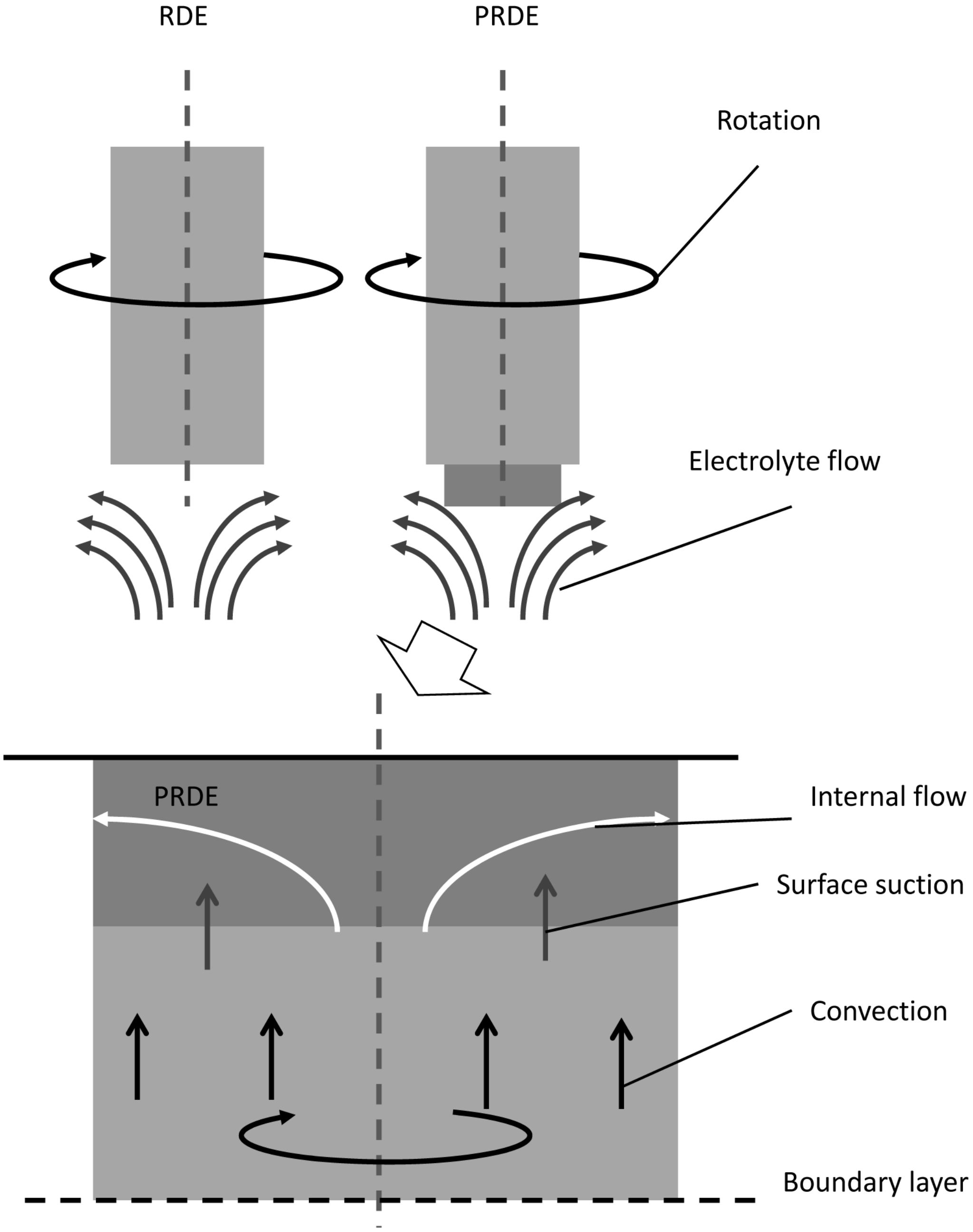

Figure 1.5 PRDE and RDE schemes

REFERENCES

References

1. M. Asif and T. Muneer, "Energy supply, its demand and security issues for developed and emerging economies" *Renewable and Sustainable Energy Reviews*, **11**(7), 1388-1413 (2007).

2. "U.S. Military Orders Less Dependence on Fossil Fuels - NYTimes.com" at <http://www.nytimes.com/2010/10/05/science/earth/05fossil.html?pagewanted=all>

3. "Military sees threats, worry in climate change — The Daily Climate" at <http://wwwp.dailyclimate.org/tdc-newsroom/2012/04/climate-security>

4. "U.S. Energy Information Administration (EIA)" at <http://www.eia.gov/>

5. S. Shafiee and E. Topal, "When will fossil fuel reserves be diminished?" *Energy Policy*, **37**(1), 181-189 (2009).

6. B. C.H.Steels, "Fuel-cell technology: Running on natural gas" *Nature*, **400**619-621 (1999).

7. S. Calabrese Barton, J. Gallaway and P. Atanassov, "Enzymatic Biofuel Cells for Implantable and Microscale Devices" *Chemical Reviews*, **104**(10), 4867-4886 (2004).

8. W.R. Grove, "On voltaic series and the combination of gases by platinum" *Philosophical Magazine and Journal of Science*, **14**127-130 (1839).

9. "The Industry Review 2011" at <http://www.fuelcelltoday.com/analysis/industry-review/2011/the-industry-review-2011>

10. "DOE hydrogen and fuel cells program: 2011 annual progress report" at <http://www.hydrogen.energy.gov/annual_progress11.html>

11. E. Ivers-Tiffee, A. Weber and H. Schichlein, "*Handbook of fuel cells, vol 2*" 587 (Wiley: Chichester, 2003).

12. J. Chen et al., "Nano-structured (La, Sr)(Co, Fe)O_3 +YSZ composite cathodes for intermediate temperature solid oxide fuel cells" *Journal of Power Sources*, **183**(2), 586-589 (2008).

13. N. Minh, "Solid oxide fuel cell technology - features and applications" *Solid State Ionics*, **174**(1-4), 271-277 (2004).

14. A. Tesfai, P. Connor, J. Nairn and J.T.S. Irvine, "Thermal Cycling Evaluation of Rolled Tubular Solid Oxide Fuel Cells" *Journal of Fuel Cell Science and Technology*, **8**(6), 061001 (2011).

15. S.-B. Sohn, S.-Y. Choi, G.-H. Kim, H.-S. Song and G.-D. Kim, "Stable sealing glass for planar solid oxide fuel cell" *Journal of Non-Crystalline Solids*, **297**(2-3), 103-112 (2002).

16. P.-C. Su, C.-C. Chao, J.H. Shim, R. Fasching and F.B. Prinz, "Solid oxide fuel cell with corrugated thin film electrolyte." *Nano letters*, **8**(8), 2289-92 (2008).

17. J.D. Nicholas and S. a. Barnett, "Measurements and Modeling of $Sm_{0.5}Sr_{0.5}CoO_{3-x}$–$Ce_{0.9}Gd_{0.1}O_{1.95}$ SOFC Cathodes Produced Using Infiltrate Solution Additives" *Journal of The Electrochemical Society*, **157**(4), B536 (2010).

18. I. Willner, Y.-M. Yan, B. Willner and R. Tel-Vered, "Integrated Enzyme-Based Biofuel Cells-A Review" *Fuel Cells*, **9**(1), 7-24 (2009).

19. Z. Du, H. Li and T. Gu, "A state of the art review on microbial fuel cells: A promising technology for wastewater treatment and bioenergy." *Biotechnology advances*, **25**(5), 464-82 (2007).

20. J. Kim, H. Jia and P. Wang, "Challenges in biocatalysis for enzyme-based biofuel cells." *Biotechnology advances*, **24**(3), 296-308 (2006).

21. V.V.N. Obreja, "On the performance of supercapacitors with electrodes based on carbon nanotubes and carbon activated material—A review" *Physica E: Low-dimensional Systems and Nanostructures*, **40**(7), 2596-2605 (2008).

22. V. Mehta and J.S. Cooper, "Review and analysis of PEM fuel cell design and manufacturing" *Journal of Power Sources*, **114**(1), 32-53 (2003).

23. H. Wen, H.M. Bambhania and S. Calabrese Barton, "Carbon nanotube-modified biocatalytic microelectrodes with multiscale porosity" *Journal of Applied Electrochemistry*, (2012).doi:10.1007/s10800-012-0381-9

24. N.P. Brandon and D.J. Brett, "Engineering porous materials for fuel cell applications." *Philosophical transactions. Series A, Mathematical, physical, and engineering sciences*, **364**(1838), 147-59 (2006).

25. Q. Sheng, R. Liu, J. Zheng, W. Lin and Y. Li, "Direct electrochemistry of glucose oxidase immobilized on porous carbon nanofiber/room temperature ionic liquid/chitosan composite film and its biosensing application" *Journal of Solid State Electrochemistry*, **16**(2), 739-745 (2011).

26. C. Lau, M.J. Cooney and P. Atanassov, "Conductive macroporous composite chitosan-carbon nanotube scaffolds." *Langmuir*, **24**(13), 7004-10 (2008).

27. J.-D. Qiu, H.-Y. Xie and R.-P. Liang, "Preparation of porous chitosan/carbon nanotubes film modified electrode for biosensor application" *Microchimica Acta*, **162**(1-2), 57-64 (2007).

28. J. Li, D. Kuang, Y. Feng, F. Zhang and M. Liu, "Glucose biosensor based on glucose oxidase immobilized on a nanofilm composed of mesoporous hydroxyapatite, titanium dioxide, and modified with multi-walled carbon nanotubes" *Microchimica Acta*, **176**(1-2), 73-80 (2011).

29. G. Mohanakrishna, S. Krishna Mohan and S. Venkata Mohan, "Carbon based nanotubes and nanopowder as impregnated electrode structures for enhanced power generation: Evaluation with real field wastewater" *Applied Energy*, 1-7 (2012).doi:10.1016/j.apenergy.2012.01.058

30. N. Oyama and F.C. Anson, "Catalysis of electrode processes by multiply-charged metal complexes electrostatically bound to polyelectrolyte coatings on graphite electrodes, and the use of polymer-coated rotating disk electrodes in diagnosing kinetic and conduction mechanisms" *Analytical Chemistry*, **52**(8), 1192-1198 (1980).

31. J. Lu, L.T. Drzal, R.M. Worden and I. Lee, "Simple Fabrication of a Highly Sensitive Glucose Biosensor Using Enzymes Immobilized in Exfoliated Graphite Nanoplatelets Nafion Membrane" *Chemistry of Materials*, **19**(25), 6240-6246 (2007).

32. V. Obreja, "On the performance of supercapacitors with electrodes based on carbon nanotubes and carbon activated material—A review" *Physica E: Low-dimensional Systems and Nanostructures*, **40**(7), 2596-2605 (2008).

33. G.S. Chai, I.S. Shin and J.-S. Yu, "Synthesis of Ordered, Uniform, Macroporous Carbons with Mesoporous Walls Templated by Aggregates of Polystyrene Spheres and Silica Particles for Use as Catalyst Supports in Direct Methanol Fuel Cells" *Advanced Materials*, **16**(22), 2057-2061 (2004).

34. F. Carn et al., "Inorganic monoliths hierarchically textured via concentrated direct emulsion and micellar templatesElectronic supplementary information (ESI) available: XRD profiles, nitrogen physisorption data and pore size distribution calculated from density functiona" *Journal of Materials Chemistry*, **14**(9), 1370 (2004).

35. A. Yu, Z. Liang and F. Caruso, "Enzyme Multilayer-Modified Porous Membranes as Biocatalysts" *Chemistry of Materials*, **17**(1), 171-175 (2005).

36. O.D. Velev and E.W. Kaler, "Structured Porous Materials via Colloidal Crystal Templating: From Inorganic Oxides to Metals" *Advanced Materials*, **12**(7), 531-534 (2000).

37. R. a Rincón et al., "Enzymatic fuel cells: Integrating flow-through anode and air-breathing cathode into a membrane-less biofuel cell design." *Biosensors & bioelectronics*, **27**132- 136 (2011).

38. J.W. Gallaway and S.A. Calabrese Barton, "Kinetics of redox polymer-mediated enzyme electrodes." *Journal of the American Chemical Society*, **130**(26), 8527-36 (2008).

39. C. Picioreanu, M.C.M. van Loosdrecht, T.P. Curtis and K. Scott, "Model based evaluation of the effect of pH and electrode geometry on microbial fuel cell performance." *Bioelectrochemistry (Amsterdam, Netherlands)*, **78**(1), 8-24 (2010).

40. W.G. Bessler, "A new computational approach for SOFC impedance from detailed electrochemical reaction–diffusion models" *Solid State Ionics*, **176**(11-12), 997-1011 (2005).

41. Y. Shi, H. Wang and N. Cai, "Direct two-dimensional electrochemical impedance spectra simulation for solid oxide fuel cell" *Journal of Power Sources*, **208**24-34 (2012).

42. W.M. Saltzman and R. Langer, "Transport rates of proteins in porous materials with known microgeometry." *Biophysical journal*, **55**(1), 163-71 (1989).

43. D. Rando, G.-W. Kohring and F. Giffhorn, "Production, purification and characterization of glucose oxidase from a newly isolated strain of Penicillium pinophilum" *Applied Microbiology and Biotechnology*, **48**(1), 34-40 (1997).

44. J. Chen, "Electrochemical characterization of carbon nanotubes as electrode in electrochemical double-layer capacitors" *Carbon*, **40**(8), 1193-1197 (2002).

45. S.K. Vashist, D. Zheng, K. Al-Rubeaan, J.H.T. Luong and F.-S. Sheu, "Advances in carbon nanotube based electrochemical sensors for bioanalytical applications." *Biotechnology advances*, **29**(2), 169-88 (2011).

46. S. Calabrese Barton, Y. Sun, B. Chandra, S. White and J. Hone, "Mediated Enzyme Electrodes with Combined Micro- and Nanoscale Supports" *Electrochemical and Solid-State Letters*, **10**(5), B96 (2007).

47. M. Terrones, W. Kuang, H. Harold and W.K. David, "Nanotubes : A Revolution in Materials Science and Electronics" *Current*, **199** (1999).

48. R.H. Baughman, A. a Zakhidov and W. a de Heer, "Carbon nanotubes--the route toward applications." *Science (New York, N.Y.)*, **297**(5582), 787-92 (2002).

49. H. Wen, V. Nallathambi, D. Chakraborty and S. Calabrese Barton, "Carbon fiber microelectrodes modified with carbon nanotubes as a new support for immobilization of glucose oxidase" *Microchimica Acta*, **175**(3-4), 283-289 (2011).

50. F. Gao, L. Viry, M. Maugey, P. Poulin and N. Mano, "Engineering hybrid nanotube wires for high-power biofuel cells" *Nature Communications*, **1**(1), 1-7 (2010).

51. J. Wang, M. Musameh and Y. Lin, "Solubilization of carbon nanotubes by Nafion toward the preparation of amperometric biosensors." *Journal of the American Chemical Society*, **125**(9), 2408-9 (2003).

52. S.-L. Shi, L.-Z. Zhang and J.-S. Li, "Electrical and dielectric properties of multiwall carbon nanotube/polyaniline composites" *Journal of Polymer Research*, **16**(4), 395-399 (2008).

53. X. Gong, J. Liu, S. Baskaran, R.D. Voise and J.S. Young, "Surfactant-Assisted Processing of Carbon Nanotube/Polymer Composites" *Chemistry of Materials*, **12**(4), 1049-1052 (2000).

54. K. Hernadi et al., "Catalytic synthesis and purification of carbon nanotubes" *Synthetic Metals*, **77**(1-3), 31-34 (1996).

55. E. Antolini, "Carbon supports for low-temperature fuel cell catalysts" *Applied Catalysis B: Environmental*, **88**(1-2), 1-24 (2009).

56. H. Chang, S.H. Joo and C. Pak, "Synthesis and characterization of mesoporous carbon for fuel cell applications" *Journal of Materials Chemistry*, **17**(30), 3078 (2007).

57. E. Frackowiak, "Carbon materials for the electrochemical storage of energy in capacitors" *Carbon*, **39**(6), 937-950 (2001).

58. J. Xiang and L.T. Drzal, "Thermal conductivity of exfoliated graphite nanoplatelet paper" *Carbon*, **49**(3), 773-778 (2011).

59. S. Flandrois and B. Simon, "Carbon materials for lithium-ion rechargeable batteries" *Carbon*, **37**(2), 165-180 (1999).

60. V. Flexer, N. Brun, R. Backov and N. Mano, "Designing highly efficient enzyme-based carbonaceous foams electrodes for biofuel cells" *Energy & Environmental Science*, **3**(9), 1302 (2010).

61. E.S. Steigerwalt, G. a. Deluga, D.E. Cliffel and C.M. Lukehart, "A Pt−Ru/Graphitic Carbon Nanofiber Nanocomposite Exhibiting High Relative Performance as a Direct-Methanol Fuel Cell Anode Catalyst" *The Journal of Physical Chemistry B*, **105**(34), 8097-8101 (2001).

62. X. Zhao, X. Lu, W.T.Y. Tze and P. Wang, "A single carbon fiber microelectrode with branching carbon nanotubes for bioelectrochemical processes." *Biosensors & Bioelectronics*, **25**(10), 2343-50 (2010).

63. H.R. Luckarift et al., "Facile Fabrication of Scalable, Hierarchically Structured Polymer/Carbon Architectures for Bioelectrodes." *ACS applied materials & interfaces*, (2012).doi:10.1021/am300048v

64. D.-J. Dai, D.-S. Chan and H.-S. Wu, "Modified Carbon Nanoball on Electrode Surface Using Plasma in Enzyme-Based Biofuel Cells" *Energy Procedia*, **14**1804-1810 (2012).

65. X. He, F. Wu and M. Zheng, "The synthesis of carbon nanoballs and its electrochemical performance" *Diamond and Related Materials*, **16**(2), 311-315 (2007).

66. N. Brun et al., "Hard Macrocellular Silica Si(HIPE) Foams Templating Micro/Macroporous Carbonaceous Monoliths: Applications as Lithium Ion Battery Negative Electrodes and Electrochemical Capacitors" *Advanced Functional Materials*, **19**(19), 3136-3145 (2009).

67. M. Dürr et al., "Low-temperature fabrication of dye-sensitized solar cells by transfer of composite porous layers." *Nature materials*, **4**(8), 607-11 (2005).

68. M. Tsionsky, G. Gun, V. Glezer and O. Lev, "Sol-Gel-Derived Ceramic-Carbon Composite Electrodes: Introduction and Scope of Applications" *Analytical Chemistry*, **66**(10), 1747-1753 (1994).

69. S. Suye, Y. Kumon and A. Ishigaki, "Immobilization of glucose oxidase on poly-(L-lysine)-modified polycarbonate membrane" *Biotechnology and Applied Biochemistry*, **27**(3), 245-245-248-248 (1998).

70. S. Myler, S. Eaton and S.P.. Higson, "Poly(o-phenylenediamine) ultra-thin polymer-film composite membranes for enzyme electrodes" *Analytica Chimica Acta*, **357**(1-2), 55-61 (1997).

71. J.S. Newman and K.E. Thomas-Alyea, "*Electrochemical systems*" 647 (Wiley-IEEE: 2004).

72. J. Newman and W. Tiedemann, "Porous-electrode theory with battery applications" *AIChE Journal*, **21**(1), 25-41 (1975).

73. H. Yakabe, M. Hishinuma, M. Uratani, Y. Matsuzaki and I. Yasuda, "Evaluation and modeling of performance of anode-supported solid oxide fuel cell" *Journal of Power Sources*, **86**(1-2), 423-431 (2000).

74. W. Bessler, S. Gewies and M. Vogler, "A new framework for physically based modeling of solid oxide fuel cells" *Electrochimica Acta*, **53**(4), 1782-1800 (2007).

75. S. Kakac, a Pramuanjaroenkij and X. Zhou, "A review of numerical modeling of solid oxide fuel cells" *International Journal of Hydrogen Energy*, **32**(7), 761-786 (2007).

76. X. Chen, "Simulation of a composite cathode in solid oxide fuel cells" *Electrochimica Acta*, **49**(11), 1851-1861 (2004).

77. a Pramuanjaroenkij, S. Kakac and X. Yangzhou, "Mathematical analysis of planar solid oxide fuel cells" *International Journal of Hydrogen Energy*, **33**(10), 2547-2565 (2008).

78. P.R. Pathapati, X. Xue and J. Tang, "A new dynamic model for predicting transient phenomena in a PEM fuel cell system" *Renewable Energy*, **30**(1), 1-22 (2005).

79. L. You and H. Liu, "A two-phase flow and transport model for the cathode of PEM fuel cells" *International Journal of Heat and Mass Transfer*, **45**(11), 2277-2287 (2002).

80. M. Hu, A. Gu, M. Wang, X. Zhu and L. Yu, "Three dimensional, two phase flow mathematical model for PEM fuel cell: Part I. Model development" *Energy Conversion and Management*, **45**(11-12), 1861-1882 (2004).

81. P. Kar, H. Wen, H. Li, S.D. Minteer and S. Calabrese Barton, "Simulation of Multistep Enzyme-Catalyzed Methanol Oxidation in Biofuel Cells" *Journal of The Electrochemical Society*, **158**(5), B580 (2011).

82. P. Zipp and H. Ahrens, "A model of bioelectrode motion artefact and reduction of artefact by amplifier input stage design" *Journal of Biomedical Engineering*, **1**(4), 273-276 (1979).

83. V. Desprez and P. Labbé, "A kinetic model for the electroenzymatic processes involved in polyphenol-oxidase-based amperometric catechol sensors" *Journal of Electroanalytical Chemistry*, **415**(1-2), 191-195 (1996).

84. A. Richardot and E.T. McAdams, "Harmonic analysis of low-frequency bioelectrode behavior." *IEEE transactions on medical imaging*, **21**(6), 604-12 (2002).

85. S. CARTER, "Oxygen transport in selected nonstoichiometric perovskite-structure oxides" *Solid State Ionics*, **53-56**597-605 (1992).

86. T.J. Armstrong and J.G. Rich, "Anode-supported solid oxide fuel cells with $La_{0.6}Sr_{0.4}CoO_{3-\lambda}$-$Zr_{0.84}Y_{0.16}O_{2-\delta}$ composite cathodes fabricated by an infiltration method" *Journal of The Electrochemical Society*, **153**(3), A515 (2006).

87. J.D. Nicholas and S. a. Barnett, "Finite-element modeling of idealized infiltrated composite solid oxide fuel cell cathodes" *Journal of The Electrochemical Society*, **156**(4), B458 (2009).

88. Y. Huang, J.M. Vohs and R.J. Gorte, "SOFC Cathodes Prepared by Infiltration with Various LSM Precursors" *Electrochemical and Solid-State Letters*, **9**(5), A237 (2006).

89. D.M. Bastidas, S. Tao and J.T.S. Irvine, "A symmetrical solid oxide fuel cell demonstrating redox stable perovskite electrodes" *Journal of Materials Chemistry*, **16**(17), 1603 (2006).

90. J.C. Ruiz-Morales, D. Marrero-López, J. Canales-Vázquez and J.T.S. Irvine, "Symmetric and reversible solid oxide fuel cells" *RSC Advances*, **1**(8), 1403 (2011).

91. J.D. Nicholas and S. a. Barnett, "Measurements and Modeling of $Sm_{0.5}Sr_{0.5}CoO_{3-x}$–$Ce_{0.9}Gd_{0.1}O_{1.95}$ SOFC Cathodes Produced Using Infiltrate Solution Additives" *Journal of The Electrochemical Society*, **157**(4), B536 (2010).

92. F. Baumann, J. Fleig, H. Habermeier and J. Maier, "Impedance spectroscopic study on well-defined (La,Sr)(Co,Fe)$O_{3-\delta}$ model electrodes" *Solid State Ionics*, **177**(11-12), 1071-1081 (2006).

93. K. Huang, "Gas-Diffusion Process in a Tubular Cathode Substrate of an SOFC" *Journal of The Electrochemical Society*, **151**(5), A716 (2004).

94. K. Huang, "Gas-Diffusion Process in a Tubular Cathode Substrate of a SOFC" *Journal of The Electrochemical Society*, **151**(5), H117 (2004).

95. W.G. Bessler, "Rapid Impedance Modeling via Potential Step and Current Relaxation Simulations" *Journal of The Electrochemical Society*, **154**(11), B1186 (2007).

96. S.. Chan, K.. Khor and Z.. Xia, "A complete polarization model of a solid oxide fuel cell and its sensitivity to the change of cell component thickness" *Journal of Power Sources*, **93**(1-2), 130-140 (2001).

97. J. Fleig, "SOLID OXIDE FUEL CELL CATHODES: Polarization Mechanisms and Modeling of the Electrochemical Performance" *Annual Review of Materials Research*, **33**(1), 361-382 (2003).

98. Q. Huang, R. Hui, B. Wang and J. Zhang, "A review of AC impedance modeling and validation in SOFC diagnosis" *Electrochimica Acta*, **52**(28), 8144-8164 (2007).

99. I.A. Schneider, D. Kramer, A. Wokaun and G.G. Scherer, "Oscillations in Gas Channels" *Journal of The Electrochemical Society*, **154**(8), B770 (2007).

100. I.A. Schneider, S.A. Freunberger, D. Kramer, A. Wokaun and G.G. Scherer, "Oscillations in Gas Channels" *Journal of The Electrochemical Society*, **154**(4), B383 (2007).

101. I.A. Schneider, M.H. Bayer, P. Boillat, A. Wokaun and G.G. Scherer, "Formation Of Low Frequency Inductive Loops In Polymer Electrolyte Fuel Cell (PEFC) Impedance Spectra Under Sub-Saturated Conditions" *ECS Transactions*, **11**461-472 (2007).

102. F. Bidrawn, R. Küngas, J.M. Vohs and R.J. Gorte, "Modeling Impedance Response of SOFC Cathodes Prepared by Infiltration" *Journal of The Electrochemical Society*, **158**(5), B514 (2011).

103. H. BOUWMEESTER, H. KRUIDHOF and A. BURGGRAAF, "Importance of the surface exchange kinetics as rate limiting step in oxygen permeation through mixed-conducting oxides" *Solid State Ionics*, **72**185-194 (1994).

104. F.S. Baumann et al., "Quantitative Comparison of Mixed Conducting SOFC Cathode Materials by Means of Thin Film Model Electrodes" *Journal of The Electrochemical Society*, **154**(9), B931 (2007).

105. F.S. Baumann et al., "Quantitative Comparison of Mixed Conducting SOFC Cathode Materials by Means of Thin Film Model Electrodes" *Journal of The Electrochemical Society*, **154**(9), B931 (2007).

106. F. Baumann, J. Fleig, H. Habermeier and J. Maier, "$Ba_{0.5}Sr_{0.5}Co_{0.8}Fe_{0.2}O_{3-\delta}$ thin film microelectrodes investigated by impedance spectroscopy" *Solid State Ionics*, **177**(35-36), 3187-3191 (2006).

107. J. Fleig et al., "Thin Film Microelectrodes in SOFC Electrode Research" *Fuel Cells*, **6**(3-4), 284-292 (2006).

108. S.B. Adler, "Factors governing oxygen reduction in solid oxide fuel cell cathodes." *Chemical Reviews*, **104**(10), 4791-843 (2004).

109. S. Adler, "Limitations of charge-transfer models for mixed-conducting oxygen electrodes" *Solid State Ionics*, **135**(1-4), 603-612 (2000).

110. S.B. Adler, "Electrode Kinetics of Porous Mixed-Conducting Oxygen Electrodes" *Journal of The Electrochemical Society*, **143**(11), 3554 (1996).

111. S.B. Adler, "Mechanism and kinetics of oxygen reduction on porous $La_{1-x}Sr_xCoO_{3-\delta}$ electrodes" *Solid State Ionics*, **111**(1-2), 125-134 (1998).

112. Y. Lu, C. Kreller and S.B. Adler, "Measurement and Modeling of the Impedance Characteristics of Porous $La_{1-x}Sr_xCoO_{3-\delta}$ Electrodes" *Journal of The Electrochemical Society*, **156**(4), B513 (2009).

113. M.E. Orazem and B. Tribollet, "*Electrochemical Impedance Spectroscopy*" *Analysis*, (2008).

114. D. Gostovic, J.R. Smith, D.P. Kundinger, K.S. Jones and E.D. Wachsman, "Three-Dimensional Reconstruction of Porous LSCF Cathodes" *Electrochemical and Solid-State Letters*, **10**(12), B214 (2007).

115. J.R. Wilson et al., "Three-dimensional analysis of solid oxide fuel cell Ni-YSZ anode interconnectivity." *Microscopy and microanalysis : the official journal of Microscopy Society of America, Microbeam Analysis Society, Microscopical Society of Canada*, **15**(1), 71-7 (2009).

116. K.N. Grew and W.K.S. Chiu, "A review of modeling and simulation techniques across the length scales for the solid oxide fuel cell" *Journal of Power Sources*, **199**1-13 (2012).

117. J.R. Smith et al., "Evaluation of the relationship between cathode microstructure and electrochemical behavior for SOFCs" *Solid State Ionics*, **180**(1), 90-98 (2009).

118. D.N. Dunn and R. Hull, "Reconstruction of three-dimensional chemistry and geometry using focused ion beam microscopy" *Applied Physics Letters*, **75**(21), 3414 (1999).

119. P.R. Shearing, J. Golbert, R.J. Chater and N.P. Brandon, "3D reconstruction of SOFC anodes using a focused ion beam lift-out technique" *Chemical Engineering Science*, **64**(17), 3928-3933 (2009).

120. R.M. Langford, G. Dale, P.J. Hopkins, P.J.S. Ewen and A.K. Petford-Long, "Focused ion beam micromachining of three-dimensional structures and three-dimensional reconstruction to assess their shape" *Journal of Micromechanics and Microengineering*, **12**(2), 111-114 (2002).

121. A.J. Kubis, G.J. Shiflet, R. Hull and D.N. Dunn, "Focused ion-beam tomography" *Metallurgical and Materials Transactions A*, **35**(7), 1935-1943 (2004).

122. J. Joos, T. Carraro, A. Weber and E. Ivers-Tiffée, "Reconstruction of porous electrodes by FIB/SEM for detailed microstructure modeling" *Journal of Power Sources*, **196**(17), 7302-7307 (2010).

123. J.R. Izzo et al., "Nondestructive Reconstruction and Analysis of SOFC Anodes Using X-ray Computed Tomography at Sub-50 nm Resolution" *Journal of The Electrochemical Society*, **155**(5), B504 (2008).

124. L. Babout, E. Maire, J.Y. Buffière and R. Fougères, "Characterization by X-ray computed tomography of decohesion, porosity growth and coalescence in model metal matrix composites" *Acta Materialia*, **49**(11), 2055-2063 (2001).

125. L. Ruffino et al., "Using X-Ray Microtomography for Characterisation of Catalyst Particle Pore Structure" *The Canadian Journal of Chemical Engineering*, **83**(1), 132-139 (2008).

126. D. Lu, M. Zhou, J.H. Dunsmuir and H. Thomann, "NMR T2 distributions and two phase flow simulations from x-ray micro-tomography images of sandstones." *Magnetic resonance imaging*, **19**(3-4), 443-8 (2001).

127. N. Shikazono et al., "Numerical Assessment of SOFC Anode Polarization Based on Three-Dimensional Model Microstructure Reconstructed from FIB-SEM Images" *Journal of The Electrochemical Society*, **157**(5), B665 (2010).

128. G.J. Nelson et al., "Comparison of SOFC cathode microstructure quantified using X-ray nanotomography and focused ion beam–scanning electron microscopy" *Electrochemistry Communications*, **13**(6), 586-589 (2011).

129. P.R. Shearing, J. Gelb and N.P. Brandon, "X-ray nano computerised tomography of SOFC electrodes using a focused ion beam sample-preparation technique" *Journal of the European Ceramic Society*, **30**(8), 1809-1814 (2010).

130. S. Calabrese Barton, "Oxygen transport in composite mediated biocathodes" *Electrochimica Acta*, **50**(10), 2145-2153 (2005).

131. Y.G. Chirkov and V.I. Rostokin, "Computer Simulation of Porous Electrodes with Immobilized Enzymes : The Percolation Properties of Multicomponent Structures" *Russian Journal of Electrochemistry*, **38**(9), 1130-1138 (2002).

132. W. Su, W. Yan, Z. Su, Y. Liu and Y. Xu, "Simulation of flow through porous anode in MFC at higher power density" *Theoretical and Applied Mechanics Letters*, **2**(2), 022003 (2012).

133. J.R. Kim et al., "Porous anodes with helical flow pathways in bioelectrochemical systems: The effects of fluid dynamics and operating regimes." *Journal of Power Sources*, (2012).doi:10.1016/j.jpowsour.2012.03.040

134. M.J. Cooney, V. Svoboda, C. Lau, G. Martin and S.D. Minteer, "Enzyme catalysed biofuel cells" *Energy & Environmental Science*, **1**(3), 320 (2008).

135. W. Johnston, N. Maynard, B.Y. Liaw and M.J. Cooney, "In situ measurement of activity and mass transfer effects in enzyme immobilized electrodes" *Enzyme and Microbial Technology*, **39**(1), 131-140 (2006).

136. P.N. Bartlett and K.F.E. Pratt, "Theoretical treatment of diffusion and kinetics in amperometric immobilized enzyme electrodes Part I: Redox mediator entrapped within the film" *Journal of Electroanalytical Chemistry*, **397**(1-2), 61-78 (1995).

137. K. Ramanathan, R. Mehrotra, B. Jayaram, A.S.N. Murthy and B.D. Malhotra, "Simulation of Electrochemical Process for Glucose Oxidase Immobilized Conducting Polymer Electrodes" *Analytical Letters*, **29**(9), 1477-1484 (1996).

138. A. Blandino, M. Mac and D. Cantero, "Modelling and simulation of a bienzymatic reaction system co-immobilised within hydrogel-membrane liquid-core capsules" **31**556-565 (2002).

139. R.T. Bonnecaze, N. Mano, B. Nam and A. Heller, "On the Behavior of the Porous Rotating Disk Electrode" *Journal of The Electrochemical Society*, **154**(2), F44 (2007).

140. B. Nam and R.T. Bonnecaze, "Analytic Models of the Infinite Porous Rotating Disk Electrode" *Journal of The Electrochemical Society*, **154**(10), F191 (2007).

141. B.A. Gregg and A. Heller, "Redox polymer films containing enzymes. 1. A redox-conducting epoxy cement: synthesis, characterization, and electrocatalytic oxidation of hydroquinone" *The Journal of Physical Chemistry*, **95**(15), 5970-5975 (1991).

142. W.J. Blaedel and J. Wang, "Rotated porous carbon disk electrode" *Analytical Chemistry*, **52**(1), 76-80 (1980).

143. S. Gupta, L. Mukhopadhyay and S.P. Moulik, "Kinetics in microemulsion V . Glucose oxidase catalyzed oxidation of β-D-glucose in aqueous , micellar and water-in-oil microemulsion media" *Indian Journal of Biochemistry & Biophysics*, **40**(October), 340-349 (2003).

144. S. Nakamura, S. Hayashi and K. Koga, "Effect of periodate oxidation on the structure and properties of glucose oxidase." *Biochimica et biophysica acta*, **445**(2), 294-308 (1976).

145. T.R. Marrero and E.A. Mason, "Gaseous Diffusion Coefficients" *Journal of Physical and Chemical Reference Data*, **1**(1), (1972).

146. K. Malek and M.-O. Coppens, "Knudsen self- and Fickian diffusion in rough nanoporous media" *The Journal of Chemical Physics*, **119**(5), 2801 (2003).

147. B.Y.J.K. Gladden, "Diffusion in Supersaturated Solutions. II. Glucose Solutions" *Extrapolation*, **1**(1914), (1952).

148. G.T.R. Palmore, H. Bertschy, S.H. Bergens and G.M. Whitesides, "A methanolrdioxygen biofuel cell that uses NAD q -dependent dehydrogenases as catalysts : application of an electro-enzymatic method to regenerate nicotinamide adenine dinucleotide at low overpotentials" *Journal of Electroanalytical Chemistry*, 155-161 (1998).

149. H. Li, H. Wen and S. Calabrese Barton, "NADH Oxidation Catalyzed by Electropolymerized Azines on Carbon Nanotube Modified Electrodes" *Electroanalysis*, **24**(2), 398-406 (2012).

150. G.T.R. Palmore and H.-H. Kim, "Electro-enzymatic reduction of dioxygen to water in the cathode compartment of a biofuel cell" *Journal of Electroanalytical Chemistry*, **464**(1), 110-117 (1999).

151. S.M. Strycharz-Glaven, R.M. Snider, A. Guiseppi-Elie and L.M. Tender, "On the electrical conductivity of microbial nanowires and biofilms" *Energy & Environmental Science*, **4**(11), 4366 (2011).

152. N. Mano et al., "Oxygen is electroreduced to water on a “wired” enzyme electrode at a lesser overpotential than on platinum." *Journal of the American Chemical Society*, **125**(50), 15290-1 (2003).

153. F. Mao, N. Mano and A. Heller, "Long tethers binding redox centers to polymer backbones enhance electron transport in enzyme “Wiring” hydrogels." *Journal of the American Chemical Society*, **125**(16), 4951-7 (2003).

154. N. Mano, H.-H. Kim and A. Heller, "On the Relationship between the Characteristics of Bilirubin Oxidases and O 2 Cathodes Based on Their “Wiring”" *The Journal of Physical Chemistry B*, **106**(34), 8842-8848 (2002).

155. S. Calabrese Barton, H.-H. Kim, G. Binyamin, Y. Zhang and A. Heller, "The “Wired” Laccase Cathode: High Current Density Electroreduction of O_2 to Water at +0.7 V (NHE) at pH 5" *Journal of the American Chemical Society*, **123**(24), 5802-5803 (2001).

156. B. Szajáni, a Molnár, G. Klámar and M. Kálmán, "Preparation, characterization, and potential application of an immobilized glucose oxidase." *Applied biochemistry and biotechnology*, **14**(1), 37-47 (1987).

157. M.V. Pishko, A.C. Michael and A. Heller, "Amperometric glucose microelectrodes prepared through immobilization of glucose oxidase in redox hydrogels" *Analytical Chemistry*, **63**(20), 2268-2272 (1991).

158. G. Binyamin, "Stabilization of Wired Glucose Oxidase Anodes Rotating at 1000 rpm at 37°C" *Journal of The Electrochemical Society*, **146**(8), 2965 (1999).

159. H. Wen, "Conductive Redox Polymer Characterization by Glucose Oxidation Standard Operating Procedure" (2010).

160. S.M. Strycharz-glaven, R.M. Snider, A. Guiseppi-elie and L.M. Tender, "Environmental Science On the electrical conductivity of microbial nanowires and biofilms †" *Materials Research*, 4366-4379 (2011).doi:10.1039/c1ee01753e

161. A. Heller, "Electron-conducting redox hydrogels: Design, characteristics and synthesis." *Current opinion in chemical biology*, **10**(6), 664-72 (2006).

162. A. Aoki, R. Rajagopalan and A. Heller, "Effect of quaternization on electron diffusion coefficients for redox hydrogels based on poly(4-vinylpyridine)" *The Journal of Physical Chemistry*, **99**(14), 5102-5110 (1995).

163. N.S. Malvankar, M.T. Tuominen and D.R. Lovley, "Comment on “On electrical conductivity of microbial nanowires and biofilms” by S. M. Strycharz-Glaven, R. M. Snider, A. Guiseppi-Elie and L. M. Tender, Energy Environ. Sci., 2011, 4, 4366" *Energy & Environmental Science*, **5**(3), 6247 (2012).

164. D. Chakraborty and S. Calabrese Barton, "Influence of Mediator Redox Potential on Fuel Sensitivity of Mediated Laccase Oxygen Reduction Electrodes" *Journal of The Electrochemical Society*, **158**(4), B440 (2011).

165. A.J. Bard and L.R. Faulkner, "*Electrochemical methods: fundamentals and applications*" 833 (Wiley: 2001).

166. N. Vogel, C.P. Hauser, K. Schuller, K. Landfester and C.K. Weiss, "Accurate Elemental Analysis of Metal-Containing Polymer Latexes Using ICP-Optical Emission Spectrometry" *Macromolecular Chemistry and Physics*, **211**(12), 1355-1368 (2010).

167. C. Bunte, O. Prucker, T. König and J. Rühe, "Enzyme containing redox polymer networks for biosensors or biofuel cells: a photochemical approach." *Langmuir : the ACS journal of surfaces and colloids*, **26**(8), 6019-27 (2010).

168. T. Tamaki, T. Ito and T. Yamaguchi, "Modelling of Reaction and Diffusion Processes in a High-surface-area Biofuel Cell Electrode Made of Redox Polymer-grafted Carbon" *Fuel Cells*, **9**(1), 37-43 (2009).

169. J.S. Newman and K.E. Thomas-Alyea, "*Electrochemical systems*" 647 (Wiley-IEEE: 2004).at <http://books.google.com/books?id=vArZu0HM-xYC&pgis=1>

170. C. Deslouis, "Transient Mass Transfer at a Coated Rotating Disk Electrode" *Journal of The Electrochemical Society*, **134**(10), 2496 (1987).

171. J.T. Stuart, "On the effects of uniform suction on the steady flow due to a rotating disk" *The Quarterly Journal of Mechanics and Applied Mathematics*, **7**(4), 446-457 (1954).

172. B. Nam and R.T. Bonnecaze, "Analytic Models of the Infinite Porous Rotating Disk Electrode" *Journal of The Electrochemical Society*, **154**(10), F191 (2007).

173. F. Lima, "Oxygen electrocatalysis on ultra-thin porous coating rotating ring/disk platinum and platinum-cobalt electrodes in alkaline media" *Electrochimica Acta*, **49**(24), 4091-4099 (2004).

174. N. Oyama and F.C. Anson, "Catalysis of electrode processes by multiply-charged metal complexes electrostatically bound to polyelectrolyte coatings on graphite electrodes, and the use of polymer-coated rotating disk electrodes in diagnosing kinetic and conduction mechanisms" *Analytical Chemistry*, **52**(8), 1192-1198 (1980).

175. R.B. Bird, W.E. Stewart and E.N. Lightfoot, "*Transport phenomena*" 905 (John Wiley and Sons: 2007).

176. D. Bom et al., "Thermogravimetric Analysis of the Oxidation of Multiwalled Carbon Nanotubes: Evidence for the Role of Defect Sites in Carbon Nanotube Chemistry" *Nano Letters*, **2**(6), 615-619 (2002).

Chapter 2 Carbon Fiber Microelectrodes Modified with Carbon Nanotubes as a New Support for Immobilization of Glucose Oxidase

2.1 Abstract

Carboxylated carbon nanotubes were coated onto carbon microfiber electrodes to create a micron-scale bioelectrode. This material has a high surface area and can serve as a support for immobilization of enzymes such as glucose oxidase. A typical carbon nanotube loading of 13 μg cm^{-1} yields a coating thickness of 17 μm and a 2000-fold increase in surface capacitance. The modified electrode was further coated with a biocatalytic hydrogel composed of a conductive redox polymer, glucose oxidase, and a crosslinker to create a glucose bioelectrode. The current density on oxidation of glucose is 16.6 mA cm^{-2} at 0.5 V (vs. Ag/AgCl) in oxygen-free glucose solution. We consider this approach to be useful for designing and characterizing surface treatments for carbon mats and papers by mimicking their local microenvironment.

2.2 Introduction

Biofuel cells generate power from ambient fuels such as plant saps, blood-borne glucose and process byproducts such as glycerol, and are suitable for mobile and distributed power applications.[1] Due to the selectivity of enzymes toward specific reactants and reactions, a conventional fuel cell's membrane and compartments can be eliminated, leading to opportunities for miniaturization.[2,3] However, achievable current density in biofuel cells is limited by low active-site density and inefficient electron transfer. Current densities of no more than about one mA cm^{-2} have been reported for complete biofuel cells in the literature.[4] This limited achievable current density remains a challenge for the practical application of biofuel cells.[5]

High surface area electrodes can increase current density by increasing electrochemically active interfaces within fixed electrode volume. Mesoporous materials are ideal as such host media.[6] Pore sizes of 2 to 50 nm are suitable for bio-molecule transport, and large surface area enables increased enzyme utilization. Enzymes have been immobilized in nanoporous silicates,[7–13] and polymers such as Nafion® and chitosan.[12,14,15] These nonconducting materials may be interspersed with carbon aerogels,[11] and nanotube matrices.[15] To incorporate enzymes within CNT matrices, direct drop-casting,[16] layer-by-layer self-assembly [17] and surface modification of CNTs [18] have been implemented to achieve well-mixed composites.

Multi-scale electrodes, with interconnected macropores that ensure liquid phase fuel transport and micropores that provide large surface area and enhanced catalyst loading, represent the desired electrode morphology. For example carbon paper consists of interlaced 10 micron diameter carbon fibers, with 80% porosity and surface area of 0.17 m^2 cm^{-3}, and has been used to immobilize biocatalysts for oxygen reduction [19] and glucose oxidation reactions.[20] To further increase the surface area and provide nanoporous sub-structure, CNTs have been grown on the carbon paper with chemical vapor deposition, leading to a 100-fold increase in surface area and a 10-fold increase in current density.[20] Ivnitski *et al.* [21] coated glucose oxidase, polyethyleneimine and Nafion on this structure to achieve enhanced direct electron transfer. However, quantitative analysis of such electrodes is complicated by non-homogeneous distribution of surface area and material concentrations in the multi-scale structure; it is therefore desirable to study the micro- and nano-scale process separately.

Carbon fiber microelectrodes (CFME) have also been implemented as electrodes in miniature biofuel cells.[2,4,22] and provide a platform that mimics the micro-environment of a single fiber of carbon paper. In this capacity, CFMEs have been used to study lithium intercalation in lithium batteries.[23,24] Various morphologies of biocatalyzed CFMEs have been reported. Pishko *et al.* used a beveled fiber electrode cross-section to make a glucose sensor.[25] Chen *et al.* fixed fibers into polycarbonate grooves and cast on the fiber mediator-enzyme adducts that achieved both glucose oxidation and oxygen reduction.[22] F. Gao *et al*. used the same setup and test condition, but with nanoporous carbon fibers to enhance surface area.[26] Chen *et al.* used a carbon nanoelectrode modified with CNTs for bio-molecule detection, without any enzyme or mediator coating.[27]

In the current work, CFMEs that mimic the morphology and microenvironment of nanotube-coated carbon paper fibers were fabricated and characterized. The CFME has diameter of 7 μm with exposed length of 1 cm. CNT and biocatalyst were coated on the exposed fiber at varied loading to form miniature bio-electrodes. Electrode morphology was characterized scanning electron microscopy (SEM), optical microscopy, and electrochemical capacitance. Bioelectrocatalytic performance was assessed using glucose oxidation catalyzed by mediated glucose oxidase. Understanding of this simple system informs the design and further study of high surface area, multiscale electrodes

2.3 Experimental

2.3.1 Chemicals and materials

Carboxylated multiwall carbon nanotubes (unless mentioned otherwise, CNT hereafter refers to carboxylated CNT) were obtained from Nanocyl (Sambreville, Belgium, http://www.nanocyl.com/). Carbon microfibers of 7 μm diameter were obtained from Goodfellow (Huntingdon, UK, http://www.goodfellow.com/). Conductive carbon paint was purchased from SPI Supplies (West Chester, PA, http://www.2spi.com). Glass capillary was obtained from A-M Systems (Carlsborg, WA, http://www.a-msystems.com/). N,N-dimethylformamide (DMF) was purchased from Fisher BioReagents (Hampton, NH, http://www.fishersci.com). Glucose oxidase (GOx) from *Aspergillus niger* was purchased from Sigma Aldrich (St. Louis, MO, http://www.sigmaaldrich.com). The synthesis of redox polymer Poly(vinylimidazole)-$[Os(bipyridine)_2Cl]^{+/2+}$ was reported previously. D-glucose, sodium bicarbonate, sodium phosphate monobasic, sodium phosphate diabasic were purchased from J.T. Baker (Phillipsburg, NJ, http://www.jtbaker.com) and used as received.

2.3.2 CFME fabrication

The schematic of CFME is demonstrated in Figure 2.1. Carbon fiber was attached to copper wire with conductive carbon paint, and flame fuse-sealed in the tip of a micropipette by a micropipette puller (Sutter Instrument, Model P-30, Novato, CA, http://www.sutter.com). The exposed fiber was cut to 1 cm with a scalpel.

CNTs were dispersed in DMF to form 1 mg mL^{-1} solution.[28] The DMF/CNT solution was cast to a CFME by brushing a micropipette tip on the electrode fiber. The freshly coated CFME was rinsed with DI water and dried at 70 ºC for one hour before use.

2.3.3 Surface morphology and surface area characterization

The morphology of the CFME was characterized by both scanning electron microscope (SEM, JEOL JSM-7500F, 5.0 kV accelerating voltage and 2 mm working distance) and optical microscope (Nikon Eclipse LV150, Tokyo, Japan, http://www.nikoninstruments.com). Electrochemical capacitance was measured by cyclic voltammetry at varying scanning rates from 0.4 to 0.5 V vs. Ag/AgCl. Non-faradaic current was plotted against scanning rate, the slope of which was recorded as the capacitance. Surface area was estimated from capacitance using an assumed specific capacitance of 25 μF cm^{-2}, a value that is representative of carbon materials.[29]

2.4 Biocatalyst coating

Biocatalyst precursor solution was cast onto CFME to form a hydrogel. The preparation of precursor solution was previously reported.[20,30] A solution of 40 mg mL^{-1} GOx was made with 0.1 M $NaHCO_3$, mixed with 7 mg mL^{-1} sodium periodate at 1:2 volume ratio and cured for one hour in darkness.[31,32] Finally, 2 μL periodate-oxidized GOx, 8 μL 10 mg mL^{-1} PVI-$[Os(bipyridine)_2Cl]^{+/2+}$ redox polymer and 0.5 μL 2.5 mg mL^{-1} PEGDGE were mixed together to yield the precursor solution. Similar to CNT immobilization, a micropipette was used to brush the precursor solution onto CFME, followed by 12-hour curing before further experiments.

2.5 Electrochemical characterization

Electrochemical characterization was conducted in a water-jacketed cell containing 50 mL phosphate-buffered saline (PBS, 20 mM phosphate, 0.1 M NaCl, pH 7.0) at 37.5 ºC, using a Bio-Logic (Knoxville, TN, http://www.bio-logic.info) VSP potentiostat. Working electrode potential was measured relative to a silver-silver chloride (Ag|AgCl) reference electrode (Fisher Scientific, Hampton, NH), with platinum wire counter electrode. Redox polymer response was characterized by cyclic voltammetry with scan rate at 50 mV/s from 0.0 V to 0.5 V/Ag|AgCl with glucose-free electrolyte and nitrogen sparging to exclude oxygen. Electrode polarization was carried out in the same potential range, but at scan rate of 1 mV s^{-1}, with 50 mM glucose and nitrogen sparging.

2.6 Results and discussion

2.6.1 CNT coated CFME

CNT coatings of up to 13 μg cm^{-2} were applied to the carbon fiber surface. Figure 2.2 shows the scanning electron micrograph of the CFMEs coated with CNTs, indicating significant roughness on the micron scale. On the nano-scale, the nanotubes interlaced into a homogeneous porous material. Pore size was estimated from Figure 2.2a to be 50 nm on average, suitable for passage of ~10 nm biomolecules. Electrodes with varying CNT loading had the same nano-porous surface but differed in micron-scale roughness and coating thickness, as shown in Figure 2d-h.

The capacitance and coating thickness of CNT-loaded CFMEs are shown in Figure 2.3. As expected, the thickness followed a square root relationship with coating mass. The large standard deviation is due to micron-scale roughness. Capacitance increased 2,000 fold above a bare CFME. Capacitance increases linearly at small CNT loading up to 6 µg, above which the slope decreases, probably due to transport limitations that hinder charge transport to inner NT layers.

2.6.2 Bare CFME coated with hydrogel

As a baseline, bare CFMEs without CNTs were coated with biocatalyst. The coating thickness with varying precursor solution volume is shown in Figure 2.4. As expected, the coating thickness is proportional to the square root of applied precursor solution volume. Compared to CNT-coated CFME surfaces in Figure 2.2, the hydrogel coating layer surface is smoother and less varied in thickness (Figure 2.4 a-f).

The effect of hydrogel film thickness on the current density for glucose oxidation on bare CFMEs is shown in Figure 2.5. The inset shows a typical polarization curve for the bioanode. The current density reaches a maximum at 0.3 V/Ag|AgCl, and shows a hysteresis of ~0.2 mA cm^{-2} at 0.3 V. The current densities at 0.5 V for all the film thicknesses are summarized, from which it can be concluded that less than 5 µm of the hydrogel film thickness was active for glucose oxidation, with less than 10% variation in current density from 1 to 15 µm film thickness. At thickness greater than 10 μm, the glucose oxidation current decreased, probably due to transport limitations of glucose and mediator within the hydrogel film.

2.6.3 CFME/CNT/Hydrogel composite electrode

The hydrophilicity of the CNT coating layer directly impacts the loading of hydrogel into the layer, since the hydrogel is highly hydrophilic. For this reason, carboxylated CNT are employed in this work. As demonstrated in Figure 2.6, NT-coated CFMEs with hydrogel loading of up to 40 μg cm^{-1} maintain constant layer thickness, suggesting that the hydrogel material has been completely absorbed into the NT layer. Based on the NT loading of 13 μg cm^{-1}, the NT layer can absorb up to 3.1 g of hydrogel per g NTs. Addition of the hydrogel component leads to a more uniform thickness as indicated by the smaller error bars as compared to Figure 2.3. Hydrogel coating thickness on bare fibers is also shown and is consistent with the complete absorption of the hydrogel into the NT layer.

Electrochemical characterizations of CNT/hydrogel-coated CFMEs are shown in Figure 2.7. The top figure shows cyclic voltammograms of three typical samples in the absence of glucose. The observed redox couple is associated with the mediator redox reaction at the electrode. Samples a to c correspond to increasing CNT loadings. For a totally reversible single electron redox reaction, the peak separation should be 56.5 mV at 25°C.[33] In our system, the peak separation increased from 90 mV for sample a, to 290 mV for sample c. This is an indication of large internal resistance (see Electronic Supplementary Material). The peak height increased from 0.87 to 5.76 mA cm^{-2} due to the increased loading of the redox mediator complex. The mediator activity trend affected the polarization curve (Figure 2.7 b) in two ways:

the current density increased 6.4 fold from 2.58 to 16.63 mA cm^{-2} at 0.5 V, and the mass-transport-controlled plateau current region shifted to the right and was not reached at high mediator loading.

Current density of a larger set of samples at 0.5 V/Ag|AgCl is summarized in Figure 2.7-c, where it is shown to correlate linearly with estimated surface area (Figure 2.3). Such a linear relationship indicates that the CNT surface area is utilized uniformly by the bioactive materials, even at very high loading (13 µg cm^{-1}) and CNT layer thickness (~17 µm). Diffusional transport of glucose, enhanced by the cylindrical geometry of the electrode, is not substantially hindered by the presence of the nanotubes. Current density is found to vary with glucose concentration according to the expected Michaelis-Menten relationship, with maximum current density and apparent Michaelis constants reported in Electronic Supplementary Material.

To explain the increasing peak separation in Figure 2.7, the peak separation as a function of peak current density is plotted in Figure 2.8. A linear relationship is observed, with internal resistance estimated to be 39.3 $\Omega\cdot\text{cm}^2$. This resistance arises due to limited contact between the copper wire and carbon fiber; we have since demonstrated that this resistance can be eliminated by increased contact length, which will be discussed in a future work.

The effect of glucose concentration on the current density at 0.5 V/Ag|AgCl was studied and the result is shown in Figure 2.9. The observed trend follows Michaelis-Menten kinetics. The maximum current, $I_{\max}$, and apparent Michaelis constant, K'_m, were estimated by nonlinear fitting and are shown in Table 2.1**.** Literature values of K'_m for immobilized glucose oxidase range from 4 mM to 87 mM, depending on the immobilization technique.[34] The values obtained here, which lie at the lower end of this range, are impacted by limited electron transport via the hydrogel mediator. The true Michaelis constant, K_m, is currently being estimated via a reaction-diffusion model. Zakeeruddin *et al.* obtained similar results for mediated glucose oxidation.[35] A rough estimation of turnover number was obtained from I_{max} and the nominal enzyme loading. Comparing to periodate-oxidized GOx at 323 s^{-1} [36] and immobilized GOx at 250 s^{-1},[37] the low values reported here are probably due to the fact that not all the GOx was electrochemically active.

2.7 Conclusions

A high surface area CNT coated CFME electrode for mediated biocatalysis is shown to provide quantifiable and observable increases in electrode current density. Compared to the bare CFME, the surface area of the modified electrode showed more than 2000-fold increase. Thanks to the hydrophilicity of the carboxylated CNT, the biocatalyst precursor solution was absorbed into the porous structure and formed a well-mixed CNT/hydrogel composite. This composite increased the concentration of active mediator and enzyme, and led to a 6.4 fold increase in glucose oxidation current density to 16.63 mA cm^{-2} at 0.5 V/Ag|AgCl. This work lays a foundation for understanding reaction and transport mechanisms in fiber supported bioelectrodes and micro-bioelectrodes for sensors and miniature biofuel cells.

2.8 Acknowledgments

The authors gratefully acknowledge support from the University of New Mexico under contract FA9550-06-1- 0264 from the Air Force Office of Scientific Research.

2.9 Tables

Table 2.1 Fitted parameter values from concentration study, assuming Michaelis-Menten kinetics

Series	K_{m}, mM	I_{max}, mA cm^{-2}	Turnover number, s^{-1}
Bare	10.30	3.06	0.5
4 μg cm^{-1} CNT	8.86	12.73	2.3
10 μg cm^{-1} CNT	7.53	17.24	3.1

2.10 Figures

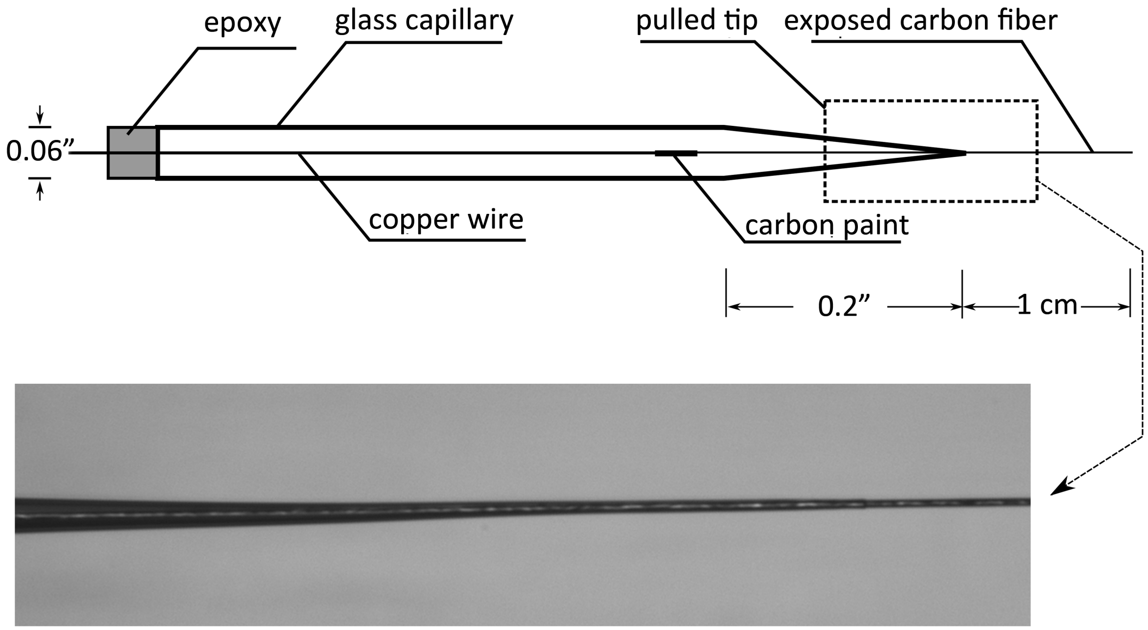

Figure 2.1 Carbon fiber microelectrode design. **a.** Electrode diagram with dimensions. **b.** optical micrograph showing carbon fiber-capillary interface.

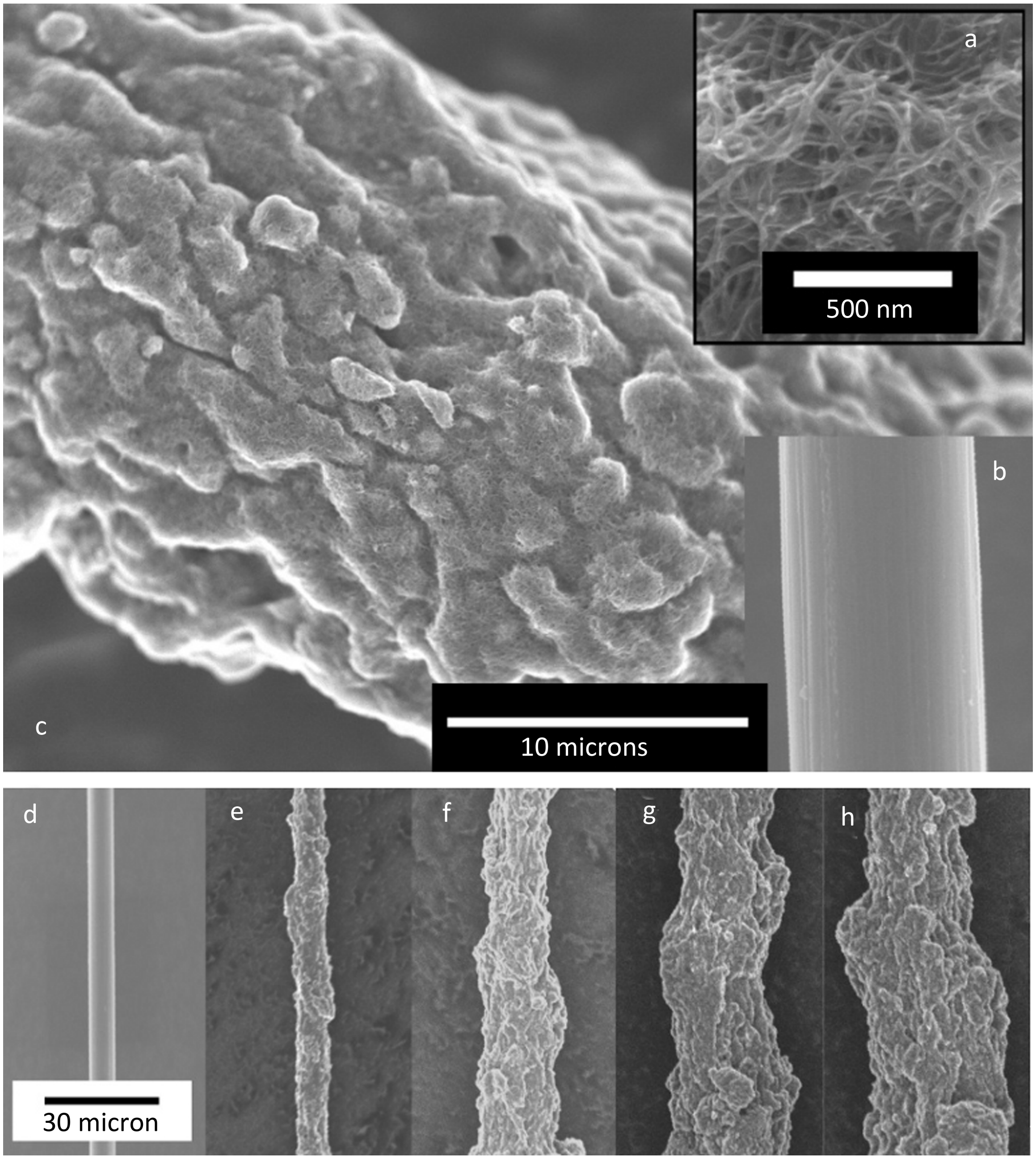

Figure 2.2 Scanning electron micrographs of CNT coated CFME. **a.** and **c.** fiber with 2 μg cm^{-1} loading; **b.** Bare carbon fiber control with same scale as (c.); **d-h.** CFME/CNT morphology with increasing CNT loading: **d.** bare CFME, **e.** 1 μg cm^{-1}, **f.** 2 μg cm^{-1}, **g.**, 5 μg cm^{-1}, **h.** 13 μg cm^{-1}.

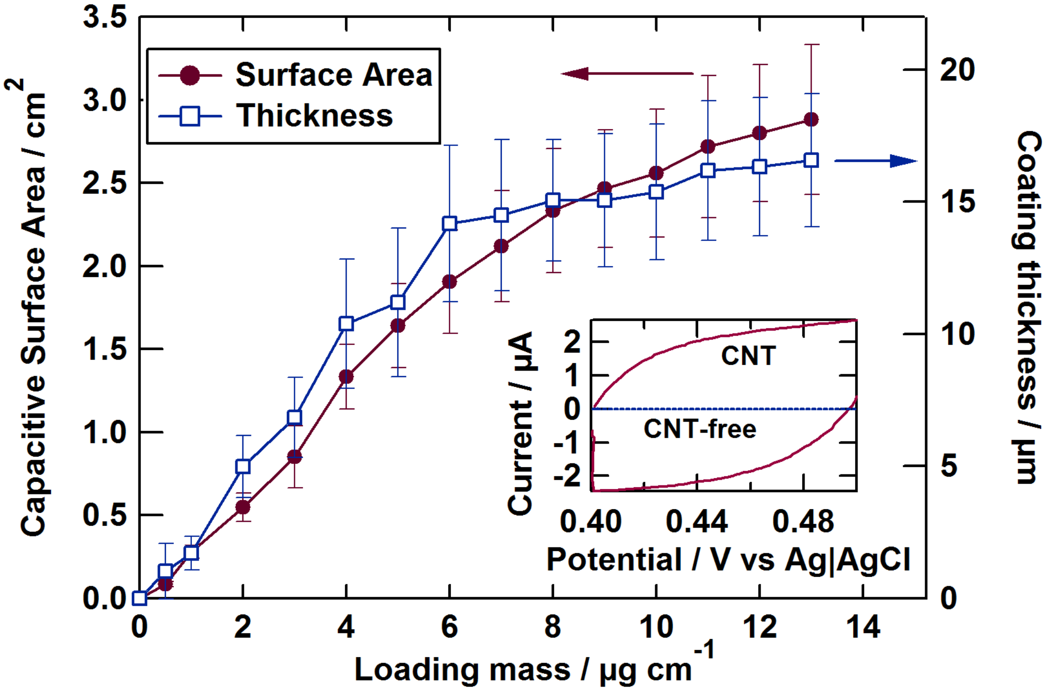

Figure 2.3 Surface characterization of CNT-coated CFME. Capacitance obtained by cyclic voltammetry in the 0.4 to 0.5 V/Ag|AgCl range in phosphate buffer solution, pH 7.0, 25 °C. Inset: cyclic voltammetry at 30 mV/s for bare CFME and 13 µg cm^{-1} CNT loaded CFME. Surface area was calculated from capacitance assuming a specific capacitance of 25 µF cm^{-2}.

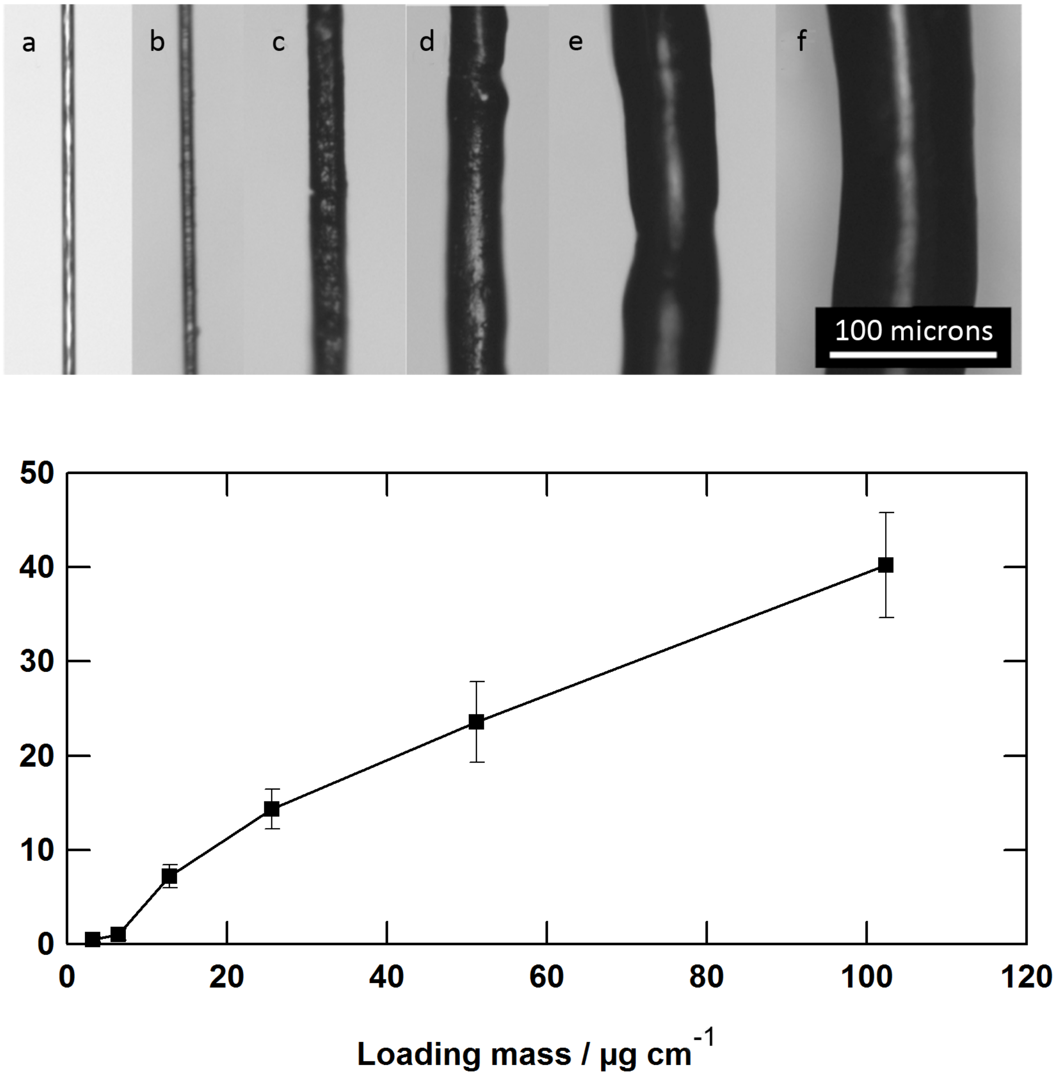

Figure 2.4 Biocatalyst-containing hydrogel films cast on a NT-free CFME. Top: optical micrographs for precursor solution volume of **a.** 0, **b.** 3.2 µg cm^{-1}, **c.** 12.8 µg cm^{-1}, **d.** 25.6 µg cm^{-1}, **e.** 51.2 µg cm^{-1}, **f.** 102.4 µg cm^{-1}. Bottom: summary of the loading and thickness

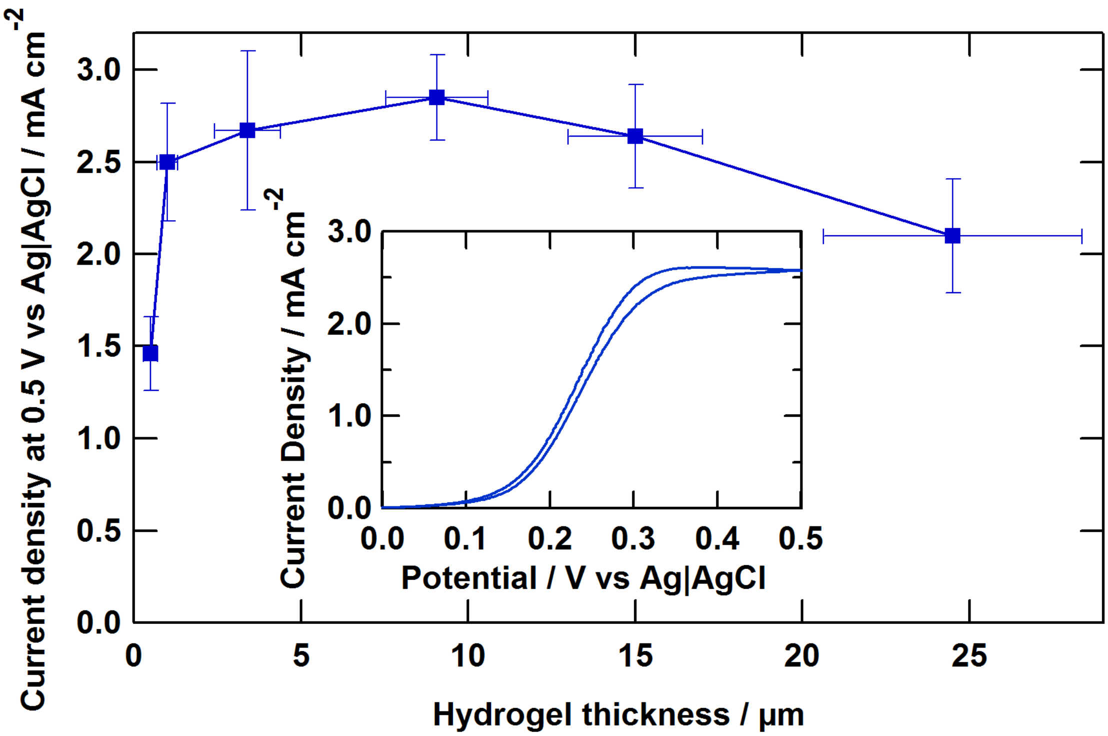

Figure 2.5 Effect of hydrogel coating thickness on glucose oxidation rate at NT-free CFME at 0.5 V/Ag|AgCl. Inset: example polarization curve at 15 µm coating thickness. Conditions: nitrogen-purged 50 mM glucose in PBS pH 7, 37.5 ºC, scan rate 1 mV s^{-1}, with stirring bar rotating at 150 rpm.

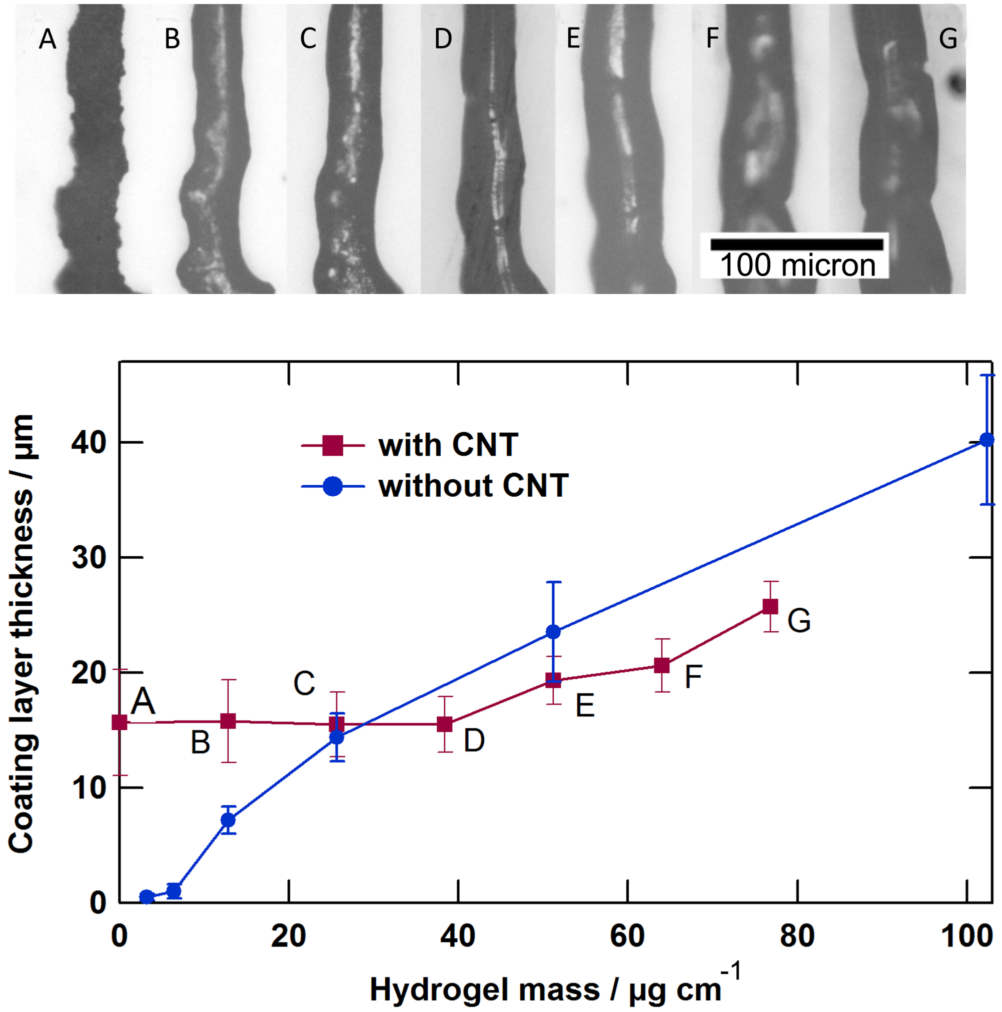

Figure 2.6 Hydrogel infiltration into CNT matrix. Hydrogel was coated on 13 µg cm^{-1} CNT-coated CFME at loadings from 0 (A) to 76.8 µg cm^{-1} (G). Optical micrographs show the change in dry hydrogel coating thickness at the same site. Beyond point D, The pores of the CNT layer were filled, thus the increase of dry thickness beyond point D can be compared to a CNT-free microelectrode.

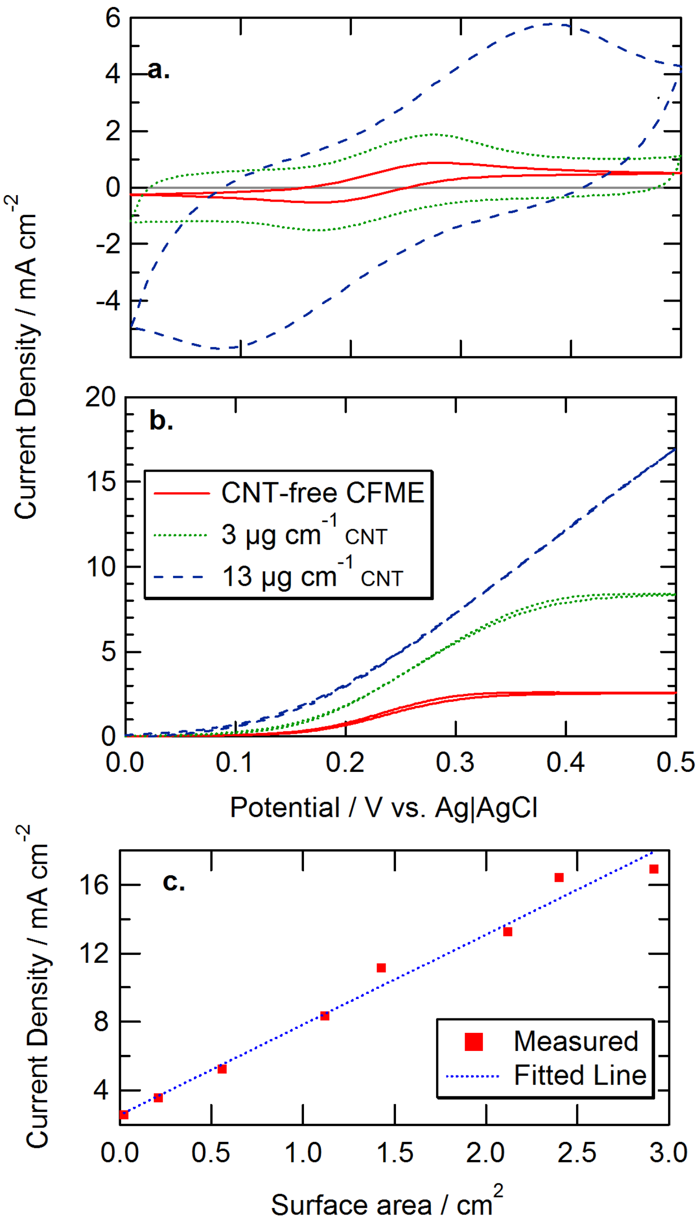

Figure 2.7 Electrochemical characterization of CFME/CNT/hydrogel electrodes for three CNT loadings. (a) Redox polymer voltammetry in N_2-purged PBS, pH 7.0, 37.5°C, glucose-free, at 50 mV/s. (b) Glucose oxidation in the same electrolyte, but with 50 mM glucose at 1 mV/s. Convection was introduced by rotating a magnetic stirring bar at 150 rpm. The samples were all loaded with 26 µg cm^{-1} hydrogel with 39.6 wt% GOx, 59.5 wt% redox polymer and 0.9 wt% PEGDGE. (c) Summary plot of glucose oxidation current density with linear fit.

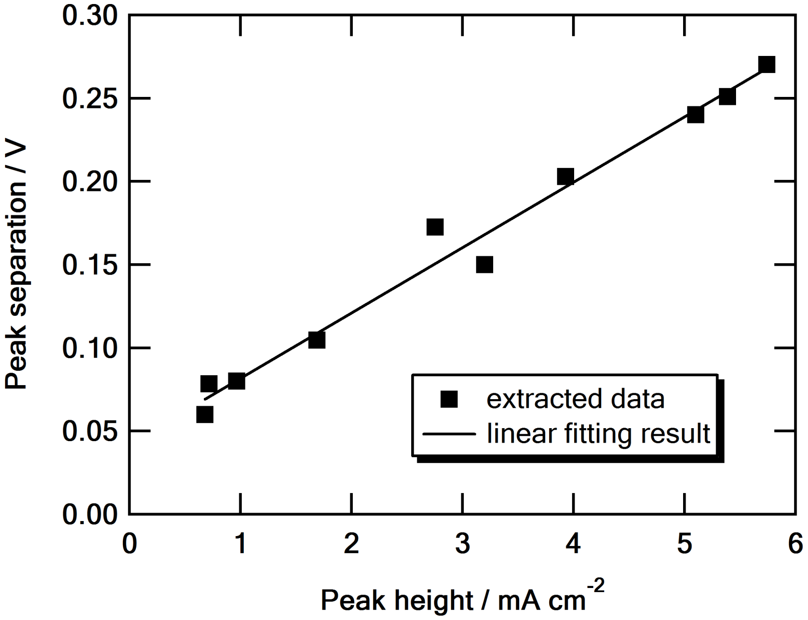

Figure 2.8 Cyclic voltammetric peak separation as a function of peak height. Tests were conducted in N_2-purged phosphate buffer solution, pH 7.0, 37.5°C, glucose-free, at 50 mV/s. The linear fitting resulted in a slope of 39.3 $\Omega \cdot cm^2$.

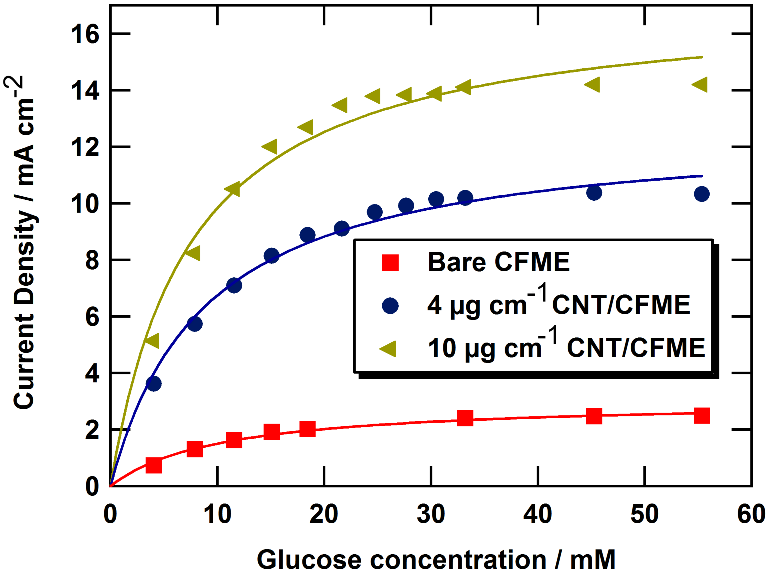

Figure 2.9 Current density at 0.5 V vs. varying glucose concentrations for three different loadings of CNT. The experimental data is shown fitted with a Michaelis-Menten kinetics model, with the fitted parameter values given in Table 1.

REFERENCES

References

1. S. Calabrese Barton, J. Gallaway and P. Atanassov, "Enzymatic Biofuel Cells for Implantable and Microscale Devices" *Chemical Reviews*, **104**(10), 4867-4886 (2004).

2. N. Mano, F. Mao and A. Heller, "A Miniature Biofuel Cell Operating in A Physiological Buffer" *Journal of the American Chemical Society*, **124**(44), 12962-12963 (2002).

3. A. Heller, "Miniature biofuel cells" *Physical Chemistry Chemical Physics*, **6**(2), 209 (2004).

4. N. Mano, F. Mao and A. Heller, "Characteristics of a miniature compartment-less glucose-O2 biofuel cell and its operation in a living plant." *Journal of the American Chemical Society*, **125**(21), 6588-94 (2003).

5. T. Tamaki et al., "Evaluation of Immobilized Enzyme in a High-Surface-Area Biofuel Cell Electrode Made of Redox-Polymer-Grafted Carbon Black" *Industrial & Engineering Chemistry Research*, **49**(14), 6394-6398 (2010).

6. J. Kim, H. Jia and P. Wang, "Challenges in biocatalysis for enzyme-based biofuel cells." *Biotechnology advances*, **24**(3), 296-308 (2006).

7. N. Mano, H.-H. Kim and A. Heller, "On the Relationship between the Characteristics of Bilirubin Oxidases and O_2 Cathodes Based on Their “Wiring”" *The Journal of Physical Chemistry B*, **106**(34), 8842-8848 (2002).

8. J. Díaz, "Enzyme immobilization in MCM-41 molecular sieve" *Journal of Molecular Catalysis B: Enzymatic*, **2**(2-3), 115-126 (1996).

9. P. Wang, S. Dai, S.D. Waezsada, a Y. Tsao and B.H. Davison, "Enzyme stabilization by covalent binding in nanoporous sol-gel glass for nonaqueous biocatalysis." *Biotechnology and bioengineering*, **74**(3), 249-55 (2001).

10. C. Lei, Y. Shin, J. Liu and E.J. Ackerman, "Entrapping enzyme in a functionalized nanoporous support." *Journal of the American Chemical Society*, **124**(38), 11242-3 (2002).

11. M. Tsionsky, G. Gun, V. Glezer and O. Lev, "Sol-Gel-Derived Ceramic-Carbon Composite Electrodes: Introduction and Scope of Applications" *Analytical Chemistry*, **66**(10), 1747-1753 (1994).

12. J.-D. Qiu, H.-Y. Xie and R.-P. Liang, "Preparation of porous chitosan/carbon nanotubes film modified electrode for biosensor application" *Microchimica Acta*, **162**(1-2), 57-64 (2007).

13. D. Ivnitski et al., "Entrapment of enzymes and carbon nanotubes in biologically synthesized silica: glucose oxidase-catalyzed direct electron transfer." *Small (Weinheim an der Bergstrasse, Germany)*, **4**(3), 357-64 (2008).

14. Y. Liu, M. Wang, F. Zhao, Z. Xu and S. Dong, "The direct electron transfer of glucose oxidase and glucose biosensor based on carbon nanotubes/chitosan matrix." *Biosensors & bioelectronics*, **21**(6), 984-8 (2005).

15. T. Klotzbach, M. Watt, Y. Ansari and S. Minteer, "Effects of hydrophobic modification of chitosan and Nafion on transport properties, ion-exchange capacities, and enzyme immobilization" *Journal of Membrane Science*, **282**(1-2), 276-283 (2006).

16. J. Wang, M. Li, Z. Shi, N. Li and Z. Gu, "Direct electrochemistry of cytochrome c at a glassy carbon electrode modified with single-wall carbon nanotubes." *Analytical chemistry*, **74**(9), 1993-7 (2002).

17. L. Deng et al., "Multilayer structured carbon nanotubes/poly-l-lysine/laccase composite cathode for glucose/O2 biofuel cell" *Electrochemistry Communications*, **10**(7), 1012-1015 (2008).

18. F. Gao, L. Viry, M. Maugey, P. Poulin and N. Mano, "Engineering hybrid nanotube wires for high-power biofuel cells" *Nature Communications*, **1**(1), 1-7 (2010).

19. S. Calabrese Barton, H.-H. Kim, G. Binyamin, Y. Zhang and A. Heller, "Electroreduction of O2 to Water on the “Wired” Laccase Cathode" *The Journal of Physical Chemistry B*, **105**(47), 11917-11921 (2001).

20. S. Calabrese Barton, Y. Sun, B. Chandra, S. White and J. Hone, "Mediated Enzyme Electrodes with Combined Micro- and Nanoscale Supports" *Electrochemical and Solid-State Letters*, **10**(5), B96 (2007).

21. D. Ivnitski, B. Branch, P. Atanassov and C. Apblett, "Glucose oxidase anode for biofuel cell based on direct electron transfer" *Electrochemistry Communications*, **8**(8), 1204-1210 (2006).

22. T. Chen et al., "A Miniature Biofuel Cell" *Journal of the American Chemical Society*, **123**(35), 8630-8631 (2001).

23. M.W. Verbrugge, "Modeling Lithium Intercalation of Single-Fiber Carbon Microelectrodes" *Journal of The Electrochemical Society*, **143**(2), 600 (1996).

24. M.W. Verbrugge, "Lithium Intercalation of Carbon-Fiber Microelectrodes" *Journal of The Electrochemical Society*, **143**(1), 24 (1996).

25. M.V. Pishko, A.C. Michael and A. Heller, "Amperometric glucose microelectrodes prepared through immobilization of glucose oxidase in redox hydrogels" *Analytical Chemistry*, **63**(20), 2268-2272 (1991).

26. X. Zhao, X. Lu, W.T.Y. Tze and P. Wang, "A single carbon fiber microelectrode with branching carbon nanotubes for bioelectrochemical processes." *Biosensors & Bioelectronics*, **25**(10), 2343-50 (2010).

27. R.-sheng Chen, W.-hua Huang, H. Tong, Z.-li Wang and J.-ke Cheng, "Carbon fiber nanoelectrodes modified by single-walled carbon nanotubes." *Analytical Chemistry*, **75**(22), 6341-5 (2003).

28. K.. Arepalli, S.; Freiman, S. W.; Hooker, S.; Migler, "*Measurement Issues in Single-Wall Carbon Nanotubes*" 72 (2008).

29. K. Kinoshita, "*Carbon: electrochemical and physicochemical properties*" 533 (Wiley: Hoboken, 1988).

30. S. Calabrese Barton, "Mixed-reactant, strip-cell direct methanol fuel cells" *Journal of Power Sources*, **96**(2), 329-336 (2001).

31. O. Zaborsky, "The immobilization of glucose oxidase via activation of its carbohydrate residues" *Biochemical and Biophysical Research Communications*, **61**(1), 210-216 (1974).

32. G. Binyamin, "Stabilization of Wired Glucose Oxidase Anodes Rotating at 1000 rpm at 37°C" *Journal of The Electrochemical Society*, **146**(8), 2965 (1999).

33. A.J. Bard and L.R. Faulkner, "*Electrochemical methods: fundamentals and applications*" 833 (Wiley: 2001).

34. B. Szajáni, a Molnár, G. Klámar and M. Kálmán, "Preparation, characterization, and potential application of an immobilized glucose oxidase." *Applied biochemistry and biotechnology*, **14**(1), 37-47 (1987).

35. S.M. Zakeeruddin, "complexes of iron (II), ruthenium (H) and osmium (I1) as mediators for glucose oxidase of Aspergillus niger and other redox proteins" *Solutions*, **337**253-283 (1992).

36. S. Nakamura, S. Hayashi and K. Koga, "Effect of periodate oxidation on the structure and properties of glucose oxidase." *Biochimica et biophysica acta*, **445**(2), 294-308 (1976).

37. S.A. Yamanaka et al., "Enzymatic activity of glucose oxidase encapsulated in transparent glass by the sol-gel method" Chemistry of Materials, 4(3), 495-497 (1992).

Chapter 3 Carbon Nanotube Modified Biocatalytic Microelectrodes with Multiscale Porosity

3.1 Abstract

Macropores were introduced into nanotube matrices via polystyrene bead templates, and the resulting matrix was applied to carbon fiber microelectrodes as a porous medium for immobilization of enzymatic biocatalysts. The macropores were found to increase the electrochemically active surface area by two fold at a nominal polystyrene mass fraction of 73%. The modified electrodes were further coated with biocatalyst hydrogel comprising glucose oxidase, redox polymer and crosslinker to create a glucose oxidizing bioanode. Glucose oxidation current density also increased two-fold after introduction of the macropores. Focused ion beam cut cross sections reveal complete adsorption of the enzyme-hydrogel matrix into the CNT layer. This templating technique is a promising approach to maximization of surface area and transport in bioelectrodes.

3.2 Introduction

Biofuel cells are electrochemical devices that convert biofuel substrates or biomass into electricity.[1] They are suitable for mobile and distributed power applications due to their capability to carry out reactions near room temperature, neutral pH, and their selectivity towards reactants.[2] Among other techniques, immobilization of enzymes in redox hydrogels has been proved to enhance enzyme activity due to the mediator conducting effect between current collector and enzyme active centers.[3,4] However, low active site density and inefficient electron transfer have limited the achievable current density to ~1 mA cm^{-2} for biofuel cells.[5,6]

High surface area materials have been extensively employed to improve electrode efficiency.[7,8] Carbon papers have been used as porous supports for bioelectrodes.[9–12] Carbon fiber microelectrodes (CFMEs) have been applied as a component for miniature biofuel cells,[13,14] and as a platform to study lithium ion intercalation in lithium ion batteries.[15,16] Various morphologies, including beveled fiber surfaces,[17] single fibers isolated in carbonate grooves,[13] nanoporous fibers,[18] fibers with branching carbon nanotubes (CNTs),[19,20] and exposed carbon fiber coated with porous CNTs [21] have been studied. In the latter study, suffusion of a porous CNT layer with a hydrogel containing redox mediator and glucose oxidase yielded a glucose oxidizing microelectrode with increased current density. It was shown that glucose oxidation current density was directly proportional to CNT surface area, suggesting that mass transport of glucose into the CNT layer was not rate limiting. However, it was not clear that

CNT surface area was maximally utilized by the biocatalyst, because the typical 50 nm pore size of the CNT layer could inhibit absorption of the biocatalyst-hydrogel precursor solution.

One approach to address this limitation is to introduce macropores into the CNT layer. Pore former techniques, in which template materials are removed either by dissolution or heat-treatment to introduce arrays of macropores, are promising candidates to enhance transport in dense porous media.[22] Template materials can be formed by filtering colloidal particle dispersions,[23–27] oil emulsion droplets,[28,29] or self-assembly.[23,30,31] Such porous carbons have been widely applied for fuel cell catalyst supports.[32] For example, polystyrene spheres combined with silica particles served as a template for a bimodal ordered porous catalyst support for direct methanol fuel cells.[33] Mano *et al.* have used macroporous carbon foam formed on a silica template as a support for glucose oxidase bioelectrode.[28]

3.3 Experimental

3.3.1 *Materials and chemicals*

Carbon fibers of 7.0 ± 0.3 μm diameter were obtained from Goodfellow (Huntingdon, UK). Carboxylated multiwall carbon nanotubes were purchased from Nanocyl (NC3101, Sambreville, Belgium). Conductive carbon paint was purchased from SPI Supplies (West Chester, PA). Glass capillary was purchased from A-M Systems (Carlsborg, WA) and used as fiber electrode body material. *N,N*-dimethylformamide (DMF) was obtained from Fisher BioReagents (Hampton, NH). Monodispersed polystyrene micro particle suspension (Part number: 95585) and glucose oxidase (GOx) from *Aspergillus niger* was purchased from Sigma

Aldrich (St. Louis, MO). The synthesis of redox polymer Poly(vinylimidazole)-$[Os(bipyridine)_2Cl]^{+/2+}$ can be found elsewhere.[3] Poly(ethylene glycol) (400) diglycidyl ether (PEGDGE) was obtained from Polysciences (Warrington, PA). Sodium periodate was purchased from MP Biomedicals (Solon, OH). Nitrogen gas was obtained from Airgas. D-glucose, sodium bicarbonate, sodium phosphate monobasic, sodium phosphate diabasic were purchased from J.T. Baker (Phillipsburg, NJ) and used as received.

3.3.2 Sealing of carbon fiber into glass capillary

A micropipette puller (Sutter Instrument, P-30, Novato, CA) was used to fuse-seal carbon fibers into pulled glass capillary tips. The carbon fibers were connected to copper wires through conductive carbon paint at the open end of the capillary. Single fibers were thus sealed tightly with glass and aligned well with the pointing tip, enabling easy handling and electrolyte insulation from copper wires. Exposed carbon fiber length was maintained at 1 cm.

3.3.3 Preparation of CNT/PS suspensions and immobilization on single carbon fibers

A 1 mg mL^{-1} suspension of carboxylated carbon nanotubes in DMF was ultra-sonicated for 1 hour for uniform dispersion. DMF is a polar, aprotic solvent that is miscible with water. This CNT/DMF dispersion was stable for at least a week.

The PS particles were received as a monodispersed aqueous suspension, which was added to CNT/DMF suspension to make a PS/CNT/DMF precursor suspension to be subsequently applied to the CFMEs. Particle size and number concentration, as given in product specifications, allowed calculation of final PS volume fractions in CNT matrix after solvent evaporation. The PS/CNT/DMF suspension was applied to the entire exposed carbon fiber length

(1 cm) by brushing with a micropipette tip. The freshly coated CFMEs were rinsed with DI water and dried at 70 ºC for one hour to fully remove DMF before usage.

PS/CNT coated CFMEs were heat treated under air for 4 hours at 450 ºC to remove PS particles, following a previous procedure.[30] Heat treatment for shorter times, *e.g.*, 2 hours yielded samples that exhibited high ohmic resistance with residual gel-like PS phases observable by SEM. CFMEs heat-treated for 4 hours exhibited neither of these phenomena. Multiwall CNTS have been shown to be stable up to 500 °C by TGA analysis.[34]

3.3.4 Surface morphology and thickness characterization

A scanning electron microscope (SEM, JEOL JSM-7500F, 5.0 kV accelerating voltage and 2 mm working distance) and an optical microscope (Nikon Eclipse LV150, Tokyo, Japan) were used to observe the surface morphology of CFMEs. Carbon fiber thicknesses were digitally measured by MATLAB®, averaging over a ~1.3 mm length of fiber.

Capacitive surface area was estimated by cyclic voltammetry in phosphate buffer solution (PBS, 20 mM phosphate, pH 7.0, with 0.1 M NaCl as supporting electrolyte), at 37.5 °C, with varying scanning rates from 0.4 to 0.5 V vs. Ag|AgCl. This potential range was chosen to minimize background current. Non-faradaic currents were plotted against scanning rates, the slope of which was recorded as the capacitance. Surface area was estimated from capacitance using an assumed specific capacitance of 25 $\mu F\ cm^{-2}$, which is representative of carbon materials.[35]

3.3.5 Cross-sectional morphology imaging

Cross sections of single carbon fibers were cut and revealed by Focused Ion Beam - SEM (FIB, Carl Zeiss NTS GmbH, Germany). Bulk cutting through fibers were accomplished with a focused ion beam of 20 nA at 30 kV. The revealed surface was subsequently polished using a small beam current of 1 nA at 30 kV. Final micrographs were collected with SEM detectors.

3.3.6 Biocatalyst coating

The preparation of biocatalyst precursor solution has been previously reported.[9] A solution of 40 mg mL^{-1} GOx was prepared with 0.1 M $NaHCO_3$, mixed with 7 mg mL^{-1} sodium periodate at 1:2 volume ratio and cured for one hour in darkness.[36,37] Final precursor solution was made by mixing 2 μL periodate-oxidized GOx, 8 μL 10 mg mL^{-1} PVI-$[Os(bipyridine)_2Cl]^{+/2+}$ redox polymer mediator and 0.5 μL of 2.5 mg mL^{-1} PEGDGE crosslinker. CFMEs modified with 2 μg cm^{-1} CNTs were coated with 1 μL cm^{-1} of precursor solution and cured for 12 hours in room temperature air before further tests. The above protocol leads to an electrode with 12 μg cm^{-1} solids loading with 59 wt% mediator, 40 wt% enzyme, and 1 wt% crosslinker.

3.3.7 Electrochemical characterization

Electrochemical characterization was conducted in a water-jacketed cell containing 50 mL PBS at 37.5 ºC and pH 7.0, made oxygen-free by nitrogen sparging. The reference electrode was Ag|AgCl (Fisher Scientific, Hampton, NH), with a platinum wire counter electrode.

Convection was introduced by rotating a magnetic stirring bar at 150 rpm. Redox polymer characterization was done with cyclic voltammetry using a VSP potentiostat (Bio-Logic, Knoxville, TN) at 50 mV/s scan rate from 0.0 V to 0.5 V/Ag|AgCl in glucose-free electrolyte. Electrode polarization in the presence of 50 mM glucose was conducted in the same conditions at 1 mV/s scan rate.

3.4 Results and discussion

The mass fraction of polystyrene particles in the PS/CNT layer is a key parameter that was controlled during this study. As shown in Figure 3.1, the PS/CNT composite can display five different composition scenarios - from pure CNT (Figure 3.1a) to pure PS (Figure 3.1e). The maximum volume fraction of PS is 74%, corresponding to a close-packed lattice of spheres. Case c, d, and e all have 74 vol% occupied by PS, but the *mass fraction* of CNTs decreases from c to e, and therefore the *mass fraction* of PS continues to increase. Hence, to avoid confusion, mass fraction (or wt%) is used to describe composition. For a high mass fraction of PS, there is insufficient CNT material to fill voids between PS spheres (Figure 3.1d**)**. Such case can lead to a CNT phase that is not inter-connected, and can collapse once the PS template is removed. For this reason, a majority of samples were made in the "dense packing" regime, in which the CNTs were sufficient to fill the gaps. Because the densities of the CNT and PS phases are about the same, dense packing occurs for PS content of 73 wt% or less.

3.4.1 CFMEs under electron microscopy

The morphologies of four representative samples were observed by SEM shown in Figure 3.2, and by FIB-revealed cross section in Figure 3.3. Figure 3.2a shows the control sample with 2 μg cm^{-1} loading of pure CNTs, displaying significant micron-scale roughness and a homogeneous nanoscale CNT matrix, consistent with literature results.[21] The cross-section view (Figure 3.3a inset) and side view (Figure 3.4a inset) reveal dense packing of CNTs, with average pore size of ~50 nm. This dense packing and small pore size could lead to transport limitations when the coating layer thickness is large.

A PS/CNT modified electrode at 73 wt% PS without heat treatment was observed. The surface view (Figure 3.2b) shows dense packing of particles on the surface. However, cross section (Figure 3.3b) indicates that PS particles congregated at the outer surface of the CNT layer and were not distributed uniformly in the radial direction. This may be due to the shrinkage of the CNT matrix during the evaporation of DMF solvent.

Figure 3.2c was obtained after heat treatment to remove 73 wt% PS particles. Although some residual PS may be present, it was not observed by SEM. Rather, the CFME surface was covered with PS-derived pores, of size comparable to the original particles (500 nm). Inside the matrix, shown in Figure 3.3c, macropores were distributed throughout the CNT layer, mostly in a close-packing pattern. However, few pores were apparent near the inner interface with the carbon fiber, consistent with Figure 3.3b, again indicating that the PS particles did not distribute evenly through the CNT layer prior to heat treatment.

Images of the CFMEs after application of enzymatic hydrogel catalyst are shown in Figure 3.2d and 3.3d. From previous estimations, a CNT layer of 2 μg cm^{-1} loading can contain up to 6.2 μg cm^{-1} hydrogel.[21] The hydrogel loading in Figure 3.2d (13 μg cm^{-1}) almost doubled this value, yielding a surface morphology that appears much smoother than the freshly heat-treated CFMEs. The cross-sectional view in Figure 3.3d shows that hydrogel successfully infiltrated and almost completely filled the pores of CNT matrix. For the purpose of microscopy, this was a dry, unhydrated gel and was expected to swell approximately two fold upon hydration, and thus completely filled the matrix.[38]

3.4.2 Effect of heat treatment on coating morphology and surface area

Polystyrene particles were subsequently removed by heat treatment at 450 °C for 4 hours. At this temperature, polystyrene gradually melts and burns away.[30] Optical microscopy was used to observe CFMEs before and after heat treatment for varying PS loadings, as shown in Figure 3.4. The images were taken so that the same site at the same angle was observed to indicate the change in coating morphology due to heat treatment. The PS-free CFME showed no change in morphology, indicating that CNTs survived the 450 °C heat-treatment.

Thickness measurements both before and after heat treatment are summarized in Figure 3.5, with error bars representing sample roughness. CFME thickness with no incorporated PS beads did not change, within measurement error, due to heat treatment; the same is true for a PS loading of 29 wt%. For higher loadings of 59 and 73 wt %, a significant thickness reduction was observed. Also shown is predicted thickness prior to heat treatment, calculated using component densities and mass fractions, and assuming that the PS beads were close packed. It can be seen that the measured result and predicted thickness match within roughness error. Even though the SEM cross-sections (Figure 3.3b) showed that the PS bead distribution is not homogeneous throughout the film, the assumption of close packing appears here to be a reasonable approximation.

Some loss of CNTs is expected due to removal of the PS beads. However, the heat treatment step is not detrimental to the NT layer itself, as evidenced by the fact that, in cases of no PS template, the CNT layer thickness is maintained (Figure 3.5), and the CNT surface area after heat treatment (0.5 ± 0.2 cm^2) matches that of electrodes that experienced no heat treatment (0.55 ± 0.1 cm^2).[21] It has also been previously been shown by thermogravimetric analysis that multiwall CNTs are stable up to 500°C.[34] Moreover, the observed surface area increases with increasing PS bead loading (Figure 3.5b). Thus we rule out significant NT loss due to heat treatment.

3.4.3 Capacitive surface area

Due to the small scale of the electrode, electrochemical capacitance measurements were used to quantify CFME surface area, after removal of the PS template by heat treatment. Moreover, capacitance is more directly relevant to electrochemical properties, because it accounts for electronic conductivity, hydrophilicity and infiltration of electrolyte. As summarized in Figure 3.5b, increasing the mass fraction of the PS template tended to increase the capacitive surface area, such that introduction of the PS template at 74 wt% led to a doubling of the capacitive surface area compared to the PS-free samples. The PS-derived macropores therefore improved the accessibility of CNT surfaces, even though the observed CNT matrix thickness did not change. Such observations can be explained by loss of external CNTs with the removal of the PS beads during heat treatment. The remaining CNTs, although having similar thicknesses, retained higher porosity, as revealed by SEM images (Figure 3.3c) and therefore higher transport efficiency.

PS mass fractions above 73 wt% led to non-dense packing (Figure 3.1d-e) with insufficient CNTs to fill voids between the PS beads. One such sample was made at 79 wt% PS, as plotted in Figure 3.5b. As expected, this sample showed reduced surface area comparing to dense-packing samples.

3.4.4 Electrochemical characterization

A biocatalyst hydrogel consisting of glucose oxidase, redox polymer and crosslinker was coated on the PS modified CFME as an electrochemical characterization platform. Redox polymer tests in the absence of glucose (Figure 3.6a) again showed a doubling of peak current density due to the introduction of the PS template at 74 wt%. Peak separation also increases with peak height, an effect we have previously attributed to contact resistance within the electrode.[21] The observed dependence corresponds to an ohmic resistance of 24 $\Omega \cdot cm^2$, which is lower than previous results (40 $\Omega \cdot cm^2$) due to improvements in electrode construction.

In the presence of glucose (Figure 3.6b), plateau current density at a CNT loading of 2 μg cm^{-2} with no PS template was comparable to previous results (4.1 ± 0.8 mA cm^{-2} *vs.* 3.5 mA cm^{-2}) within error. [21] Plateau current density was also doubled due to the introduction of 74 wt% PS, with minimal variation in half-wave potential. Performance improvement was therefore not compromised by transport limitations within the porous matrix, and appeared to vary linearly with PS loading (Figure 3.6 insets), suggesting that increased plateau current density is directly related to increased accessible surface area, as shown in Figure 3.5b.

3.5 Conclusions

Introducing macropores via PS particle templating was shown to increase accessible surface area and improve performance of a biocatalyzed CFME. Introduction of the PS particle template at 74 wt%, corresponding to close packing of the PS particles with dense NT packing, led to a doubling of the capacitive surface area as compared to the untemplated samples. The templated CNT CFMEs displayed peak redox polymer and enzymatic activity properties that also doubled as compared to untemplated CNT electrodes. The hydrophilicity of the carboxylated CNT layer enabled total infiltration of biocatalytic hydrogel, as revealed by FIB-SEM. This simple procedure enables the fabrication of hierarchical multiscale porous carbon electrodes that are scalable to other applications.

3.6 Figures

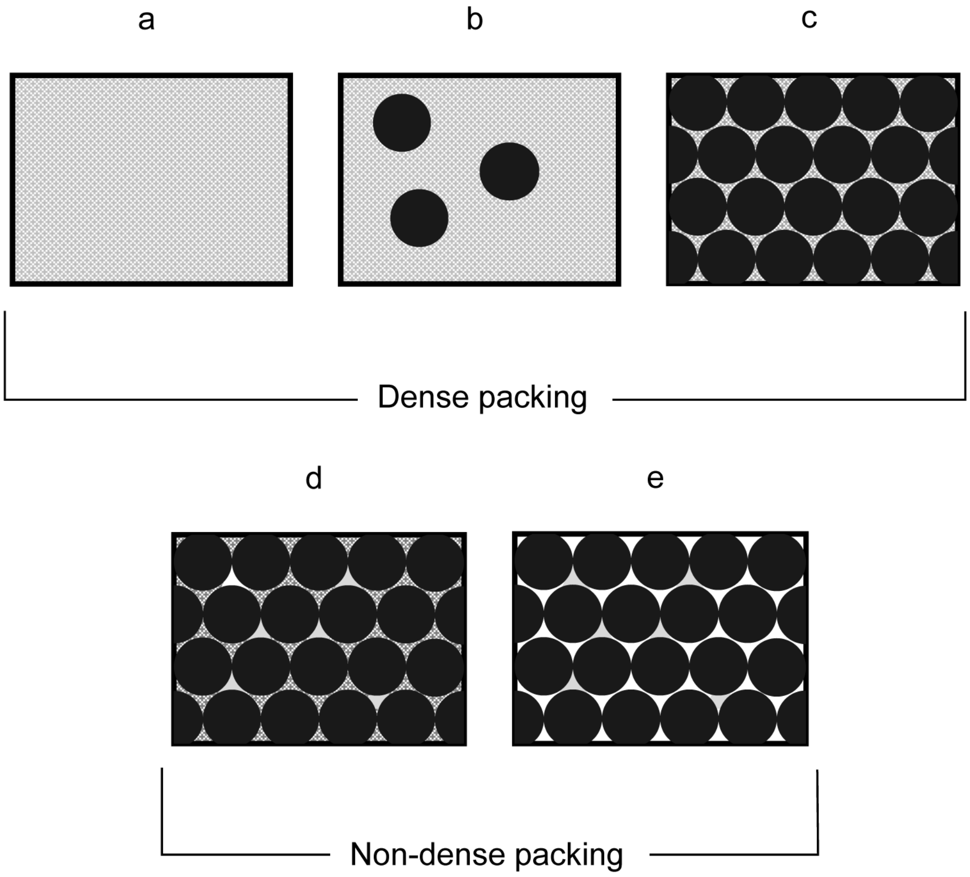

Figure 3.1 Schematics of PS packing within a CNT matrix. a) CNT matrix alone; b) PS sparsely distributed within the CNT matrix; c) PS close packed (74 vol%), with voids completely filled by CNT matrix; d) PS close-packed, with incomplete filling by CNT matrix; e) PS only.

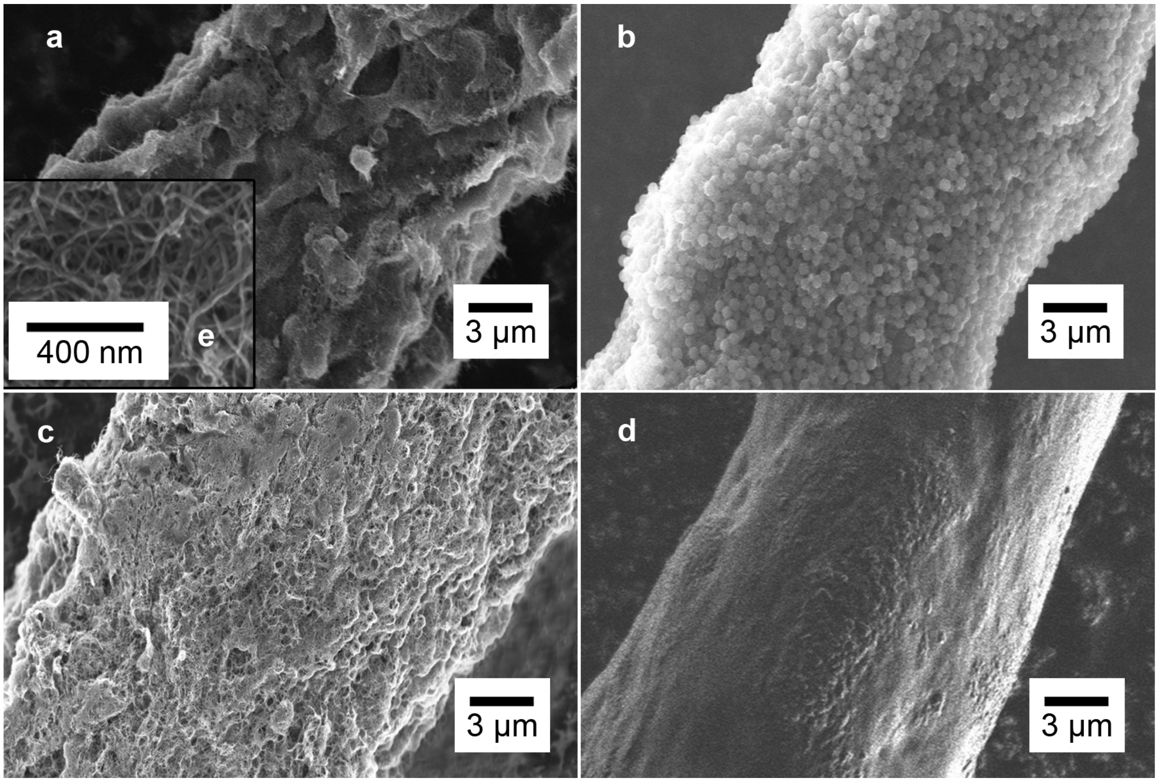

Figure 3.2 Scanning electron micrographs of CFMEs at different preparation stages. a) CNT coating (no PS particles) at 2 µg cm^{-1}, inset: magnified view showing CNT matrix pores; b) PS+CNT coating at PS mass fraction of 73 wt%; c) PS+CNT coating after heat treatment. d) Hydrogel coated CFME at loading of 13 µg cm^{-1}; e) Inset showing amplified view of the CNT matrix.

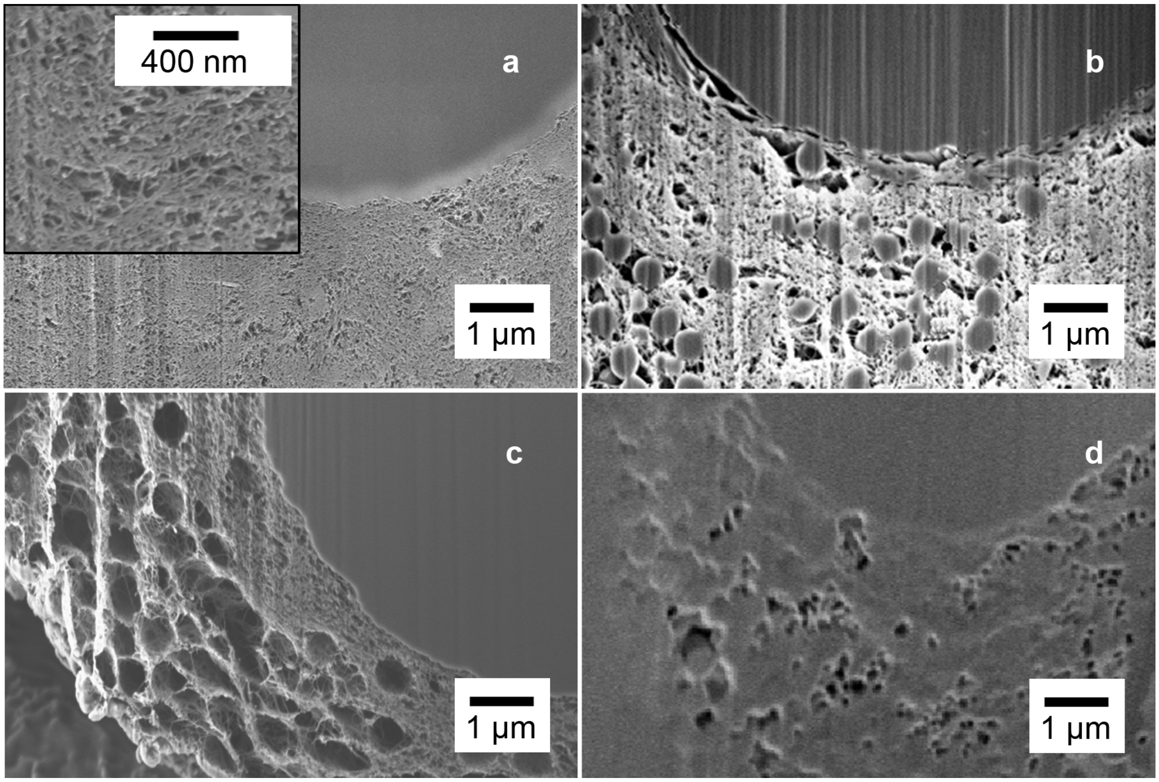

Figure 3.3 Scanning electron micrographs of the focused ion beam revealed cross sections. Samples are: a) CNT coating (no PS particles) at 2 µg cm^{-1}, inset: magnified view showing CNT matrix pores; b) PS+CNT coating at PS mass fraction of 73 wt%; c) PS+CNT coating after heat treatment. d) Hydrogel coated CFME at loading of 13 µg cm^{-1}. Vertical lines, especially those in (b), are artifacts from the ion beam polishing; e) Inset showing amplified view of the CNT matrix.

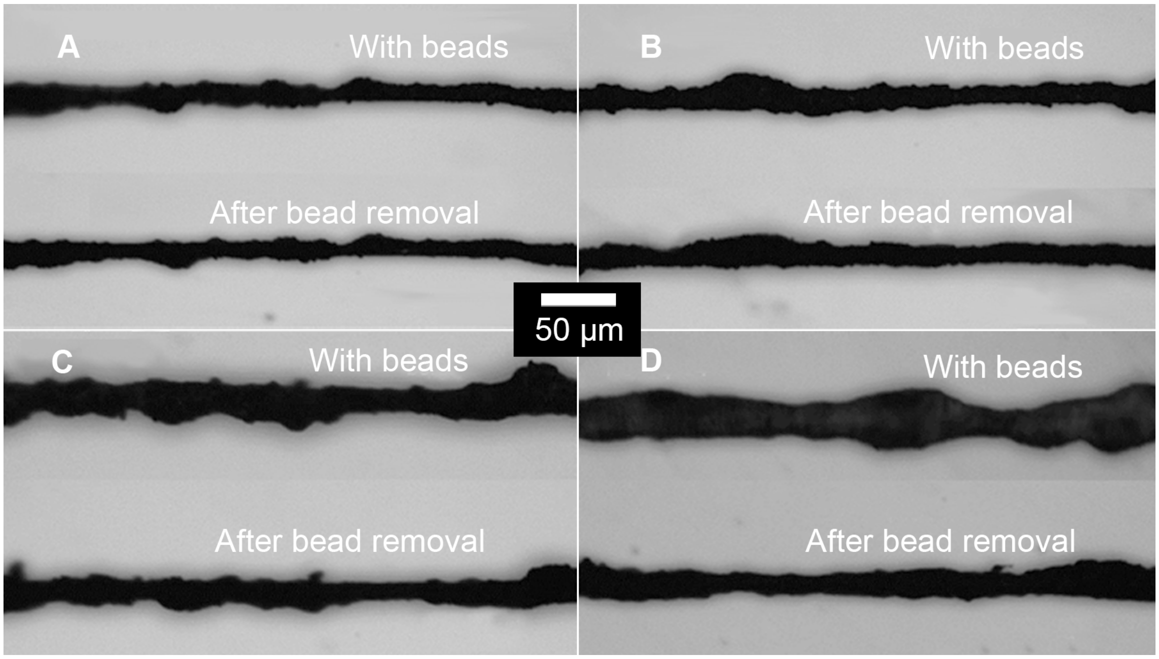

Figure 3.4 Optical micrographs of CFMEs with PS particles and after particle removal with heat treatment at varying PS mass fractions. The same angle at the same spot was observed to represent morphological changes. Corresponding mass fractions are a) CNTs alone; b) 28 wt% PS; c) 58 wt% PS; d) 73 wt% PS; CNT loading was fixed at 2 μg cm^{-1}.

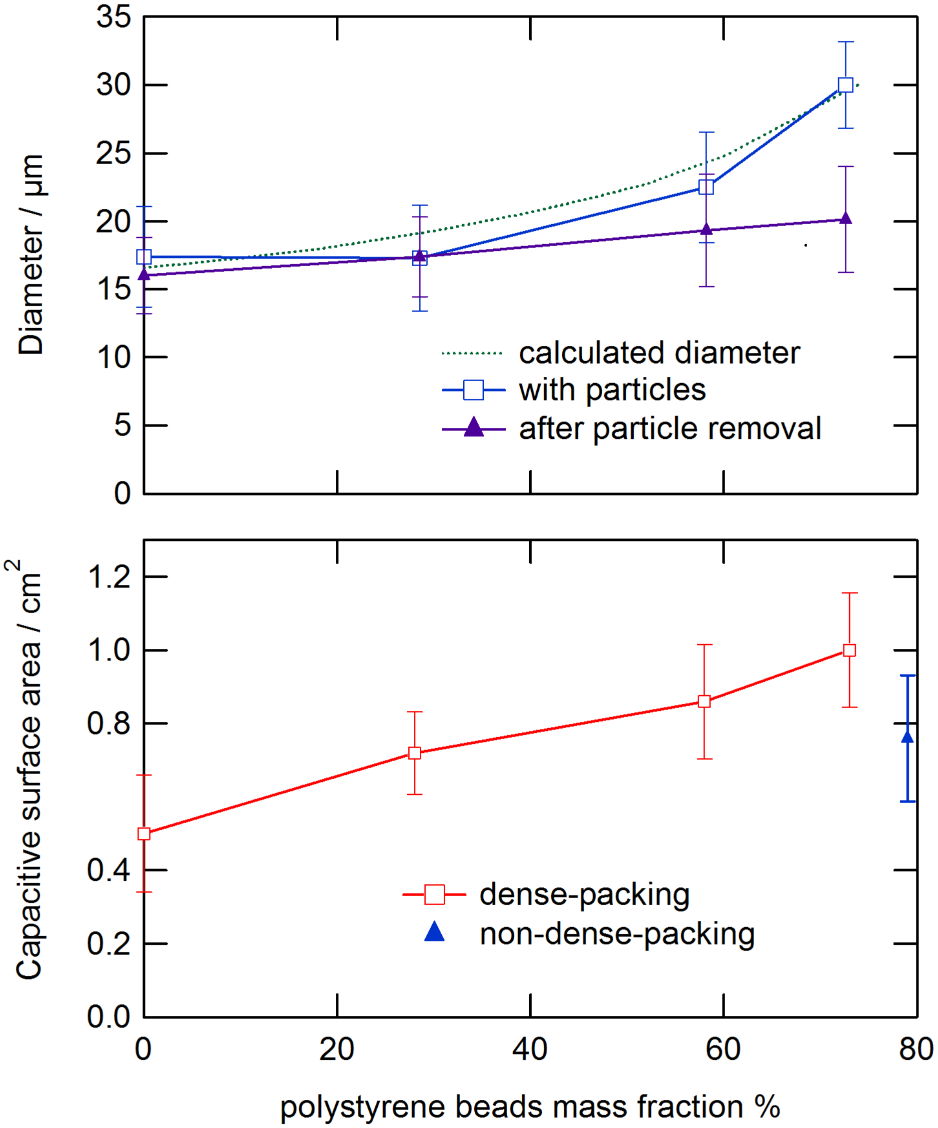

Figure 3.5 Morphology trend of templated CNT-modified CFMEs. a) PS/CNT CFME diameter before and after particle removal, estimated from the images of Fig. 4. Also shown is calculated diameter based on density estimates. b) Capacitive surface area of PS/CNT CFMEs after bead removal with heat treatment. CNT loading mass was fixed at 2 µg cm^{-1}. Capacitance obtained by cyclic voltammetry in the 0.4 to 0.5 V/Ag|AgCl range in phosphate buffer solution, pH 7.0, 25°C. Surface area was calculated from capacitance assuming a specific capacitance of 25 µF cm$^{-2.}$

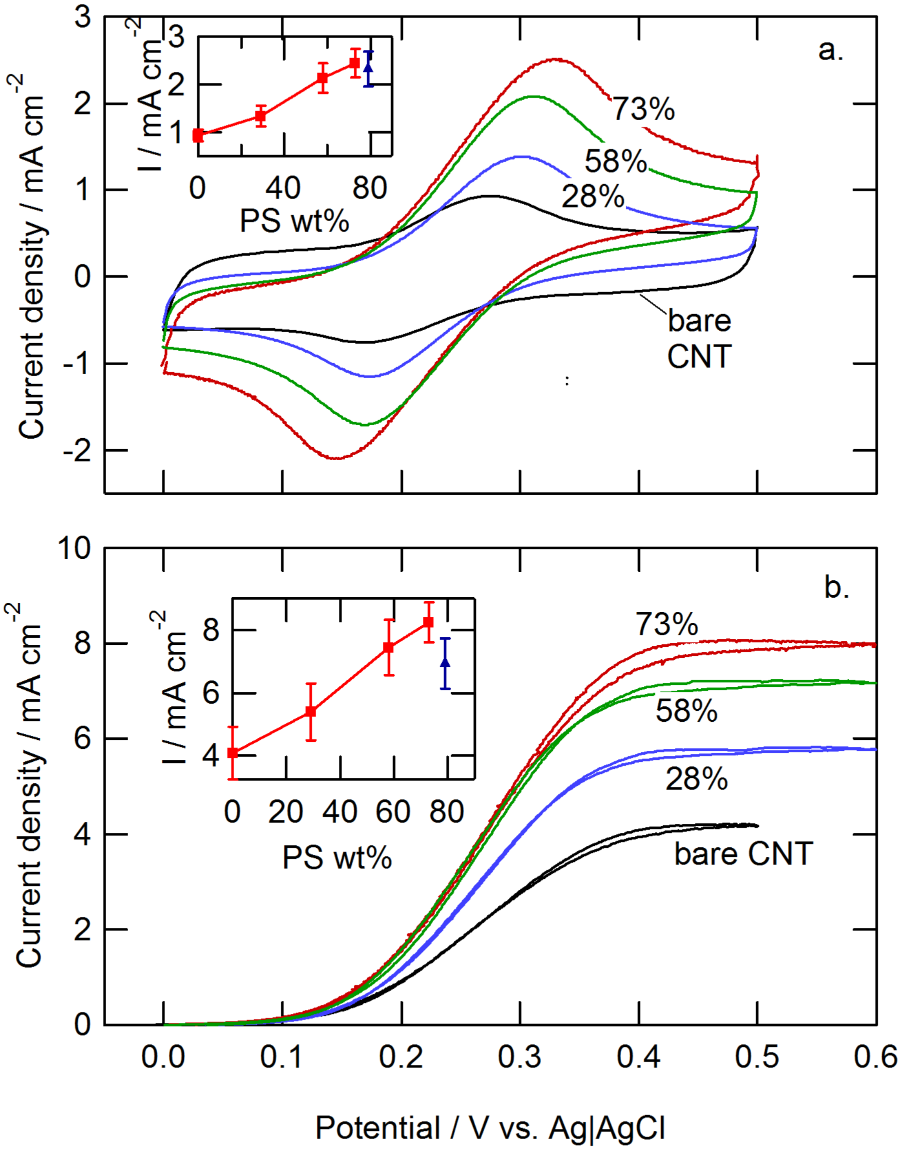

Figure 3.6 Electrochemical response of glucose bioelectrodes supported on templated CNT-modified CFMEs at varying initial PS mass fractions. **a)** Redox polymer voltammetry in N_2-purged PBS, pH 7.0, 37.5°C, glucose-free, 50 mV/s scan rate. **Inset:** redox polymer peak height vs. PS mass fraction; **b)** Glucose oxidation with 50 mM glucose, 1 mV/s scan rate. The samples were all loaded with 26 µg cm^{-1} hydrogel with 39.6 wt% GOx, 59.5 wt% redox polymer and 0.9 wt% PEGDGE. Inset: glucose oxidation plateau current density vs. PS mass fractions. The triangle (▲) in each inset represents the non-dense-packing case (Fig. 1d).

REFERENCES

References

1. I. Willner, Y.-M. Yan, B. Willner and R. Tel-Vered, "Integrated Enzyme-Based Biofuel Cells-A Review" *Fuel Cells*, **9**(1), 7-24 (2009).

2. S. Calabrese Barton, J. Gallaway and P. Atanassov, "Enzymatic Biofuel Cells for Implantable and Microscale Devices" *Chemical Reviews*, **104**(10), 4867-4886 (2004).

3. B.A. Gregg and A. Heller, "Redox polymer films containing enzymes. 1. A redox-conducting epoxy cement: synthesis, characterization, and electrocatalytic oxidation of hydroquinone" *The Journal of Physical Chemistry*, **95**(15), 5970-5975 (1991).

4. T. Nöll and G. Nöll, "Strategies for "wiring" redox-active proteins to electrodes and applications in biosensors, biofuel cells, and nanotechnology." *Chemical Society Reviews*, **40**(7), 3564-76 (2011).

5. N. Mano, F. Mao and A. Heller, "Characteristics of a miniature compartment-less glucose-O2 biofuel cell and its operation in a living plant." *Journal of the American Chemical Society*, **125**(21), 6588-94 (2003).

6. F. Mao, N. Mano and A. Heller, "Long tethers binding redox centers to polymer backbones enhance electron transport in enzyme "Wiring" hydrogels." *Journal of the American Chemical Society*, **125**(16), 4951-7 (2003).

7. M.J. Cooney et al., "Design of chitosan gel pore structure: towards enzyme catalyzed flow-through electrodes" *Journal of Materials Chemistry*, **18**(6), 667 (2008).

8. J. Kim, H. Jia and P. Wang, "Challenges in biocatalysis for enzyme-based biofuel cells." *Biotechnology advances*, **24**(3), 296-308 (2006).

9. S. Calabrese Barton, Y. Sun, B. Chandra, S. White and J. Hone, "Mediated Enzyme Electrodes with Combined Micro- and Nanoscale Supports" *Electrochemical and Solid-State Letters*, **10**(5), B96 (2007).

10. S. Calabrese Barton, H.-H. Kim, G. Binyamin, Y. Zhang and A. Heller, "The "Wired" Laccase Cathode: High Current Density Electroreduction of O_2 to Water at +0.7 V (NHE) at pH 5" *Journal of the American Chemical Society*, **123**(24), 5802-5803 (2001).

11. S. Calabrese Barton, H.-H. Kim, G. Binyamin, Y. Zhang and A. Heller, "Electroreduction of O_2 to Water on the "Wired" Laccase Cathode" *The Journal of Physical Chemistry B*, **105**(47), 11917-11921 (2001).

12. D. Ivnitski, B. Branch, P. Atanassov and C. Apblett, "Glucose oxidase anode for biofuel cell based on direct electron transfer" *Electrochemistry Communications*, **8**(8), 1204-1210 (2006).

13. T. Chen et al., "A Miniature Biofuel Cell" *Journal of the American Chemical Society*, **123**(35), 8630-8631 (2001).

14. N. Mano, F. Mao and A. Heller, "A Miniature Biofuel Cell Operating in A Physiological Buffer" *Journal of the American Chemical Society*, **124**(44), 12962-12963 (2002).

15. M.W. Verbrugge, "Modeling Lithium Intercalation of Single-Fiber Carbon Microelectrodes" *Journal of The Electrochemical Society*, **143**(2), 600 (1996).

16. M.W. Verbrugge, "Lithium Intercalation of Carbon-Fiber Microelectrodes" *Journal of The Electrochemical Society*, **143**(1), 24 (1996).

17. M.V. Pishko, A.C. Michael and A. Heller, "Amperometric glucose microelectrodes prepared through immobilization of glucose oxidase in redox hydrogels" *Analytical Chemistry*, **63**(20), 2268-2272 (1991).

18. F. Gao, L. Viry, M. Maugey, P. Poulin and N. Mano, "Engineering hybrid nanotube wires for high-power biofuel cells" *Nature Communications*, **1**(1), 1-7 (2010).

19. R.-sheng Chen, W.-hua Huang, H. Tong, Z.-li Wang and J.-ke Cheng, "Carbon fiber nanoelectrodes modified by single-walled carbon nanotubes." *Analytical Chemistry*, **75**(22), 6341-5 (2003).

20. X. Zhao, X. Lu, W.T.Y. Tze and P. Wang, "A single carbon fiber microelectrode with branching carbon nanotubes for bioelectrochemical processes." *Biosensors & Bioelectronics*, **25**(10), 2343-50 (2010).

21. H. Wen, V. Nallathambi, D. Chakraborty and S. Calabrese Barton, "Carbon fiber microelectrodes modified with carbon nanotubes as a new support for immobilization of glucose oxidase" *Microchimica Acta*, **175**(3-4), 283-289 (2011).

22. O.D. Velev and E.W. Kaler, "Structured Porous Materials via Colloidal Crystal Templating: From Inorganic Oxides to Metals" *Advanced Materials*, **12**(7), 531-534 (2000).

23. O. Velev, T. Jede, R. Lobo and A. Lenhoff, "Porous silica via colloidal crystallization" *Nature*, **389**447–448 (1997).

24. F. Iskandar et al., "Enhanced Photocatalytic Performance of Brookite TiO_2 Macroporous Particles Prepared by Spray Drying with Colloidal Templating" *Advanced Materials*, **19**(10), 1408-1412 (2007).

25. B.T. Holland, L. Abrams and A. Stein, "Dual Templating of Macroporous Silicates with Zeolitic Microporous Frameworks" *Journal of the American Chemical Society*, **121**(17), 4308-4309 (1999).

26. P. Jiang, J. Cizeron, J.F. Bertone and V.L. Colvin, "Preparation of Macroporous Metal Films from Colloidal Crystals" *Journal of the American Chemical Society*, **121**(34), 7957-7958 (1999).

27. O. Velev, P. Tessier, A. Lenhoff and E. Kaler, "A class of porous metallic nanostructures" *Nature*, **401**(6753), 548 (1999).

28. V. Flexer, N. Brun, R. Backov and N. Mano, "Designing highly efficient enzyme-based carbonaceous foams electrodes for biofuel cells" *Energy & Environmental Science*, **3**(9), 1302 (2010).

29. A. Imhof and D. Pine, "Ordered macroporous materials by emulsion templating" *Nature*, **389**(6654), 948–950 (1997).

30. G. Subramanian, V.N. Manoharan, J.D. Thorne and D.J. Pine, "Ordered Macroporous Materials by Colloidal Assembly: A Possible Route to Photonic Bandgap Materials" *Advanced Materials*, **11**(15), 1261-1265 (1999).

31. Y. a. Vlasov, M. Deutsch and D.J. Norris, "Single-domain spectroscopy of self-assembled photonic crystals" *Applied Physics Letters*, **76**(12), 1627 (2000).

32. H. Chang, S.H. Joo and C. Pak, "Synthesis and characterization of mesoporous carbon for fuel cell applications" *Journal of Materials Chemistry*, **17**(30), 3078 (2007).

33. G.S. Chai, I.S. Shin and J.-S. Yu, "Synthesis of Ordered, Uniform, Macroporous Carbons with Mesoporous Walls Templated by Aggregates of Polystyrene Spheres and Silica Particles for Use as Catalyst Supports in Direct Methanol Fuel Cells" *Advanced Materials*, **16**(22), 2057-2061 (2004).

34. D. Bom et al., "Thermogravimetric Analysis of the Oxidation of Multiwalled Carbon Nanotubes: Evidence for the Role of Defect Sites in Carbon Nanotube Chemistry" *Nano Letters*, **2**(6), 615-619 (2002).

35. K. Kinoshita, "*Carbon: electrochemical and physicochemical properties*" 533 (Wiley: Hoboken, 1988).

36. G. Binyamin, "Stabilization of Wired Glucose Oxidase Anodes Rotating at 1000 rpm at 37°C" *Journal of The Electrochemical Society*, **146**(8), 2965 (1999).

37. O. Zaborsky, "The immobilization of glucose oxidase via activation of its carbohydrate residues" *Biochemical and Biophysical Research Communications*, **61**(1), 210-216 (1974).

38. A. Aoki, R. Rajagopalan and A. Heller, "Effect of quaternization on electron diffusion coefficients for redox hydrogels based on poly(4-vinylpyridine)" *The Journal of Physical Chemistry*, **99**(14), 5102-5110 (1995).

Chapter 4 Simulation of Porous Rotating Disk Electrode with Convection and Diffusion Processes

4.1 Abstract

A model based on convective and diffusive transport of reactants in a porous rotating disk electrode (PRDE) is described. This model includes consideration of diffusion and ambient convection to account for experimentally observed non-zero current at low rotation speeds, while retaining sigmoidal dependence of current density on disk rotation rate at constant potential. The model also considers concentration and velocity fields in the electrolyte adjacent to the PRDE, which can limit overall transport of reactant. Model-generated polarization results are compared to experiment to yield estimates of transport and kinetic parameters in the PRDE. The effects of various system parameters have been explored, elucidating the effect of each parameter on rotation speed and potential dependence.

4.2 Introduction

Porous electrodes are of major interest to fuel cell and battery researchers due to their high surface area, which serves as a heterogeneous reaction interface and significantly improves area specific resistance and overall current density.[1–5] Porous electrodes have thus found wide applications in all kinds of energy generation devices, including batteries, solar cells, supercapacitors, and bioreactors.[6] As the most widely used portable energy source, lithium ion batteries require high surface area electrodes to store/intercalate and discharge/deintercalate lithium ions at both cathodes and anodes.[7–12] Solar cells utilize porous materials for photo-excited electron collection. For example, dye-sensitized solar cells invented by Gratzel utilize porous TiO_2 nanocrystalline films, which were coated with light absorbing dyes, to efficiently collect exited electrons.[13–17] Bioreactors take advantage of the high surface area to conduct maximum conversion within limited volume.[6,18–20] Porous carbon supports have also been widely used for biofuel cell electrodes. In Chapter 2 and 3, carbon nanotube based carbon fiber microelectrodes were demonstrated for glucose oxidase catalyzed glucose oxidation. Porous electrodes have been widely applied as biocatalyst support for biosensors and biofuel cells.[21–25]

To characterize porous media as electrode support, it is commonly carried out to attach a porous electrode onto a flat RDE to study the electrochemical responses (PRDE).[26–34] These electrodes are rotated to bring substrate to the active sites, and the rotation rate is usually maintained at high values to minimize mass transport limitations. Nam et al. studied mass transport within PRDEs with the assumption of first order kinetics and convection as the only transport mechanism at high rotation, with diffusion only dominant at low rotations.[27,35] They predicted the general behavior of PRDE current output as a function of rotation speed, which shows a sigmoidal trend with increasing rotation rate. As shown in Nam's publication, such assumptions led to results agree very well with couple of experiments where zero currents were observed at low rotations.[26]

Nam's work, however, makes two overly simplistic assumption: one, linear kinetics, which is not applicable in enzymatic nonlinear systems; two, diffusion only considered in low rotations that only the surface of the PRDE is active enough to have any concentration gradient. When applied to a recently-studied glucose oxidase anode supported on a porous carbonaceous monolith, it failed to be applicable in two aspects.[36,37] First, the system was catalyzed by glucose oxidase, and the resulting reaction kinetics were not linear at higher glucose concentrations. At concentrations much larger than Michaelis-Menten constant, the reaction rate was independent of glucose concentration. Second, Nam assumed that diffusion is only important at low rotation regime where the low rotation is defined when the rotation rate ω gives value of T_r^{∞} to be less than 0.3, which is defined by the following expression:

$$T_r^{\infty} = \frac{2k\omega^2}{k_r \nu} \tag{1}$$

where k is the permeability, k_r is the first order reaction rate, and ν is the kinematic viscosity.

Thus diffusion was not included for high rotation cases. However, since axial velocity within PRDE always reduces to zero at the vicinity of current collector backend, diffusion dominates in this region, thus it is necessary to include diffusion in all rotations.

This work attempts to explain Flexer's data by the inclusion of both convection and diffusion of glucose substrate at all the rotations. It addressed the non-zero current at lower rotation, and the sigmoidal shape that's typical of PRDEs. Moreover, external convection in the electrolyte at low rotations was included in the model since the boundary layer thickness beyond which bulk substrate concentration is maintained is no longer at the PRDE surface at low rotations.

4.3 Mathematical Model

The proposed model follows the scheme shown in Figure 4.1. PRDE rotation results in convection both internal and external to the porous layer. Reactants are initially drawn towards the PRDE by both convection and diffusion, enter the PRDE, and flow through while being consumed by the reaction. As shown in Appendix A.1, axial flow velocity is only a function of axial position, *z*, thus the problem can be simplified to 1D.[38,39]

4.3.1 Velocity field within PRDE

The velocity field within the porous layer has been solved by Joseph utilizing the similarity variables introduced by von Karman:[39,40]

$$\begin{bmatrix} q_r \\ q_\theta \\ q_z \end{bmatrix} = -\frac{k\omega^2}{v}\begin{bmatrix} -r \\ 2rk\omega / v \\ 2z \end{bmatrix} \quad (2)$$

where k is permeability, v is kinematic viscosity, z is axial position, and r is radial position. The expression is valid for an infinitely large porous disk. This is a good approximation for a thin PRDE attached to an RDE surface. This solution does not consider boundary between PRDE and electrolyte since the suction of electrolyte at the interface is a natural result induced by rotation.

4.3.2 Velocity field in the electrolyte

As shown in Appendix A.1, Stuart described the axial velocity field q_{ze} in electrolyte as a function of axial position by solving a boundary value differential equation group. The boundary value problem treated the suction speed a as an independent parameter. Dimensionless axial velocity H at PRDE / electrolyte surface, together with the definition of H, leads to the definition of a:

$$a = \frac{q_{ze}\big|_{z=h}}{\sqrt{v\omega}} \quad (3)$$

where v is kinematic viscosity of water, ω is rotation rate, and q_{ze} is dimensional velocity in electrolyte. However, with two additional conditions for any PRDE system:

$$\begin{aligned} &\varepsilon \bullet q_z\big|_{z=h} = q_{ze}\big|_{z=h} \\ &q_z = -2z\frac{k\omega^2}{v} \end{aligned} \quad (4)$$

where ε is the porosity, k is permeability, and z is axial position with z=0 defined as the PRDE top surface in contact with electrolyte (thus it is z-h when discussing PRDE and electrolyte together). Thus, for a PRDE system, the surface suction parameter, a, can be expressed as

$$a = \left(\frac{\omega}{v}\right)^{\frac{3}{2}} \bullet 2k\varepsilon h \tag{5}$$

Hence, for any given PRDE test system, with knowledge of porous media thickness, permeability, porosity, and water viscosity, the suction parameter varies with rotation rate. Eq. 12 may also be used to estimate the range of applicable values of a for this analysis.

The velocity field external to the disk may then be described as a function of a (see Appendix A.1). The reactant concentration profile within electrolyte is well controlled by Schmidt number:

$$Sc = v / D \tag{6}$$

where D is the reactant diffusivity and ν is kinematic viscosity. The effect will be discussed later.

When the PRDE reaction rate is limited by reactant mass transfer, with linear reaction kinetics, the following governing equation is applicable:

$$0 = \frac{1}{Sc}\frac{d^2\Theta}{d\zeta^2} - H(\zeta, a)\frac{d\Theta}{d\zeta} \tag{7}$$

where $\Theta = c/c_\infty$ is the dimensionless reactant concentration, c is the local reactant concentration, c_∞ the bulk concentration. Definitions of other parameters can be found in Table 4.3.

Boundary conditions:

$$\begin{aligned}\Theta(\zeta = 0) = 0\\ \Theta(\zeta = \infty) = 1\end{aligned} \tag{8}$$

where ζ=0 is the surface of PRDE in contact with bulk electrolyte. The boundary layer thickness ζ_{bl} can then be defined as:

$$\Theta(\zeta = \zeta_{bl}) = 0.99 \tag{9}$$

Another important dependent variable in this analysis is the dimensionless mass transfer at the PRDE surface, which is defined as:

$$\varphi = \frac{1}{Sc}\frac{d\Theta}{d\zeta}\Big|_{\zeta=0} \tag{10}$$

where 1/Sc can be considered a dimensionless diffusivity.

4.3.3 Boundary value problem setup

The boundary value problem setup includes two governing equations and boundary condition at left (current collector), middle (RDE/electrolyte interface), and right (boundary layer thickness).

Governing equation in PRDE.

$$-\varepsilon R(c)+D_{eff}\frac{d^2c}{dz^2}-q_z\varepsilon\frac{dc}{dz}=0 \tag{11}$$

Governing equation in electrolyte

$$D_0\frac{d^2c}{dz^2}-q_{ze}\frac{dc}{dz}=0 \tag{12}$$

where ε is porosity, *R(c)* is PPBB kinetic reaction rate (described below); D_{eff} is effective diffusivity of substrate within PRDE.[20] q_{z} and q_{ze} are the axial velocity profiles internal and external to the porous layer, respectively; *z* is axial position; and D_0 is the intrinsic reactant diffusivity in the electrolyte. It should be noted that q_{z} and q_{ze} are both functions of *z*. Details of the axial velocity profiles can be found in Appendix.

Boundary condition at the current collector (left):

$$\frac{dc}{dz}=0\Big|_{z=0} \tag{13}$$

Boundary condition at the PRDE/electrolyte interface (middle):

$$\varepsilon\bullet q_z\big|_{PRDE}=q_{ze}\big|_{electrolyte} \tag{14}$$

$$D_{eff}\frac{\partial c}{\partial z}+q_z\varepsilon c=q_{ze}c+D_0\frac{\partial c}{\partial z} \tag{15}$$

$$D_{eff} = D_0 \bullet \varepsilon^{3/2} \bullet \phi \tag{16}$$

Electrolyte boundary layer:

$$c = c_\infty \tag{17}$$

where ϕ is the permeability of hydrogel. As discussed by Gehrke et al., the permeability of hydrogels are affected by gel crosslinking and swallowing.[41] The details of these effects are outside the discussion in the current work. Instead, phenomenal effect as a correction factor was studied. Effective diffusivity varies with porosity to the 3/2 power according to Bruggeman's correction law.[42] Eq. 23 represents a material balance at the electrode-electrolyte interface.

4.3.4 Kinetic reaction and velocity field

The reaction rate follows enzymatic ping-pong bi bi mechanism:

$$R(c) = \frac{V_{\max}}{1 + K_m / M_O + K_s / c} \tag{18}$$

where K_m and K_s are the enzymatic kinetic parameters, $V_{\max}$ is maximum reaction rate, M_0 and c are the oxidized mediator and substrate concentrations respectively. The expression for oxidized mediator concentration, M_O, is obtained by assuming Nerstian fast redox kinetics:

$$E = E_0 + \frac{RT}{nF} \ln \frac{M_o}{M_R} \tag{19}$$

and

$$M_{total} = M_o + M_R \tag{20}$$

where E is the applied potential, E_0 is redox potential, M_{total} is the total concentration of redox polymer mediator centers.

For fitting purposes, the values of reaction parameters K_{m} and M_{total} were obtained from measurements of glucose oxidase anode previously studied in our group, and are shown in Table 4.2.Table 4.2 Parameter list

In order to compare the model to experiment, four parameters were chosen to be fitted: k , ϕ , $V_{\max}$ and K_s . They were chosen because they represent the transport behavior (k, ϕ) and kinetic behavior ($V_{\max}$, K_{s}). Permeability, k, can be calculated by measuring the mass flow through porous media under controlled pressure or concentration gradients and calculating via the basic definitions. For example, gas permeability tests by feeding gas on one side and measuring the permeated gas with gas chromotograph.[43] Hydrogel permeability can be measured by membrane permeation experiments where concentrations on either side of the hydrogel membrane is well-controlled.[41]

4.4 Results and discussion

4.4.1 Concentration profile at limiting current

The practical range of suction a is from 0 to 0.01, and that of Sc from 100 to 100000. For a typical value of Sc = 1000, dimensionless concentration profiles Θ vs ζ external to the PRDE and at limiting current are shown in Figure 4.2. In this figure, ζ=0 represents the PRDE-electrolyte interface. The full transport region can be approximately divided into two parts: one at large ζ, where convection dominates; one close to PRDE surface (small ζ), where diffusion dominates. The diffusion-dominated region has a straight-line profile, consistent with that of diffusion without any convection and reaction.

The boundary layer thickness is very sensitive to suction rate *a*. Large values of a shift the diffusion region closer to the PRDE interface. Dimensionless mass transport, as defined by Eq. 17, becomes significantly large at $a = 1$, as indicated by the steep slope near $\zeta= 0$.

4.4.2 *Effect of Schmidt number and suction on limiting mass transfer rate on PRDE surface*

As shown in Figure 4.3, the mass transport at PRDE / electrolyte surface shows a sigmoidal shape with increasing Schmidt number. It helps by taking a look at Eq. 14 to understand the reason for such behavior. Although Eq. 14 contains term $H(\zeta,a)$ as a function of *a*, it doesn't vary significantly at the analyzed *a* ranging from 0 to 0.01 and has value close to $-0.5\zeta^2$. Thus the governing equation remains unchanged in small *Sc* and small *a* cases.

At extremely low Schmidt number, as shown in Eq.(27), diffusivity dominates, thus leading to invariant concentration profile. Similarly, for Schmidt numbers above 10^4, convection dominates, also resulting in a single term governing equation and thus an invariant mass flux. The Sc range between 1 to 10^4 is intermediate with both convection and diffusion contributing to mass transport.

Limiting current is independent of a for $a < 10^{-5}$ with small values of Sc. Suction dependence is only observed at high Sc and a values. This is expected, since a only affects convection, whereas small Sc indicates diffusion dominance. To make a clearer comparison, the difference in dimensionless limiting current for $a > 0$ as compared to $a = 0$ values were plotted, to generate Figure 4.4. It can be seen that $a \approx 10^{-3}$ can be used as a general criteria below which suction rate can be neglected in calculating mass transfer rate to the PRDE.

Limiting current calculation gave the upper limit for boundary layer thickness in subsequent calculations where the PRDE/electrolyte interface concentration is non-zero. That is, the boundary layer thickness estimated here can be used as the location where $c = c_\infty$ boundary condition shall be applied.

4.4.3 Concentration profile in the whole system

Substrate (*e.g.* glucose) concentration profiles under varying rotation rates is shown in Figure 4.5. At low rotations (10 s^{-1}, or 100 RPM), if no diffusion was considered, no reactant would enter the PRDE, resulting in zero current. In the current model, low rotations lead to a simple asymptotic case with fixed bulk concentration at PRDE outer surface, zero flux at inner surface, and chemical reaction in between. The effect of reaction rate constant on concentration profile is shown in Figure 4.7. When reaction rate is high (large $V_{\max}$ value), the active region of the electrode could be quite limited.

For all the cases calculated so far, the concentration profile in electrolyte is always uniform. It is due to the large difference in velocity field in PRDE and electrolyte. As shown in

Figure 4.8, the velocities in electrolyte quickly reach more than three orders of magnitude larger than that in PRDE. To further reveal the relationship, the ratio between the two velocities is:

$$\frac{q_{PRDE}}{q_{electrolyte}} = \frac{4hk}{(z-h)^2}\sqrt{\frac{\omega}{\nu}} \tag{21}$$

Thus smaller rotations actually lead to even larger deviation in velocities. Larger rotations would in effect decrease boundary layer thickness, thus making the concentration in electrolyte uniform.

As the rotation rate picks up, the concentration profile shows enhanced transport by convection. Since the convective velocity is largest near the PRDE-electrolyte interface, the convective effect is more obvious there. The inner (left) part is still dominated by diffusion due to the same reason, as shown by the 1000 s^{-1} blue curve. When rotation goes even higher, as exemplified by 10000 s^{-1}, the concentration become uniform throughout PRDE, as expected.

4.4.4 Comparison of models with and without diffusion considered

As shown in Figure 4.6, the concentration profile for diffusion and no diffusion cases were plotted for comparison. It can be seen that, at high rotations, the two cases is similar at PRDE top surface regions, indicating convection dominance. Low rotations lead to large deviations. Since the flow field is always zero at the vicinity of PRDE backend, substrate brought to this backend is always zero. Thus it can be concluded that the inclusion of diffusion at all rotations are necessary even if rotation rate is high.

Figure 4.14 shows the current density dependence on rotation rate. Detailed fitting process will be discussed later. The calculated result without diffusion inclusion is shown in the plot. Such model results in zero background current and lower current density at all rotations.

4.4.5 *Effect of parameters*

The current density was calculated from concentration profile by:

$$i = nF\left(\int_{\text{whole PRDE thickness}} R\left(c(z)\right)dz \right) \tag{22}$$

The effect of kinetic parameter V_{max} was shown in Figure 4.9. It can be seen that an increased V_{max} value leads to increased current density at all rotation rates, while the signature sigmoidal shape was maintained. The current density increase is almost proportional to V_{max}, due to the large K_{S} used, which leads to PPBB kinetics that's very close to first order reaction.

As shown in Figure 4.10, the applied potential dependence on the current densities were plotted. They are very typical idealized polarization curves for enzyme electrodes.[44] However, the assigned redox potential for redox mediators at 0.55 V does not show up in the curve as the half-wave potential. Instead, 0.53 V, with 0.02 V lower than the assigned value, was observed as the half-wave potential. The slight change is due to the concentration distribution within the PRDE.

Figure 4.11 shows the substrate concentration dependence. This curve has shifted expected Ks values due to concentration gradient within PRDE. Larger rotations lead to smaller gradient, thus closer apparent K_S as comparing to biocatalyst intrinsic reaction rates, as shown in Figure 4.11 bottom.

The effect of porous electrode thickness is shown in Figure 4.12. Larger thickness does not lead to an increased current density at lower rotation rates. This is due to the limited diffusion within the PRDE, leaving most of the inner porous media inactive. At higher rotation, the entire PRDE is active, thus the significantly increased current output.

Permeability affects the rotation dependence of current largely by dislocating the "onset rotation" where the current starts to increase faster with rotation, as shown in Figure 4.13. Larger permeability leads to smaller onset rotation. However, permeability doesn't change the actual lower and higher end of the output since it doesn't change the achievable kinetics.

4.4.6 Fitting to experimental results

The fitting curve and experimental results matched up very well, as shown in Figure 4.14. The system being fitted was glucose oxidase coated porous carbonaceous monolith at high (2910 μg cm^{-2}) and low (340 μg cm^{-2}) catalyst loadings. The fitting parameter values are summarized in Table 4.1.

The value of permeability, *k*, is lower than usual porous solid values at ~10^{-9} cm^2.[45] The hydrogel diffusivity correction factor is pretty close to previous measured values of 0.68 for dextran hydrogel.[41] $V_{\max}$ is much lower than our own previously measured value at 0.31 M/s. This is probably due to two reasons: First, the porous media significantly lowered the nominal volume reaction rate since the rate of reaction is actually averaged over the total system volume, and the catalyst contained within a fixed volume could thus be significantly less than pure catalyst hydrogel phases. Secondly, the nominal K_m value used deviates from the real value. For example, a K_m of 816 mM (10 fold increase) could leads to a fitted value of 0.8 mM/s for V_max. K_s also deviates from regular glucose oxidase constants at 13 mM. The irregularity of kinetic parameters is probably due to the usage of M_{total} and K_m from a different system. Measurements of M_total and k from the fitted system would reduce the number of unknowns to 2 and increase the certainty of estimated values of K_M and k_cat.

4.5 Conclusions

In the current work, a model based on convective and diffusive transport of reactants in porous rotating disk electrode was proposed. This model could explain the non-zero current at low rotation speeds, and still show the signature sigmoidal shape of PRDE current output versus rotation rate. Also explored are the concentration and velocity field in the electrolyte outside of PRDE, which could have a potential impact on the PRDE performance. Effect of various parameters have also been explored, giving some insight of how each part of the overall current vs. rotation curve were affected. Most importantly, the current model yields almost perfect fitting to PRDE experimental data, verifying its application.

The possible implementations of the current model could be extended to other researches on porous media. For example, polymer electrolyte membrane fuel cell coated on carbon fiber papers,[46] or bioreactors that utilize porous support to conduct bioconversions.[6,47] The advantage of the PRDE lies in its capability to control the mass transport within the porous media. Comparing to stationary porous electrodes, PRDEs have advections in addition to diffusion, thus studied the phenomena that could possibly maximize electrode performance. It is also relatively easy to fabricate by simply attaching a porous disk to a conductive surface, without having to worry about setting up proper fuel flow channels.

4.7 Tables

Table 4.1 Fitting parameter results

Parameter	**High loading**	**Low loading**
k, ×10^{-11} cm^{2}	5.24 ± 0.15	6.12 ± 1.52
ϕ	0.60 ± 0.0068	0.43 ± 0.024
V_{max}, mM/s	0.41 ± 0.0019	0.21 ± 0.0069
K_s, mM	106 ± 9.5	210 ± 108

Table 4.2 Parameter list

		Value	Ref.
c	Substrate concentration	Dependent variable	
c_{∞}	Substrate bulk concentration	100 mM	[1]
D_0	Glucose diffusivity in electrolyte	8.4×10^{-6} cm^2/s	[6] [48]
D_{eff}	Effective glucose diffusivity within PRDE		Eq. 6
E_0	Redox potential	0.55 V vs. Ag/AgCl	[1]
F	Faraday constant	96485 C/mol	
ε	Porosity	74 %	[1]
h	PRDE thickness	1 mm	[2]
k	PRDE permeability	To be fitted, initial value: 6×10^{-11} cm^2	[4]
ϕ	Hydrogel led diffusivity reduction	To be fitted, initial value: 0.68	[5]
K_m	Ping pong bi bi (PPBB) reaction constant	81.6 mM	
K_s	Substrate PPBB constant	To be fitted, initial value: 12 mM	
M_0	Oxidized mediator concentration		Eq. 8
M_{total}	Overall active mediator concentration	660 mM	
n	Reaction electron equivalent	2	
q_z	Velocity within PRDE.	Analytical solution available	Eq. 9
q_{ze}	Velocity within electrolyte	Solved numerically	[7]
R	Gas constant	8.314 J/mol/K	
$R(c)$	Rate of glucose oxidation reaction	PPBB kinetic expression	Eq. 8
T	Temperature	37 °C	[1]
U	Applied potential	0.5 V	[1]
ν	Kinematic viscosity of water	0.01 cm^2/s	
$V_{\max}$	Maximum enzymatic reaction rate	To be fitted, initial value: 0.4 mM/s	
ω	Rotation rate	Varied	[1]
z	Axial position	Independent variable	

Table 4.3 Intermediate parameter definitions

	Definition	Description
a	$(\omega / \nu)^{1.5} \bullet 2k\varepsilon h$	Suction parameter
Sc	ν / D	Schmidt number
Θ	c/c_∞	Dimensionless concentration
H	$q_z / \sqrt{\nu\omega}$	Dimensionless axial velocity
ζ	$\sqrt{\omega / \nu} \bullet (z-h)$	Dimensionless distance
φ	$(1/Sc) \bullet (d\Theta / d\zeta)\big\rvert_{\zeta=0}$	Dimensionless mass transfer

4.8 Figures

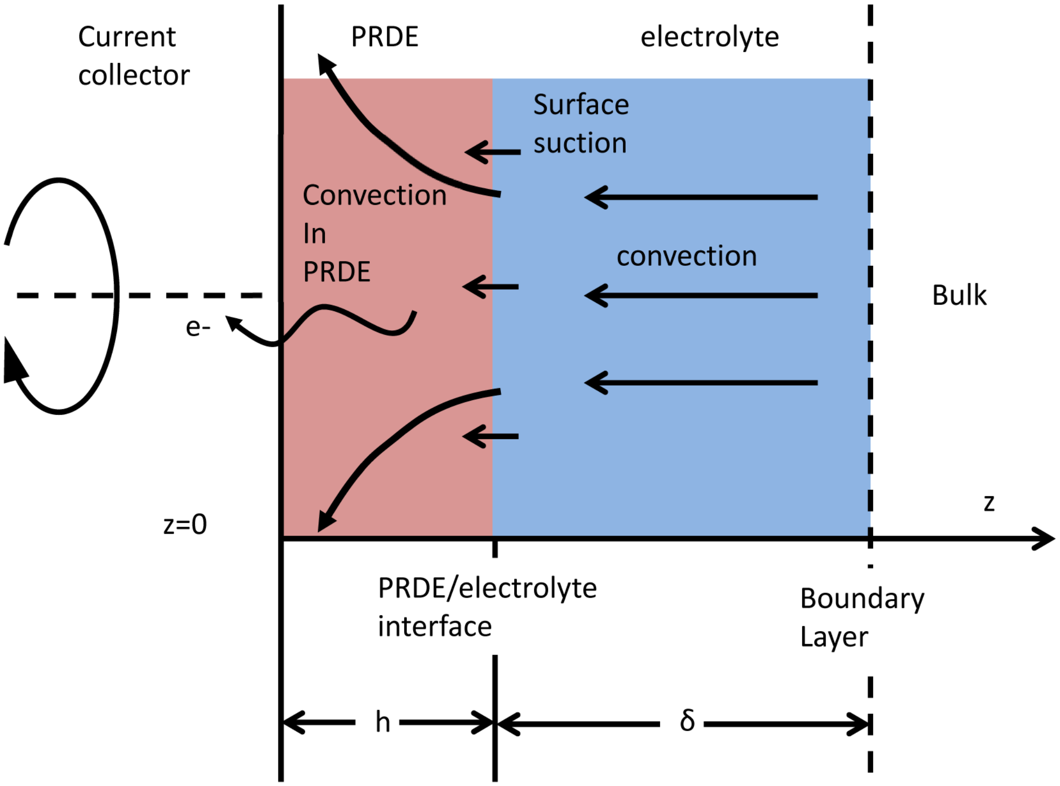

Figure 4.1 Schematics of convective diffusion model. Left part is porous rotating disk electrode at varying rotations. Convection happens both in and out of PRDE. PRDE/electrolyte interface has a continuous volumetric flow rate. The boundary layer is the region that concentration gradient exists and bulk concentration is maintained in electrolyte out of this region. Axial position was labeled as z. The thickness of PRDE and electrolyte bulk are h and δ respectively.

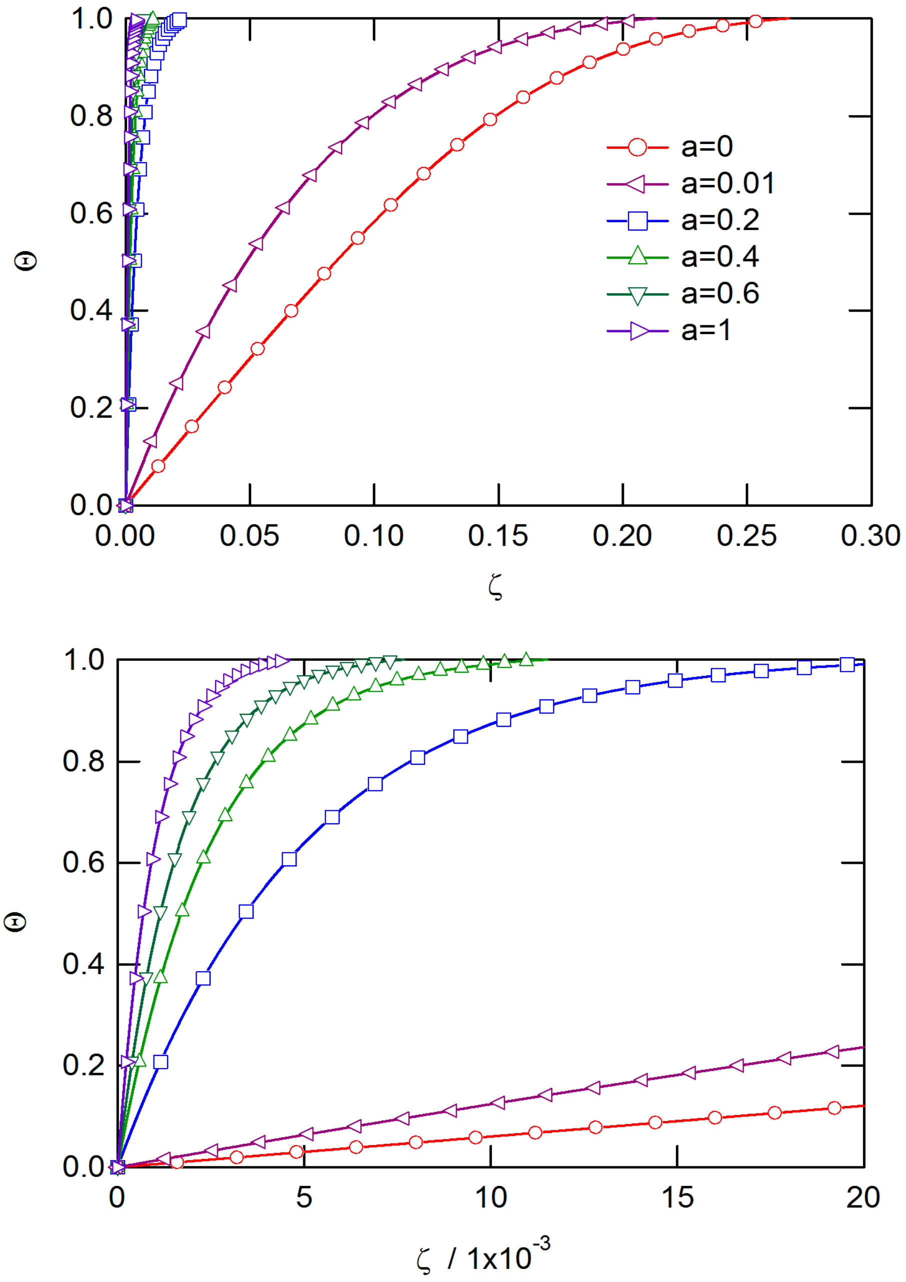

Figure 4.2 Dimensionless concentration profile ($\Theta = c/c_{\infty}$) at varying suction *a* from 0 to 1 at limiting current condition, in which case the PRDE surface concentration is zero. Bottom plot is the amplified part of the small ζ range of top figure to give a clearer view of high value *a*'s. Here ζ = 0 corresponds to PRDE-electrolyte interface. Symbols were sparsely labeled on the calculated line.

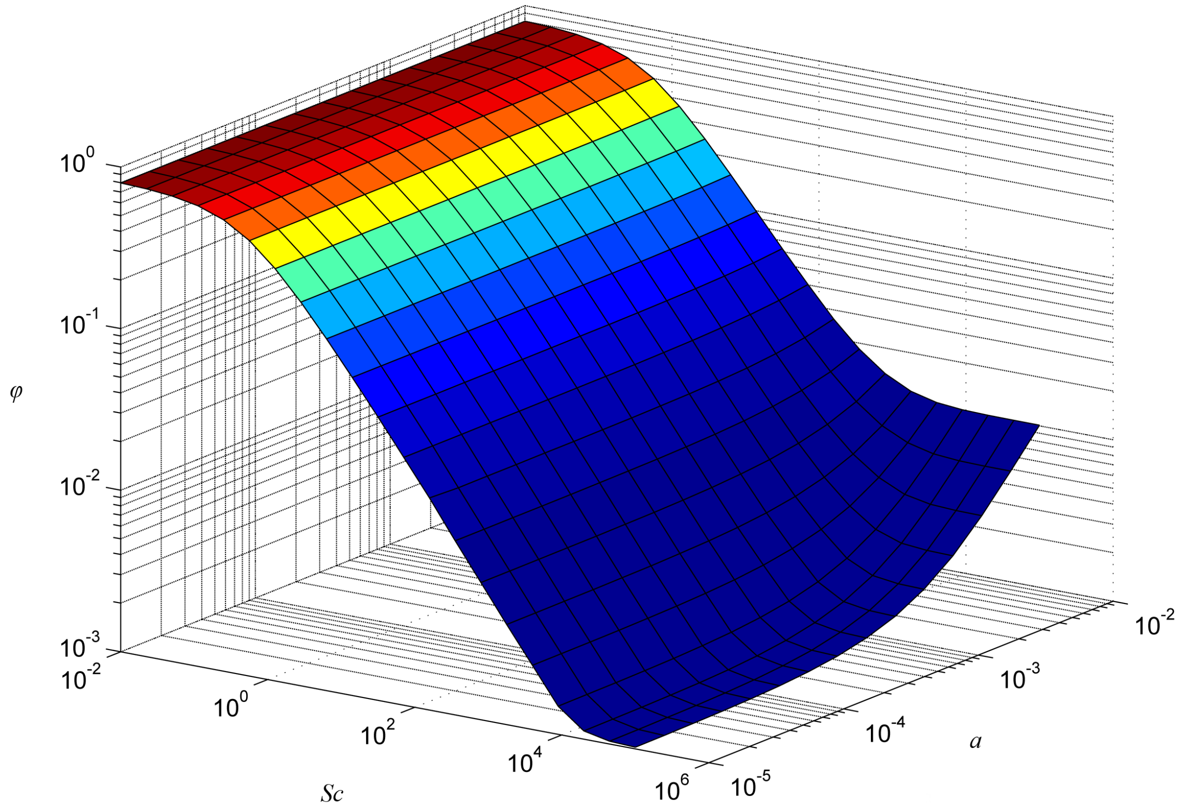

Figure 4.3 Dimensionless mass transfer ϕ at PRDE / electrolyte surface as a function of both suction, *a*, and Schmidt number, *Sc*. To shows a better overview, a range of *Sc* values larger than physically accessible were used to generate this plot. All axes scales are logarithmic.

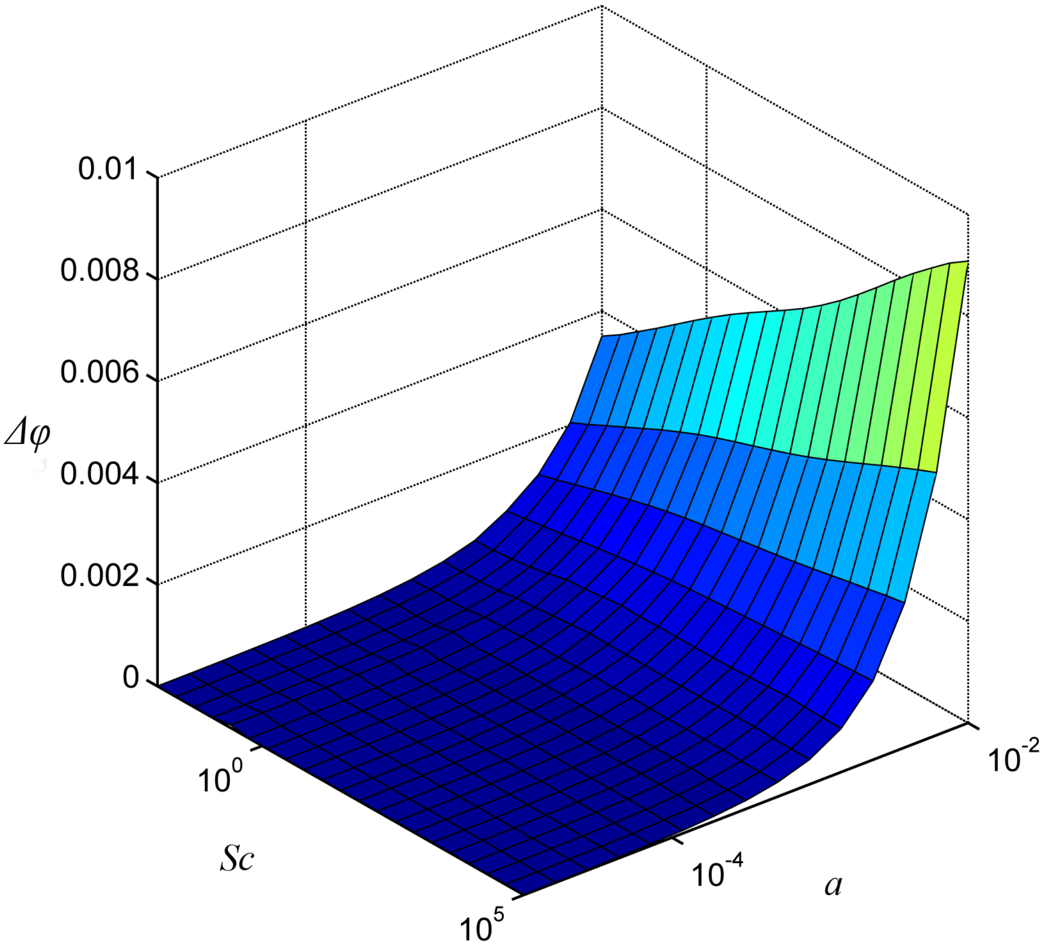

Figure 4.4 Mass transfer deviation Δϕ of *a* > 0 cases from *a* = 0 case. Sc and *a* are both logrithmatic.

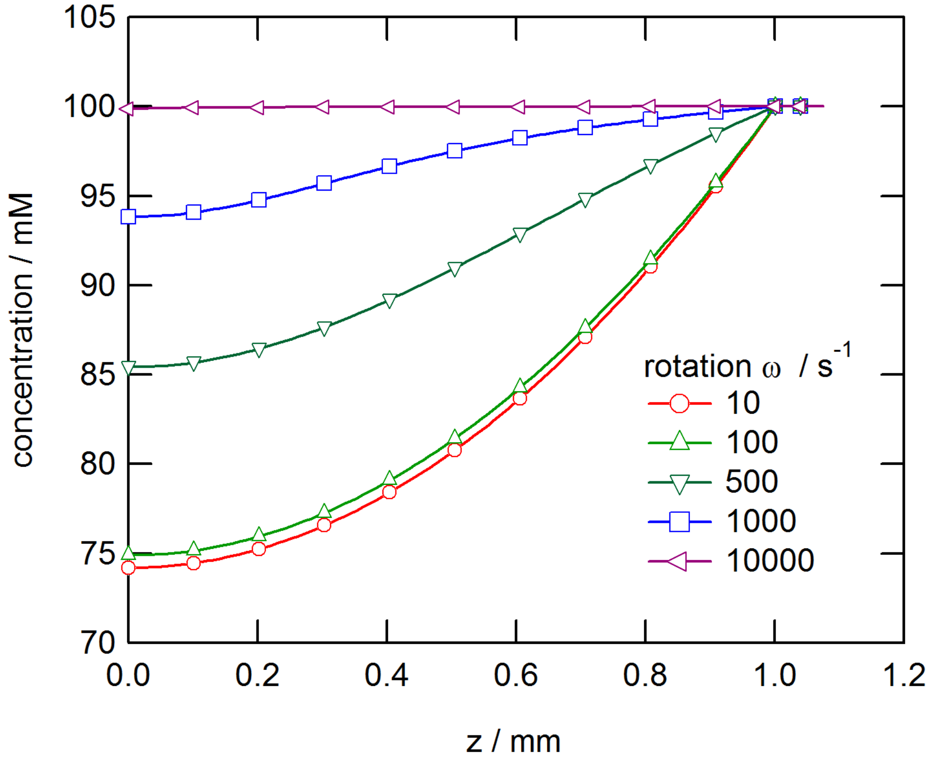

Figure 4.5 Concentration profile at varying rotation rate from 10 to 10^5 s^{-1}. Porous electrode thickness is 1 mm. All other parameters are the same as Table 4.2

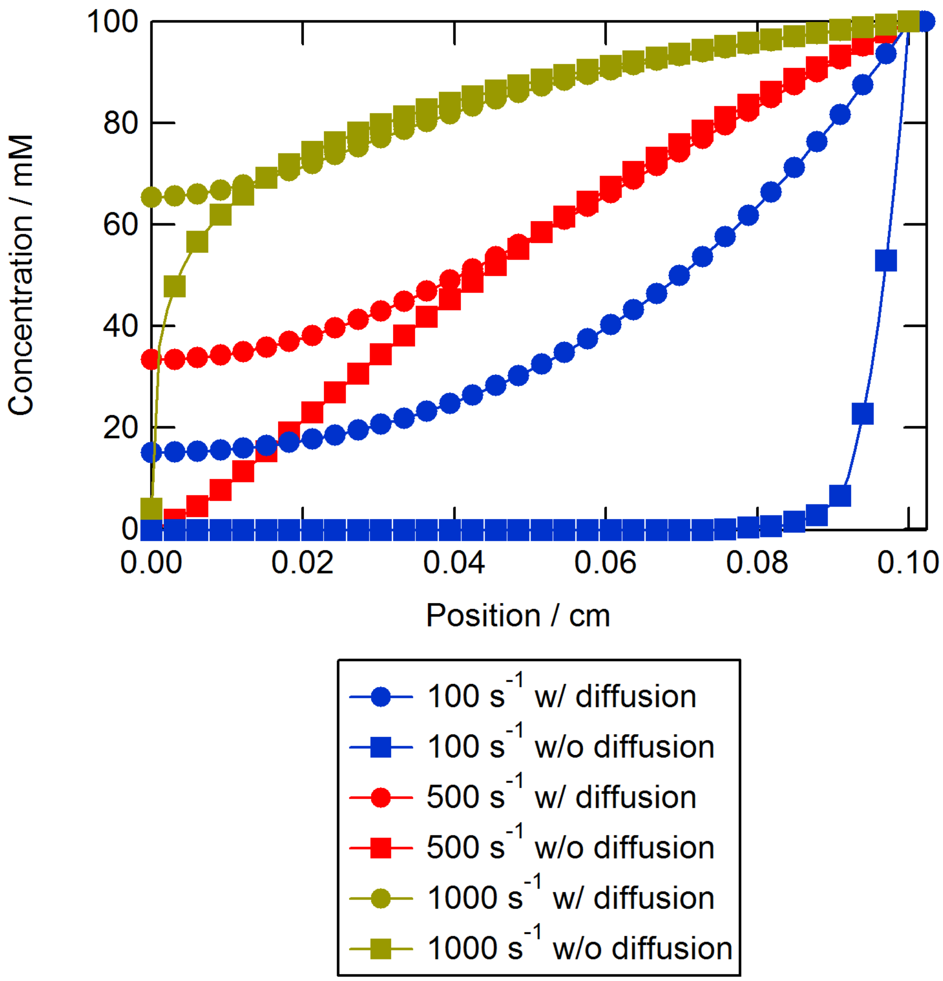

Figure 4.6 Concentration profile for diffusion included model and diffusion excluded model at varying rotations. All other parameters are the same as Table 4.2

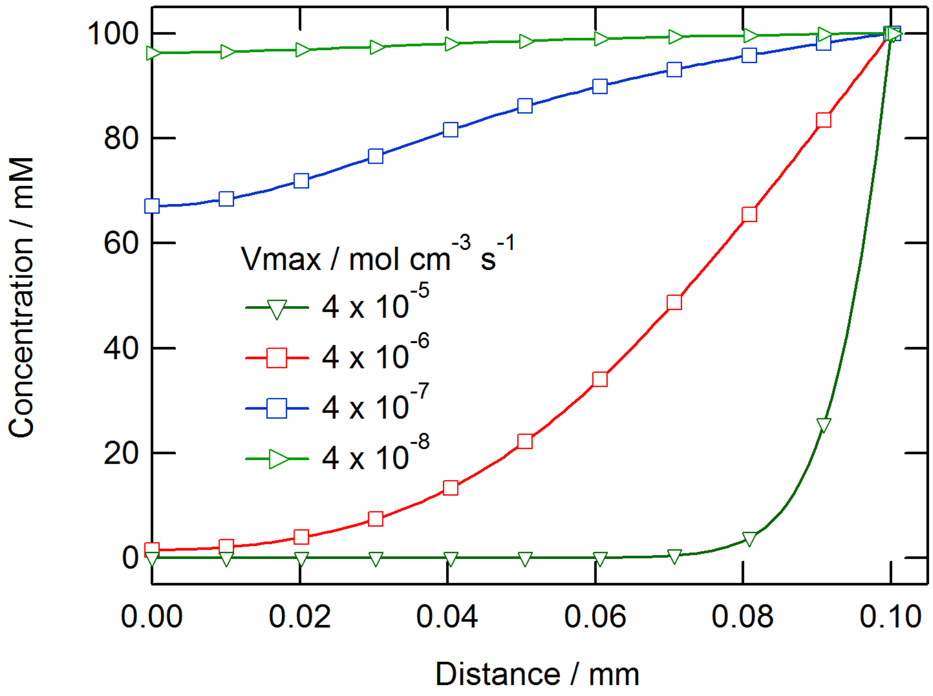

Figure 4.7 Concentration profile with varying Vmax. Other parameters were the same as Table 4.2 Parameter list.

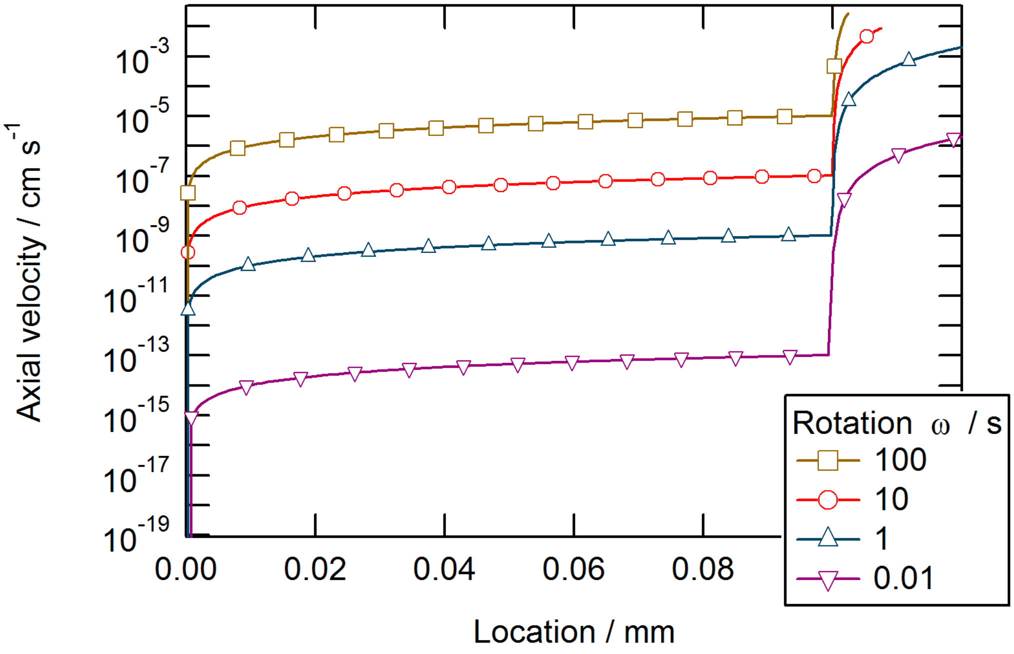

Figure 4.8 Velocity profile at varying rotations. PRDE top surface is at 0.01 mm. The velocity from 0 to 0.01 mm is thus within PRDE, beyond 0.01 mm is in electrolyte. The electrolyte velocity calculation is estimated only at locations below boundary layer thickness estimated from limiting current cases.

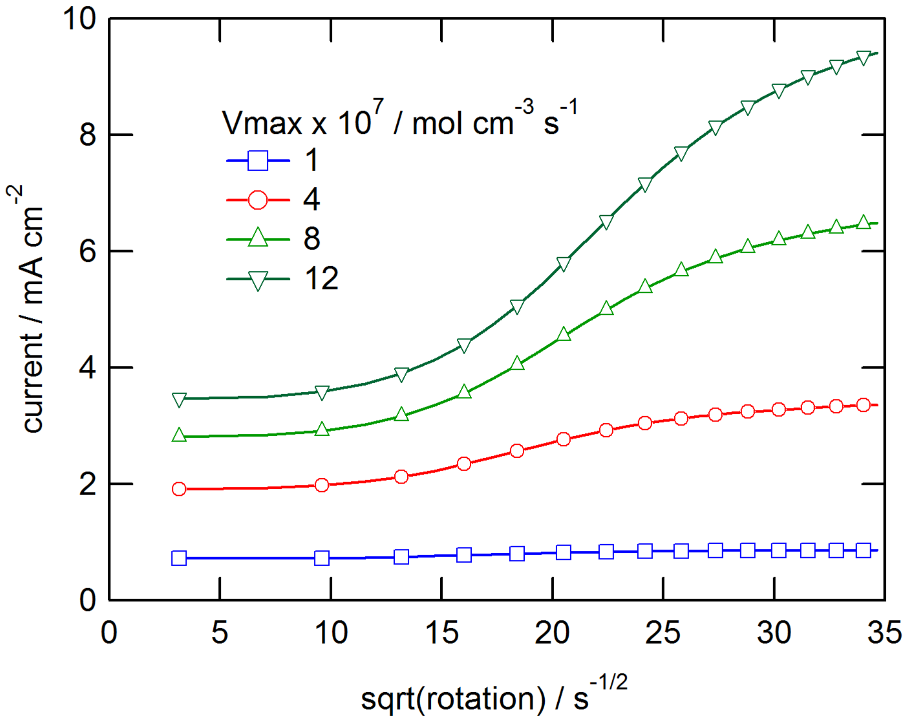

Figure 4.9 Rotation dependence of current density at varying $V_{\max}$. All other parameter values are the same as Table 4.2.

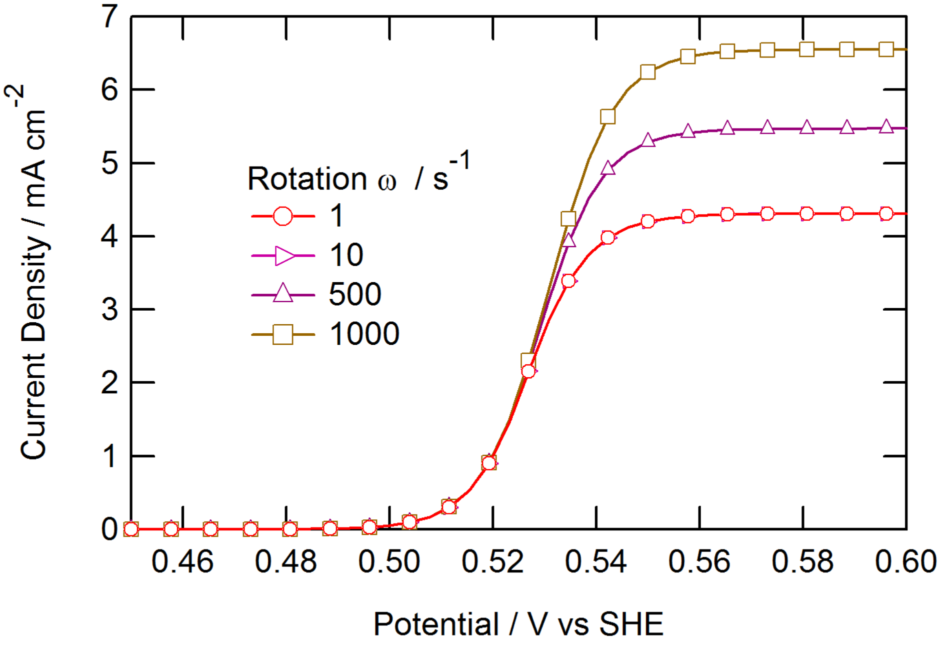

Figure 4.10 Potential dependence of current densities on varying rotation rates. All other parameter values are the same as Table 4.2.

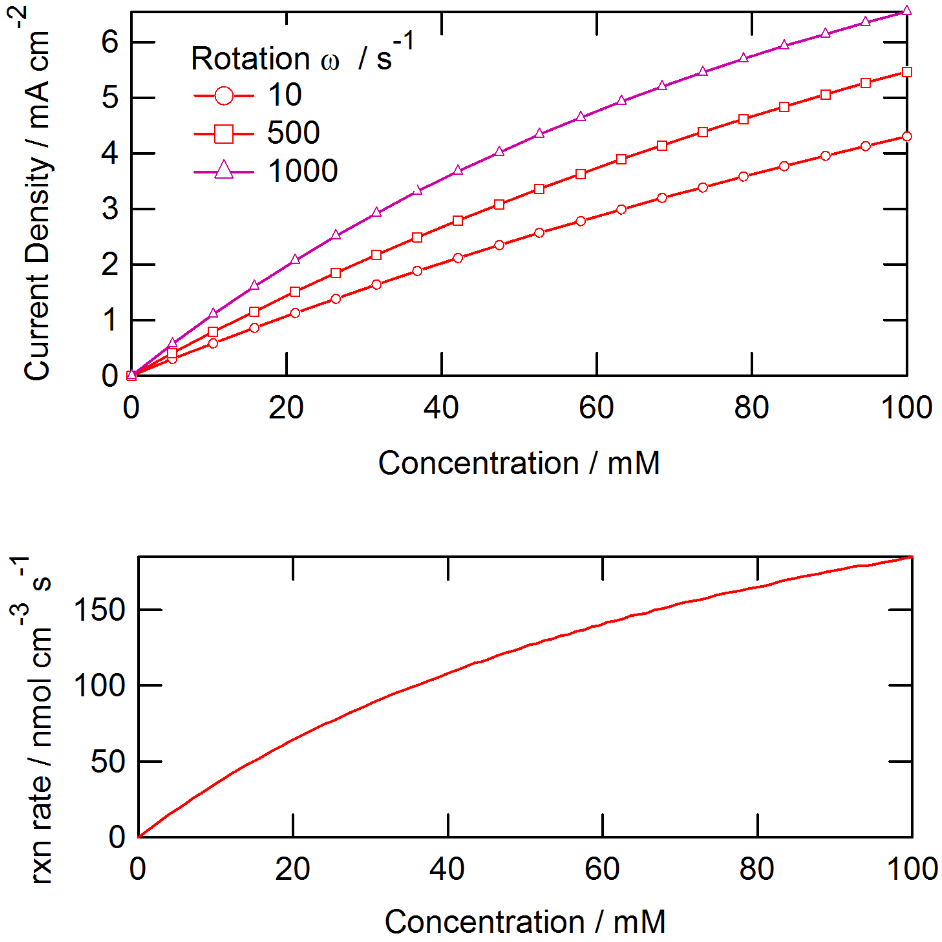

Figure 4.11 Substrate bulk concentration dependence of current densities (top) and the biocatalyst rate of reaction as a function of concentration. All other parameter values are the same as Table 4.2.

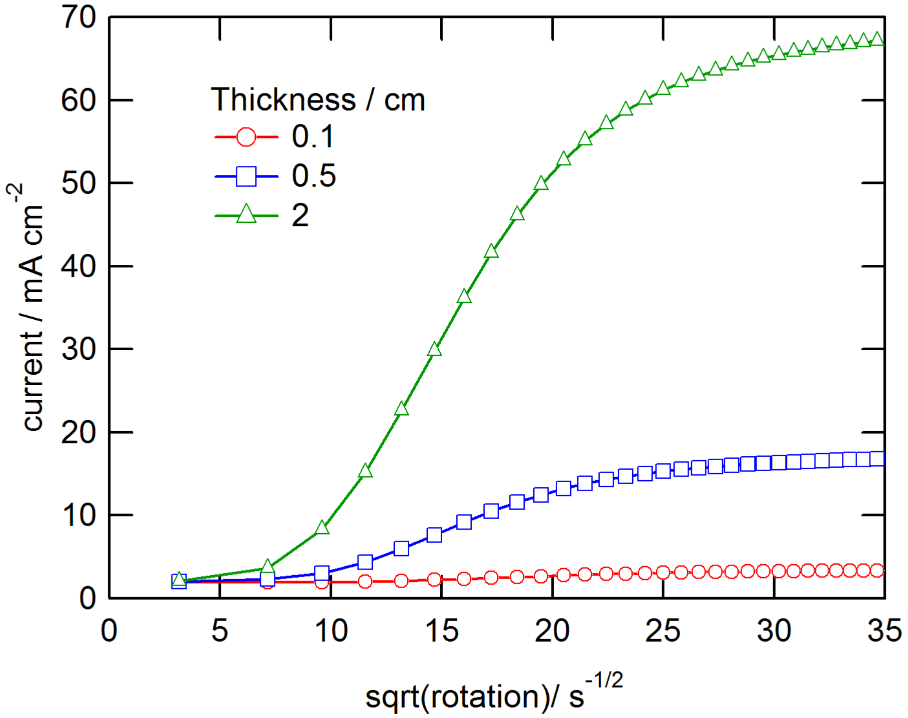

Figure 4.12 Effect of porous electrode thickness on the current density output. Electrode thicknesses were taken as 0.1, 0.5 and 2 cm.

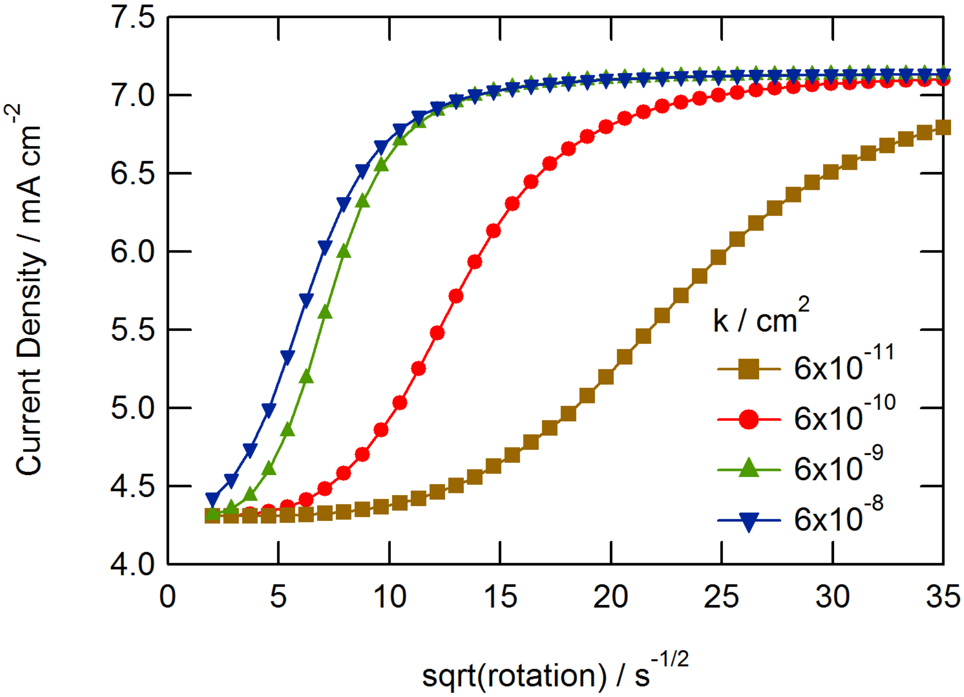

Figure 4.13 Permeability variation on rotation dependency of current density.

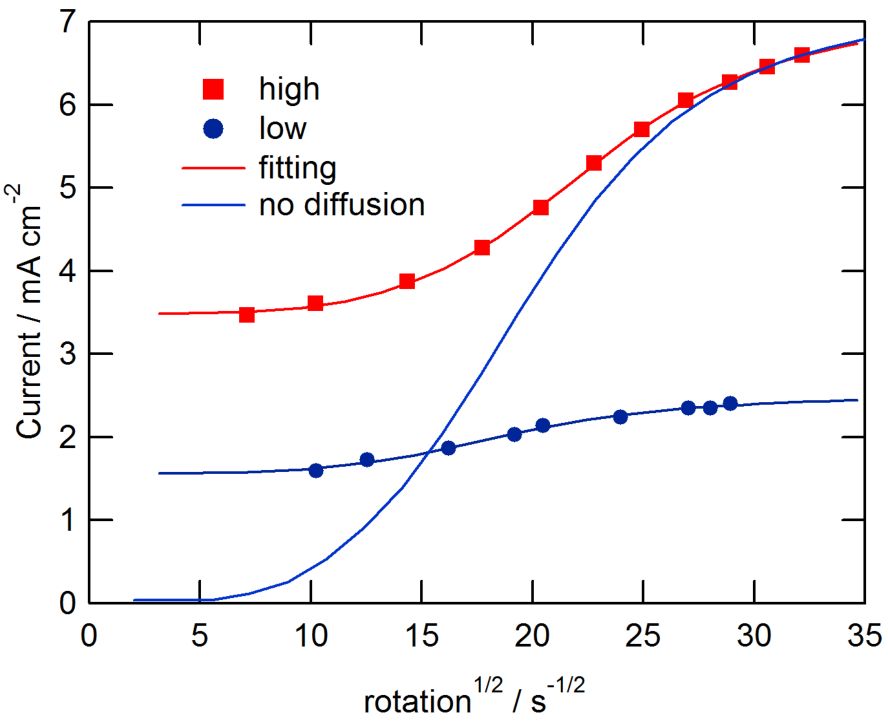

Figure 4.14 Fitting and experimental results at high and low loadings on PRDE. Also included is the calculation if no diffusion is considered in the high catalyst loading case.

REFERENCES

References

1. B.C. Steele and a Heinzel, "Materials for fuel-cell technologies." *Nature*, **414**(6861), 345-52 (2001).

2. V. Obreja, "On the performance of supercapacitors with electrodes based on carbon nanotubes and carbon activated material—A review" *Physica E: Low-dimensional Systems and Nanostructures*, **40**(7), 2596-2605 (2008).

3. V. Mehta and J.S. Cooper, "Review and analysis of PEM fuel cell design and manufacturing" *Journal of Power Sources*, **114**(1), 32-53 (2003).

4. H. Wen, H.M. Bambhania and S. Calabrese Barton, "Carbon nanotube-modified biocatalytic microelectrodes with multiscale porosity" *Journal of Applied Electrochemistry*, (2012).doi:10.1007/s10800-012-0381-9

5. N.P. Brandon and D.J. Brett, "Engineering porous materials for fuel cell applications." *Philosophical transactions. Series A, Mathematical, physical, and engineering sciences*, **364**(1838), 147-59 (2006).

6. H. Li, H. Wen and S. Calabrese Barton, "NADH Oxidation Catalyzed by Electropolymerized Azines on Carbon Nanotube Modified Electrodes" *Electroanalysis*, **24**(2), 398-406 (2012).

7. E. Yoo et al., "Large reversible Li storage of graphene nanosheet families for use in rechargeable lithium ion batteries." *Nano letters*, **8**(8), 2277-82 (2008).

8. C.K. Chan, X.F. Zhang and Y. Cui, "High capacity Li ion battery anodes using ge nanowires." *Nano letters*, **8**(1), 307-9 (2008).

9. Y. Wang and G. Cao, "Developments in Nanostructured Cathode Materials for High-Performance Lithium-Ion Batteries" *Advanced Materials*, **20**(12), 2251-2269 (2008).

10. Y. Yu, L. Gu, C. Zhu, P.A. van Aken and J. Maier, "Tin nanoparticles encapsulated in porous multichannel carbon microtubes: preparation by single-nozzle electrospinning and application as anode material for high-performance Li-based batteries." *Journal of the American Chemical Society*, **131**(44), 15984-5 (2009).

11. H. Li, Q. Wang, L. Shi, L. Chen and X. Huang, "Nanosized SnSb Alloy Pinning on Hard Non-Graphitic Carbon Spherules as Anode Materials for a Li Ion Battery" *Chemistry of Materials*, **14**(1), 103-108 (2002).

12. M. Wakihara, "Recent developments in lithium ion batteries" *Materials Science and Engineering: R: Reports*, **33**(4), 109-134 (2001).

13. M. Zukalová et al., "Organized mesoporous TiO_2 films exhibiting greatly enhanced performance in dye-sensitized solar cells." *Nano letters*, **5**(9), 1789-92 (2005).

14. K. Murakoshi, R. Kogure, Y. Wada and S. Yanagida, "Fabrication of solid-state dye-sensitized TiO_2 solar cells combined with polypyrrole" *Solar Energy Materials and Solar Cells*, **55**(1-2), 113-125 (1998).

15. M. Grätzel, "Dye-sensitized solar cells" *Journal of Photochemistry and Photobiology C: Photochemistry Reviews*, **4**(2), 145-153 (2003).

16. C.J. Barbé et al., "Nanocrystalline Titanium Oxide Electrodes for Photovoltaic Applications" *Journal of the American Ceramic Society*, **80**(12), 3157-3171 (2005).

17. S. Ito et al., "Fabrication of thin film dye sensitized solar cells with solar to electric power conversion efficiency over 10%" *Thin Solid Films*, **516**(14), 4613-4619 (2008).

18. F.-C. Yang and J.-T. Yu, "Development of a bioreactor system using an immobilized white rot fungus for decolorization" *Bioprocess Engineering*, **15**(6), 307-310 (1996).

19. K.J. Burg et al., "Comparative study of seeding methods for three-dimensional polymeric scaffolds." *Journal of biomedical materials research*, **51**(4), 642-9 (2000).

20. D.L. Nettles, S.H. Elder and J.A. Gilbert, "Potential use of chitosan as a cell scaffold material for cartilage tissue engineering." *Tissue engineering*, **8**(6), 1009-16 (2002).

21. V. Flexer, N. Brun, R. Backov and N. Mano, "Designing highly efficient enzyme-based carbonaceous foams electrodes for biofuel cells" *Energy & Environmental Science*, **3**(9), 1302 (2010).

22. V. Flexer, N. Brun, O. Courjean, R. Backov and N. Mano, "Porous Mediator-free Enzyme Carbonaceous Electrodes Obtained Through Integrative Chemistry for Biofuel Cells" *Small*, 1-10doi:10.1039/b000000x

23. J. Lu, L.T. Drzal, R.M. Worden and I. Lee, "Simple Fabrication of a Highly Sensitive Glucose Biosensor Using Enzymes Immobilized in Exfoliated Graphite Nanoplatelets Nafion Membrane" *Chemistry of Materials*, **19**(25), 6240-6246 (2007).

24. Q. Sheng, R. Liu, J. Zheng, W. Lin and Y. Li, "Direct electrochemistry of glucose oxidase immobilized on porous carbon nanofiber/room temperature ionic liquid/chitosan composite film and its biosensing application" *Journal of Solid State Electrochemistry*, **16**(2), 739-745 (2011).

25. S. Myler, S. Eaton and S.P.. Higson, "Poly(o-phenylenediamine) ultra-thin polymer-film composite membranes for enzyme electrodes" *Analytica Chimica Acta*, **357**(1-2), 55-61 (1997).

26. B. Nam and R.T. Bonnecaze, "Analytic Models of the Infinite Porous Rotating Disk Electrode" *Journal of The Electrochemical Society*, **154**(10), F191 (2007).

27. R.T. Bonnecaze, N. Mano, B. Nam and A. Heller, "On the Behavior of the Porous Rotating Disk Electrode" *Journal of The Electrochemical Society*, **154**(2), F44 (2007).

28. F. Lima, "Oxygen electrocatalysis on ultra-thin porous coating rotating ring/disk platinum and platinum-cobalt electrodes in alkaline media" *Electrochimica Acta*, **49**(24), 4091-4099 (2004).

29. J. Perez, "Application of the Flooded-Agglomerate Model to Study Oxygen Reduction on Thin Porous Coating Rotating Disk Electrode" *Journal of The Electrochemical Society*, **141**(2), 431 (1994).

30. E. Guilminot, A. Corcella, M. Chatenet and F. Maillard, "Comparing the thin-film rotating disk electrode and the ultramicroelectrode with cavity techniques to study carbon-supported platinum for proton exchange membrane fuel cell applications" *Journal of Electroanalytical Chemistry*, **599**(1), 111-120 (2007).

31. A.J. Appleby and M. Savy, "Kinetics of oxygen reduction reactions involving catalytic decomposition of hydrogen peroxide" *Journal of Electroanalytical Chemistry and Interfacial Electrochemistry*, **92**(1), 15-30 (1978).

32. B. Merzougui and S. Swathirajan, "Rotating Disk Electrode Investigations of Fuel Cell Catalyst Degradation Due to Potential Cycling in Acid Electrolyte" *Journal of The Electrochemical Society*, **153**(12), A2220 (2006).

33. F. LIMA, "Oxygen electrocatalysis on ultra-thin porous coating rotating ring/disk platinum and platinum?cobalt electrodes in alkaline media" *Electrochimica Acta*, **49**(24), 4091-4099 (2004).

34. J. Perez, E.R. Gonzalez and E.A. Ticianelli, "Oxygen electrocatalysis on thin porous coating rotating platinum electrodes" *Electrochimica Acta*, **44**(8-9), 1329-1339 (1998).

35. B. Nam and R.T. Bonnecaze, "Analytic Models of the Infinite Porous Rotating Disk Electrode" *Journal of The Electrochemical Society*, **154**(10), F191 (2007).

36. V. Flexer, N. Brun, R. Backov and N. Mano, "Designing highly efficient enzyme-based carbonaceous foams electrodes for biofuel cells" *Energy & Environmental Science*, **3**(9), 1302 (2010).

37. V. Flexer, N. Brun, O. Courjean, R. Backov and N. Mano, "Porous mediator-free enzyme carbonaceous electrodes obtained through Integrative Chemistry for biofuel cells" *Energy & Environmental Science*, **4**(6), 2097 (2011).

38. J.T. Stuart, "On the effects of uniform suction on the steady flow due to a rotating disk" *The Quarterly Journal of Mechanics and Applied Mathematics*, **7**(4), 446-457 (1954).

39. T. von Karman, "On laminar and turbulent friction" *Zeitschrift Für Angewandte Mathematik Und Mechanik*, **1**233-252 (1921).

40. D.D. Joseph, "Note on Steady Flow Induced By Rotation of a Naturally Permeable Disk" *The Quarterly Journal of Mechanics and Applied Mathematics*, **18**(3), 325-331 (1965).

41. S.H. Gehrke, J.P. Fisher, M. Palasis and M.E. Lund, "Factors determining hydrogel permeability." *Annals of the New York Academy of Sciences*, **831**(508), 179-207 (1997).

42. J.S. Newman and K.E. Thomas-Alyea, "*Electrochemical systems*" 647 (Wiley-IEEE: 2004).

43. M. Ikeguchi, K. Ishii, Y. Sekine, E. Kikuchi and M. Matsukata, "Improving oxygen permeability in SrFeCo0.5Ox asymmetric membranes by modifying support-layer porous structure" *Materials Letters*, **59**(11), 1356-1360 (2005).

44. S. Calabrese Barton, "Oxygen transport in composite mediated biocathodes" *Electrochimica Acta*, **50**(10), 2145-2153 (2005).

45. R.J. Millington and J.P. Quirk, "Permeability of porous solids" *Transactions of the Faraday Society*, **57**1200 (1961).

46. V. Nallathambi, J.-W. Lee, S.P. Kumaraguru, G. Wu and B.N. Popov, "Development of high performance carbon composite catalyst for oxygen reduction reaction in PEM Proton Exchange Membrane fuel cells" *Journal of Power Sources*, **183**(1), 34-42 (2008).

47. H. Li, H. Wen and S. Calabrese Barton, "NADH Oxidation Catalyzed by Electropolymerized Azines on Carbon Nanotube Modified Electrodes" *Electroanalysis*, n/a-n/a (2012).doi:10.1002/elan.201100573

48. B.Y.J.K. Gladden, "Diffusion in Supersaturated Solutions. II. Glucose Solutions" *Extrapolation*, **1**(1914), (1952).

Chapter 5 Modeling of Composite Porous Solid Oxide Fuel Cell Cathode

5.1 Abstract

Composite solid oxide fuel cell cathodes were proven to decrease cell polarization resistances. Such electrodes were composed of three interconnected phases: mixed ionic and electronic conductor (MIEC) phase, ionic conductor (IC) phase and gaseous phase. The impedance of an infiltrated solid oxide fuel cell composite cathode is modeled at varying MIEC loadings and temperatures. Diffusion, migration of oxygen vacancies and MIEC electronic conduction were considered. Simulation results were validated by comparison to experimental results conducted at symmetric cells. At high MIEC loadings, the experimental result displayed migration-limited behavior and was well described by a Gerisher impedance model. Ionic conductor conductivity and surface exchange reaction rate constants were fitted to experiments to yield temperature dependency of these parameters. However, under MIEC loadings less than 7.5 vol %, electronic conductivity and oxygen ion charge transfer via MIEC become rate limiting, necessitating a numerical model to fit the data. The fitted MIEC electronic conductivity was explained using percolation theory with Bethe lattice assumptions for finite sample size.

5.2 Introduction

At a solid oxide fuel cell (SOFC) cathode, oxygen is adsorbed to the cathode surface, dissociates into surface oxygen, diffuses along the surface, and finally reduces to oxygen anion through charge transfer and incorporation at catalytic sites.[1,2] The scheme of this process is shown in Figure 5.2. The overall reaction can be expressed as:

$$\frac{1}{2}O_2(g)+2e^-+V_o^{\infty}\rightarrow O_o^x \tag{1}$$

In a traditional SOFC cathode, the catalytic site is at the triple phase boundary (TPB) where gaseous oxygen, ion-conducting electrolyte and an electronic conductor coexist. However, the TPB is quite limited in porous media.[3]

Incorporation of a mixed ionic and electronic conductor (MIEC) material extends the active region of oxygen reduction to the bulk of the material.[4–6] However, MIEC doesn't have comparable ionic conductivity as that of ionic conductor (IC), which is the material for solid electrolyte.[7] For example, most commonly used ionic conductor, yittra-stabilized-zirconia (YSZ, IC) has ionic conductivity of 0.1 S/cm,[8] while the ionic conductivity of lanthanum strontium cobalt ferrite (LSCF, MIEC) is 1×10^{-7} S/cm.[9] It has previously been revealed by modeling that both surface oxygen diffusion and bulk vacancy transport can be rate limiting in porous MIEC cathodes.[10–12] For cathodes purely made of MIEC, oxygen vacancy transport largely limits the cathode current output. Porous composite MIEC/IC composite electrodes with MIEC nanoparticles coated on IC nanoscale scaffold address this issue by retaining IC as the major vacancy conduction channel.[13]

An example composite MIEC/IC electrode is the $Sm_{0.5}Sr_{0.5}CoO_{3-x}$-$Ce_{0.9}Gd_{0.1}O_{1.95}$ (SSC-GDC) composite electrode, where $Sm_{0.5}Sr_{0.5}CoO_{3-x}$ (SSC) is the MIEC and $Ce_{0.9}Gd_{0.1}O_{1.95}$ (GDC) is the IC. Such an electrode may be constructed by screen printing a GDC suspension onto a dense GCD electrolyte layer, followed by sintering to form a porous GDC electrode. An SSC precursor solution is then infiltrated into the scaffold, gelled and then fired to form SSC nanoparticles. This infiltration step may be repeated in order to control SSC loading from 2 % to 13.7 %. Finally, a current collector layer is printed on top of the composite porous electrode.[13]

The composite SOFC cathode has extremely low polarization resistance (R_p), which is considered the most important benchmark for SOFC cathodes.[4,13] At 600 °C under open circuit, a SSC-GDC cathode as described above displays a R_p value of 0.1 Ω cm^2 as compared to 1.8 Ω cm^2 for a conventional MIEC cathode.[5]

Various models considered composite cathodes.[9,14–17] Finite element analysis were used to study electrode models with more than one dimension, including electrode setup geometry, or potential and current distribution within particles.[4,9] Electrode geometries including thin film, random packing of particles, or macro-homogeneous overlapping phases were studied.[17,18]

Besides mass transport and electrochemical kinetics in electrodes, gas phase oscillation propagation in gas channels was also included in some whole cell models.[16] The "Simple Infiltrated Microstructural Polarization Loss Estimation" (SIMPLE) model is the starting point for this study. This model yields an analytical prediction of R_p with no adjustable parameters and it is capable of predicting experimental results within 30% error.[13,19] The SIMPLE model accounts for IC scaffold and MIEC nanoparticle geometry, the surface oxygen reaction resistance, and the oxygen vacancy conductance within IC electrolyte. However, the SIMPLE model does not account for limitations due to low electron conductivity, low surface exchange rates, or oxygen gas concentration polarization. The former limitations were observed at low MIEC loading, and the latter under non-equilibrium polarization conditions.

The effects mentioned above that is excluded by SMIPLE model were included in the present proposed model. The impedance responses of symmetric cells were studied by deriving from first principles including physicochemical processes such as gas diffusion and vacancy transport instead of equivalent circuit components. Such derivation is necessary because time-dependent processes like vacancy diffusion in MIEC phase is charge neutral, which cannot be accounted by any charge transfer circuit elements. On the other hand, equivalent circuit modeling is known to be non-unique to represent observed impedance, thus leading to possibly confusing interpretation of circuit element parameters. Thin film MIEC electronic and electrochemical properties were used as inputs to the model.[18] Electronic conductivity at low MIEC loading is modeled using percolation theory.[20]

This is a collaboration work with the research group of Dr. Jason Nicholas at Michigan State University. Dr. Nicholas is the author of the SIMPLE model,[4] and Lin Wang of Dr. Nicholas' group provided experimental data for model validation.

5.3 Mathematical Model

The proposed model is one-dimensional based on the macro-homogeneous porous electrode model.[21] Such models do not consider the exact position and geometry details of packing particles. Instead, continuous and average quantities were used to represent the electrode properties, and the various phases (in this case IC, MIEC, and gas phases) were considered as overlapped in space for calculation.[22] As shown in Figure 5.1, a differential volume element (DVE) of the porous electrode consists of IC, MIEC, and gas phases. The DVEs are big enough to contain all three phases and small enough to maintain continuous distributions of electrochemical potential and species concentrations. Within a DVE, electrons and oxygen gas are consumed following the reaction:

$$\frac{1}{2}V_o^{\infty} + 2e^- + O_2 \Leftrightarrow O_o \tag{2}$$

Although the mechanism of oxygen reduction is not yet fully understood,[23] this approach treats the whole reaction as a single consumption term, which greatly simplified the calculation.

Equivalent circuit model is the most widely used technique to solve for the impedance response of electrochemical systems.[24] This technique is insufficient in dealing with systems that are not clearly equivalent to any established circuit elements, such as Warburg element that's derived from restricted or semi-infinite diffusion:[25]

$$Z = \frac{1}{\sqrt{j\frac{\omega}{D_i}}} \tag{3}$$

The alternative way to solve for a complex system is to start from first principles like transport and thermodynamic equations, identify governing and boundary equations, and derive corresponding analytical or numerical results.

In the current work, electrochemical impedance spectroscopy were calculated by the following scheme:[24]

1. Set up the governing and boundary equations for SOFC cathode, based on transient mass balances in all the phases considered and electrochemical potentials.
2. Set $\frac{\partial}{\partial t} = 0$ to solve for steady state solutions. At open circuit, the steady state solution is trivial– uniform potential and concentration profiles yielding zero current.
3. Linearize all governing equations about the steady-state solution.
4. Transfer the linearized equations from time domain to frequency domain by setting $\frac{\partial}{\partial t} \to j\omega$, and solve for the transient term of all the time-dependent variables. This conversion technique is only valid for sinusoidal perturbations, and can greatly simplify solution process comparing to other techniques like Fourier transform.[25]
5. Solve the transient equations for a chosen value of potential perturbation, $\tilde{V}_0$.

6. Calculate impedance, which is defined as $Z(\omega) = \frac{\tilde{V}_0}{\tilde{I}(\omega)}$. Because the impedance, Z(ω), is normalized by $\tilde{V}_0$, and the governing equations are linearized, the impedance should therefore be independent of the value of $\tilde{V}_0$.

5.3.1 Governing equations for SOFC cathode

The impedance response can be solved for open circuit, where the steady state solution is uniform oxygen concentration, electric potential, and vacancy concentration throughout the electrode. This trivial condition enables easy calculation of impedance, including analytical solution under certain assumptions. The basis of the following governing equations is conservation of oxygen vacancies, electrons, and oxygen gas molecules.

Based on a vacancy mass balance, the governing equation for IC vacancy transport is

$$0 = \frac{\varepsilon_{ic}\sigma_{ic}}{\left(z_v F\right)^2}\frac{\partial^2 \mu_{v,ic}}{\partial y^2} - a_{ic}N \tag{4}$$

Electrochemical potential $\mu_{v,ic}$ for oxygen vacancy is defined as:

$$\mu_{v,ic} = z_v F\phi_v + RT\ln\left(c_v\right) + \mu_{v,ic,0} \tag{5}$$

the term *N* is the local charge transfer flux between IC and MIEC. The IC is assumed to be fast in oxygen vacancy transport, thus maintaining uniform concentration at all time. Thus the variation in vacancy potential in IC is only due to the electric potential variation.

Conservation of vacancies in the MIEC phase yields

$$\varepsilon_{miec}\frac{\partial C_v}{\partial t}=\frac{\varepsilon_{miec}D_v C_\infty}{RT}\frac{\partial^2\mu_{v,miec}}{\partial y^2}-n_v a_{miec}r+a_{ic}N \tag{6}$$

where r is reaction rate, given by Equation (11) Similarly, a charge balance within the MIEC governs electron conduction:

$$0=\frac{\sigma_e}{\left(z_e F\right)^2}\frac{\partial^2\mu}{\partial y^2}-n_e a_{miec}r \tag{7}$$

In the MIEC, electrons are assumed to have uniform concentration, so no accumulation term appears. For the gas phase, a material balance on oxygen yields

$$\varepsilon_{gas}C_0\frac{\partial x}{\partial t}=\varepsilon_{gas}D_g C_0\frac{\partial^2 x}{\partial y^2}-n_g a_{miec}r \tag{8}$$

where C_0 is bulk gas concentration, x is the partial pressure of oxygen, a_{miec} is the surface area of MIEC, D_g is gas diffusivity, and ε_{gas} is gas phase volume fraction.

Based on the governing equations above, the charge transfer flux between the IC and MIEC can be expressed as:

$$N=\frac{1}{\left(z_v F\right)^2}\left(\frac{1}{R_i}+C_i\frac{\partial}{\partial t}\right)\left(\mu_{v,ic}-\mu_{v,miec}\right) \tag{9}$$

where R_i is charge transfer resistance between MIEC and IC, C_i is capacitance. Equation (8) has already been linearized, thus R_i corresponds to the zero volts overpotential in Butler-Volmer equation:

$$i = i_0 \left(e^{\alpha_a \frac{nF}{RT}\eta} - e^{-\alpha_b \frac{nF}{RT}\eta} \right) \tag{10}$$

where i_0 is exchange current, and η is overpotential. Thus R_i can be expressed as

$$R_i = \frac{RT}{nFi_0} \tag{11}$$

Reaction rate can be expressed as:

$$\begin{aligned} r &= r_0 \left(e^{\alpha_f \Delta G} - e^{-\alpha_f \Delta G} \right) \\ \Delta G &= RT \left(\frac{1}{2} \ln \frac{x}{x_{eq}} + \ln \frac{C_v}{C_{v,eq}} \right) \end{aligned} \tag{12}$$

where x_{eq} and C_{eq} are values at equilibrium, which can be obtained by solving the steady state equations at open circuit. The electrochemical potential terms can be defined as

$$\begin{aligned} \mu_{v,ic} &= \mu_{v,ic,eq} + z_v F \left(\phi_v - \phi_{v,eq} \right) \\ \mu_{v,miec} &= \mu_{v,miec,eq} + RT \ln \left(\frac{C_v}{C_\infty} \right) - 2\mu_e \\ \mu_e &= \mu_{e,eq} + z_e F \left(U_e - U_{oc} \right) \end{aligned} \tag{13}$$

which is a combination of the chemical potential with the electrostatic potential. At open circuit, the trivial solution is:

$$\begin{aligned}
&\mu_e = \mu_{e,apply} \\
&C_v = C_{v,eq} \\
&x = x_{eq} \\
&\mu_{v,ic} = \mu_{v,ic,eq} \\
&\mu_{v,miec} = \mu_{v,miec,eq}
\end{aligned} \tag{14}$$

Based on this solution, we can linearize the governing equations and flux expressions and transfer them into frequency domain:

$$0 = \frac{\varepsilon_{ic}\sigma_{ic}}{\left(z_v F\right)^2}\frac{\partial^2 \widetilde{\mu_{v,ic}}}{\partial y^2} - a_{ic}\widetilde{N} \tag{15}$$

$$\varepsilon_{miec}\widetilde{C_v} \bullet j\omega = \frac{\varepsilon_{miec}D_v C_\infty}{RT}\frac{\partial^2 \widetilde{\mu_{v,miec}}}{\partial y^2} - n_v a_{miec}\tilde{r} + a_{ic}\widetilde{N} \tag{16}$$

$$0 = \frac{\sigma_e}{\left(z_e F\right)^2}\frac{\partial^2 \widetilde{\mu_e}}{\partial y^2} - n_e a_{miec}\tilde{r} \tag{17}$$

$$\varepsilon_{gas}C_0\tilde{x} \bullet j\omega = \varepsilon_{gas}D_g C_0\frac{\partial^2 \tilde{x}}{\partial y^2} - n_g a_{miec}\tilde{r} \tag{18}$$

$$\widetilde{N} = \frac{1}{\left(z_v F\right)^2}\left(\frac{1}{R_i} + C_i \bullet j\omega\right)\left(\widetilde{\mu_{v,ic}} - \widetilde{\mu_{v,miec}}\right) \tag{19}$$

$$\tilde{r} = r_0\left(\alpha_f + \alpha_b\right)\left(\frac{1}{2}\frac{\tilde{x}}{x_\infty} + \frac{\widetilde{C_v}}{C_\infty}\right) \tag{20}$$

$$\widetilde{\mu_{v,ic}} = z_v F \widetilde{\phi_v} \tag{21}$$

$$\widetilde{\mu_{v,miec}} = RT \frac{\widetilde{C_v}}{C_\infty} - 2\widetilde{\mu_e} \tag{22}$$

$$\widetilde{\mu_e} = z_e F \widetilde{U_e} \tag{23}$$

where *j* is complex number unit, all the tildes indicate all variables corresponds to transient term.

5.3.2 Boundary conditions

The boundary condition for steady state and transient frequency domain are very similar. See Figure 5.3 for a scheme of cathode processes. At electrode / electrolyte interface, in electrode:

$$\begin{aligned}
&\mu_{v,ic} = \mu_{v,ic,eq}, \widetilde{\mu_{v,ic}} = 0 \\
&\mu_{v,miec} = \mu_{v,ic}, \widetilde{\mu_{v,miec}} = \widetilde{\mu_{v,ic}} \\
&\nabla U_e = 0, \nabla \widetilde{U_e} = 0 \\
&\nabla x = 0, \nabla \tilde{x} = 0
\end{aligned} \tag{24}$$

At the electrode / current collector interface:

$$\begin{aligned}
&\nabla \mu_{v,ic} = 0, \nabla \widetilde{\mu_{v,ic}} = 0 \\
&\nabla \mu_{v,miec} = 0, \nabla \widetilde{\mu_{v,miec}} = 0 \\
&U_e = U_{apply}, \widetilde{U_e} = \widetilde{U_{apply}} \\
&x = x_\infty, \tilde{x} = 0
\end{aligned} \tag{25}$$

where $U_{\text{apply}} = 0$ V for open circuit.

The calculation of impedance can be conducted with:

$$\begin{aligned}
\tilde{i} &= -\frac{\sigma_{ic}}{\left(z_v F\right)^2}\frac{\partial \widetilde{\mu_{v,ic}}}{\partial y} - \frac{\varepsilon_{miec} D_v C_\infty}{RT}\frac{\partial \widetilde{\mu_{v,miec}}}{\partial y}\Big|_{y=0} \\
Z &= \frac{\widetilde{U_{apply}}}{\tilde{i}}
\end{aligned} \tag{26}$$

5.3.3 *Percolation theory for low MIEC loadings*

Figure 5.11 showed the scheme for percolation model. Top of the MIEC nanoparticles were in contact with current collector. It is assumed that the MIEC nanoparticles were randomly distributed within the pore column and only those particles that's connected to the current collector is active.

For the current system under study, the percentage of active MIEC particles that's electronically accessible to current collector and their effective conductivity are of interest.

The general formula to calculate accessible MIEC particles are:[26]

$$\varepsilon_a^T = \varepsilon_a\left(\varepsilon,\xi\right) + \sum_{n=1}^{\infty} s_n\left(n,\varepsilon,\xi\right) p_v\left(nv^*\right) \tag{27}$$

where ε_a^T is the total accessible particle fraction, $\varepsilon_a(\varepsilon,\xi)$ is the particle that belong to infinite particle cluster, $s_n\left(n,\varepsilon,\xi\right)$ is the volume fraction of cluster with size n, and $p_v\left(nv^*\right)$ is the probability of size n cluster coincide with current collector. For an ideal percolation system, sample has infinite size, and particles form "clusters". The system under study is not ideal, in the sense that it is finite in sample size, thus even if a particle does not belong to an infinite cluster; it could still be accessible to the current collector. That's the reason for the second term in equation (26).

To calculate effective conductivity, the following general equation can be used:

$$\sigma_{eff} = \sigma_0 \bullet h(\varepsilon, \xi, x) \tag{28}$$

where σ_{eff} is the effective conductivity, σ_0 is the MIEC bulk conductivity, $h(\varepsilon, \xi, x)$ is the function that accounts for the porosity.

To carry out the aforementioned calculation, Bethe lattice approximation can be utilized.[27–29] It is one of the few percolation models with analytical solutions. Most of the physically realistic lattices can be approximated by Bethe lattice by choosing an effective particle coordination number. The effective coordination number can be chosen based on the following equation:

$$\frac{1}{(\xi - 1)} = p_c \tag{29}$$

where ξ is the effective coordination number, and p_c is the observed percolation threshold. Thus, for example, for $p_c = 0.33$, $\xi = 4$. Finite cluster size distribution for Bethe lattice can be derived to be:

$$s_n(n, \varepsilon, \xi) = \frac{2(\xi - 1)\big((n+1)(\xi - 1) - 1\big)}{(n-1)!\big((n+1)(\xi - 1) - n + 1\big)!} \varepsilon^n (1 - \varepsilon)^{(\xi - 2)n + \xi} \tag{30}$$

It needs to be noted that:

$$\lim_{n\to\infty}\left(s_n\left(n,\varepsilon,\xi\right)\right)=\varepsilon_a \tag{31}$$

The probability of cluster on the surface can be calculated based on surface to volume ratio of our system. The porosity effect on conductivity function h can also be calculated based on Bathe lattice approximation.

$$h\left(\varepsilon,\xi,x\right)=-\frac{\xi-1}{\xi-2}\frac{C'}{\sigma_0} \tag{32}$$

where C' is a integration specific to assumed lattice.[30,31]

5.4 Results and discussion

5.4.1 Impedance analytical solution

Although the comprehensive impedance model is consisted of four dependent variables and it is impossible to solve it analytically. However, it is possible to obtain an analytical solution with the following assumptions:

1. No gas phase transport limitation;
2. Uniform electronic state (high electronic conductivity of MIEC)
3. No charge transfer resistance between MIEC and IC;
4. Large electrode thickness.

As shown later, these assumptions are generally valid for the SSC-GDC symmetric SOFC. Adler have proposed similar solution for MIEC only cathode. In the current work, we will show that composite MIEC/IC cathode follows the same trend.

With the assumption above, equation group (9) can be simplified to:

$$\begin{aligned}
&0 = \frac{\varepsilon_{ic}\sigma_{ic}}{\left(z_v F\right)^2}\frac{\partial^2 \widetilde{\mu_{v,ic}}}{\partial y^2} - a_{ic}\widetilde{N} \\
&\varepsilon_{miec}\widetilde{C_v}j\omega = \frac{\varepsilon_{miec}D_v C_\infty}{RT}\frac{\partial^2 \widetilde{\mu_{v,miec}}}{\partial y^2} - n_v a_{miec}\tilde{r} + a_{ic}\widetilde{N} \\
&\widetilde{\mu_{v,ic}} = \widetilde{\mu_{v,miec}} \\
&\tilde{r} = r_0\left(\alpha_f + \alpha_b\right)\frac{\widetilde{C_v}}{C_\infty} \\
&\widetilde{\mu_{v,ic}} = z_v F\widetilde{\phi_v} \\
&\widetilde{\mu_{v,miec}} = RT\frac{\widetilde{C_v}}{C_\infty} - 2\widetilde{\mu_e} \\
&\widetilde{\mu_e} = z_e F\widetilde{U_e}
\end{aligned} \tag{33}$$

The analytical solution to this equation is:

$$Z = \frac{zz\sqrt{1+\dfrac{cn}{\mu 1n}}}{2\left(z\mu_1 + z\mu_2\right)}\frac{1}{\sqrt{cr + ct\left(j\omega\right)^{\beta}}} \tag{34}$$

where

$$\begin{aligned}
&zz = \frac{LRT}{z_e z_v F^2}, cn = \frac{L^2}{D_v}\frac{1}{\varepsilon_{miec}C_\infty}\frac{a_{ic}RT}{\left(z_v F\right)^2}, \mu 1n = \frac{a_{ic}L^2}{\varepsilon_{ic}\sigma_{ic}} \\
&z\mu_1 = \frac{\varepsilon_{ic}\sigma_{ic}RT}{\left(z_v F\right)^2}, z\mu_2 = \varepsilon_{miec}D_v C_\infty \\
&ct = \frac{L}{D_v}, cr = \frac{L^2}{D_v}\frac{1}{\varepsilon_{miec}C_\infty}n_v a_{miec}r_0
\end{aligned} \tag{35}$$

Definition in equation (34) is also included in Table 5.2. Here β is time constant dispersion factor, indicating the dispersion of vacancy diffusivity and conductivity in MIEC and IC. Equation (33) is the same mathematically as Gerisher impedance element. $z\mu_1$ and $z\mu_2$ corresponds to the contribution of vacancy transport from IC and MIEC, respectively.

The fitting result is shown in Figure 5.4. The experimental data were obtained with symmetric cell made of SSC-GDC composite at 13.7 vol % MIEC infiltration volume fraction. Experimental data were obtained from 400 to 700 °C. The fittings were all obtained with 3 parameters: IC oxygen conductivity, surface exchange reaction constant, and time constant dispersion factor β. At higher temperatures of 650 (not shown here) and 700 °C, there is a low frequency bump, which should correspond to gas phase diffusion.

The summary of the fitting is shown in Figure 5.5. With increasing temperature, both IC conductivity and surface exchange reaction rate increase. According to Arrhenius equation, the activation energy is $(6.45 \pm 0.62) \times 10^4$ J mol^{-1} for reaction, and $(5.26 \pm 0.34) \times 10^4$ J mol^{-1} for IC vacancy conduction.

5.4.2 Low MIEC loading model

At low loading of MIEC loadings, the percolation of MIEC may not be fully connected to form a network. In this case, the electronic conductivity and surface reaction constant were assumed to be affected significantly, as shown in the largely increased polarization resistance.

To model such case, we introduce variable μe as one additional dependent variable to solve on top of equation 32:

$$\frac{\partial^2 c}{\partial \xi^2} = K \bullet c \tag{36}$$

$$\frac{\partial^2 \mu_e}{\partial \xi^2} = \mu er \bullet c \tag{37}$$

where

$$K = \frac{ct(j\omega)^{\beta} + \left(1 + \dfrac{cn}{\mu 1n}\right)\mu er + cr}{1 + \dfrac{cn}{\mu 1n}} \tag{38}$$

with boundary conditions:

$$c - 2\mu_e = 0\Big|_{\xi=0} \tag{39}$$

$$\nabla \mu_e = 0\Big|_{\xi=0} \tag{40}$$

$$\nabla\left(c - 2\mu_e\right) = 0\Big|_{\xi=1} \tag{41}$$

$$\mu_e = \mu_{e,applied} \tag{42}$$

Although it is hard to give an explicit analytical solution, it is possible to simplify the problem to the following matrix (see Appendix for details and the definition for A_i is in equation (45) and (46)):

$$\begin{bmatrix} 1-\frac{2\mu er}{K} & 1-\frac{2\mu er}{K} & 0 & -2 \\ \frac{\mu er}{-\sqrt{K}} & \frac{\mu er}{\sqrt{K}} & 1 & 0 \\ \left(-\sqrt{K}+\frac{2\mu er}{\sqrt{K}}\right)e^{-\sqrt{K}} & \left(\sqrt{K}-\frac{2\mu er}{\sqrt{K}}\right)e^{\sqrt{K}} & -2 & 0 \\ \frac{\mu er}{K}e^{-\sqrt{K}} & \frac{\mu er}{K}e^{\sqrt{K}} & 1 & 1 \end{bmatrix} \bullet \begin{bmatrix} A_1 \\ A_2 \\ A_3 \\ A_4 \end{bmatrix} = \begin{bmatrix} 0 \\ 0 \\ 0 \\ \mu_{e0} \end{bmatrix} \tag{43}$$

where μ_{e0} is the potential modulation. And the impedance is:

$$Z = \frac{zz \bullet \mu_{e0}}{\left(z\mu_1 + z\mu_2\right)} \frac{1}{\left(\sqrt{K} - \frac{2\mu er}{\sqrt{K}}\right)\left(A_2 - A_1\right) - 2A_3} \tag{44}$$

It can be proved that when $\mu er \to 0$ (corresponds to large electronic conductivity), and $K \to +\infty$ (corresponds to large thickness), the matrix equation (42) can be significantly simplified and Gerisher type of impedance solution in equation (33) can be restored.

Fitting results comparing to experimental data is shown in Figure 5.6. SSC infiltration loading from 2.0 % to 15.5 vol % for SSC-GDC composite electrodes at 550 °C were used as example here. Besides the previously mentioned low MIEC loading model, a constant phase element (CPE) and resistor equivalent circuit model was used to account for the high frequency semi-circle in Nyquist plot in Figure 5.6, with its impedance as:

$$Z = \frac{R_h}{R_h Q_h \left(j\omega\right)^{\alpha} + 1} \tag{45}$$

where R_h is high frequency resistance and Q_h is high frequency CPE constant. Although not obvious in Nyquist plot, Bode plot with frequency vs. –Im(Z) clearly indicated the distinguishable time constants of vacancy transport within cathode and the added CPE process. The correlated characteristic frequencies were summarized in Figure 5.8. High loading at 13.7 and 15.5 vol % were not included since the peak is not as distinguishable, thus the inclusion of CPE leads to large fitting errors. The CPEs arise due to the IC / MIEC interfacial vacancy charge transfer. At large MIEC loadings, the abundance of interfacial surface area between IC/MIEC in cathode resulted in small charge transfer resistance. Low MIEC loadings, especially those under percolation threshold, would significantly lower the active charge transfer area, thus result in much larger R_h.

The low loading model with CPE gave reasonably good fitting results. Based on the baseline parameter values shown in Table 5.1, the rate constant r_0 and MIEC conductivity were chosen as the fitting parameters. They were chosen because they were supposedly affected the most by MIEC loading level, and they gave the distinguishable curve change in both Nyquist and Bode plots, as shown in Figure 5.9 and Figure 5.10. Generally speaking, a decreasing rate constant leads to larger total resistance, but minimal change at high frequencies. The peak frequency would also shift to orders of magnitude smaller dramatically. The decrease of MIEC conductivity also increase total resistance, but the Nyquist plot is affected throughout frequency spectrum, and the shift in peak frequency is much smaller comparing to rate constant changes.

The summary of the fitted parameters was shown in Figure 5.7. MIEC conductivity showed dramatic increase at higher MIEC loadings, which shall be addressed by percolation theory below. Rate constant doesn't increase in percolation theory pattern since it is a surface property, which is proportional to MIEC loadings. The fitting of CPE leads to decreasing resistances, indicating enhanced charge transfer with higher loading with MIECs.

5.4.3 Percolation theory prediction of MIEC conductivity

Bethe lattice approximation is used to explain the observed conductance trend with infiltration volume fraction. Based on the fitted MIEC conductance value from Figure 5.7, the volume fraction of particle in void space can be calculated by dividing MIEC fraction with void fraction of 32%. Percolation threshold has to be above 23.4% (= 7.5 vol % of MIEC total volume fraction) since the conductance at this loading is 6 orders of magnitude lower than bulk MIEC conductivity. Thus a reasonable equivalent Bethe lattice coordination number was chosen to be 5. As shown later, it is indeed the case. With this input, accessible particle fraction and effective conductivity were calculated and shown in Figure 5.12.

The fitted conductivity and percolation predication matched reasonably well. Beyond percolation threshold, conductivity increases gradually, while accessible particles increase sharply. This trend can be visualized in such a way: right before the percolation threshold, particle clusters with finite size were formed. At the threshold, those clusters were connected with very thin bottlenecks to form an infinite cluster. These bottlenecks were the rate-limiting step for electronic conduction, but all the particles previously in finite clusters were suddenly accessible from the boundaries. Below percolation threshold, infinite cluster has zero conductivity and accessibility. For a finite sample, it is not the case. Figure 5.12 shows the finite sample case in log scale. Accessible particle fraction overlaps with that of infinite sample beyond percolation threshold, indicating most of the accessibility is due to infinite cluster when it’s available.

The conductivity at very low loading at 9 vol% showed much larger value than percolation predictions. It is due to the MIEC / current collector triple phase boundary (TPB) that is active even if there is no MIEC infiltration at all. This TPB can serve as a reaction route that's in parallel to the cathode reactions. At medium to high MIEC loading values, this route is almost inactive. When loading is very low, this TPB leads to higher background reaction and thus leads to higher conductivities.

5.5 Conclusions

SSC-GDC composite cathode impedance performances were modeled at varying loadings and temperatures. The diffusion, migration of oxygen vacancies and MIEC electronic conduction were considered, which enables us to de-convolute the charge neutral processes that are contributing to impedance responses. At high MIEC loadings above percolation threshold, composite cathode followed semi-infinite transport and showed Gerisher type of responses. Ionic conductor conductivity and surface exchange reaction rate constant were fitted to yield the temperature dependences. At low loadings from 2.0 ~ 15.5 vol % MIEC loadings at 550 ˚C, due to the limited contact between MIEC nanoparticles, the electronic conductivity within MIEC is thus limited, and led to much larger polarization resistances. Besides that, semi-circles at high frequencies due to oxygen ion charge transfer were observed. Taking those two effects into account, Nyquist and Bode plots were fitted with good match. The fitted MIEC electronic conductivity was explained with percolation theory with analytical solution by simplifying with Beth lattice assumptions. The fitted conductivity showed good fit except at very low MIEC volume fractions, where the fitted value is orders of magnitude larger than the predictions by percolation theory. This is probably due to the triple phase boundary (TPB) at the cathode / current collector interface, which provide a reaction path in parallel with MIEC active sites.

5.6 Tables

Table 5.1 List of parameters

Symbol	Description	Value	Reference
a_{miec}	MIEC active surface area	2×10^{4} cm^{2}/cm^{3}	Nicholas2009
a_{ic}	IC / MIEC interfacial surface area	To be fitted	
$C_{g,\infty}$	Gas bulk concentration	2.4 mM	
$C_{v,\infty}$	Vacancy bulk concentration	10 mM	Svensson1997
C_i	MEIC/IC charge transfer capacitance	4×10^{-5} F/cm^{2}	Baumann2007
D_v	Vacancy diffusivity	To be fitted	Svensson1997
D_g	Gas bulk diffusivity	0.83 cm^{2}/s	
L	Cathode thickness	10 µm	Nichoals2009
r_0	Reaction constant	To be fitted	
Q_h	High frequency CPE constant at low loading	To be fitted	
R_h	High frequency resistance in low loading model	To be fitted	
R_i	MEIC/IC charge transfer resistance	1×10^{-5} Ω cm^{2}	Baumann2007
x_∞	Bulk oxygen fraction	0.2	
ε_{miec}	MIEC volume fraction	0.14	Nicholas2009
ε_{ic}	IC volume fraction	68%	Nicholas2009
σ_{miec}	MIEC electric conductivity	1000 S/cm	Wang2003

Table 5.2 List of non-dimensional variables and parameters

Symbol	Definition
$c = \widetilde{C_v} / C_\infty$	Vacancy concentration
$r = \tilde{r} / r_0$	Reaction rate
$n = \widetilde{N}\left(z_v F\right)^2 R_i / RT$	Charge transfer flux
$x = \tilde{x} / x_\infty$	Oxygen volume fraction
$\xi = y / L$	Length
$\mu_1 = \widetilde{\mu_{v,ic}} / RT$	IC vacancy potential
$\mu_2 = \widetilde{\mu_{v,miec}} / RT$	MIEC vacancy potential
$\mu_e = \widetilde{\mu_e} / RT$	Electronic potential
$ct = L / D_v$	MIEC time constant
$cr = \dfrac{L^2}{D_v} \dfrac{1}{\varepsilon_{miec} C_\infty} n_v a_{miec} r_0$	MIEC reaction
$cn = \dfrac{L^2}{D_v} \dfrac{1}{\varepsilon_{miec} C_\infty} \dfrac{a_{ic} RT}{\left(z_v F\right)^2}$	Charge transfer flux coefficient
$\mu 1n = a_{ic} L^2 / \varepsilon_{ic} \sigma_{ic}$	IC vacancy conductivity
$\mu er = \left(z_e F L\right)^2 n_e a_{miec} r_0 / \sigma_e RT$	Electron reaction term
$zz = \dfrac{LRT}{z_e z_v F^2}$	Impedance calculation
$z\mu_1 = \dfrac{\varepsilon_{ic} \sigma_{ic} RT}{\left(z_v F\right)^2}$	Impedance IC contribution
$z\mu_2 = \varepsilon_{miec} D_v C_\infty$	Impedance MIEC contribution

5.7 Figures

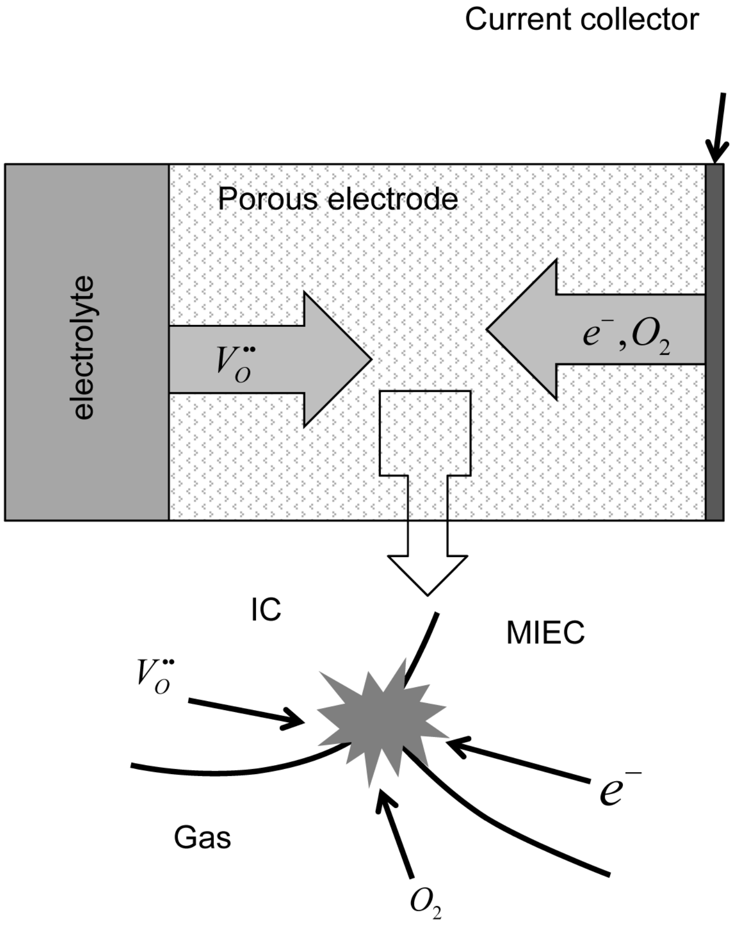

Figure 5.1 Schematic of SOFC modeling scheme. The bottom inset shows the reaction happening at a differential volume element in the macro-homogeneous model.

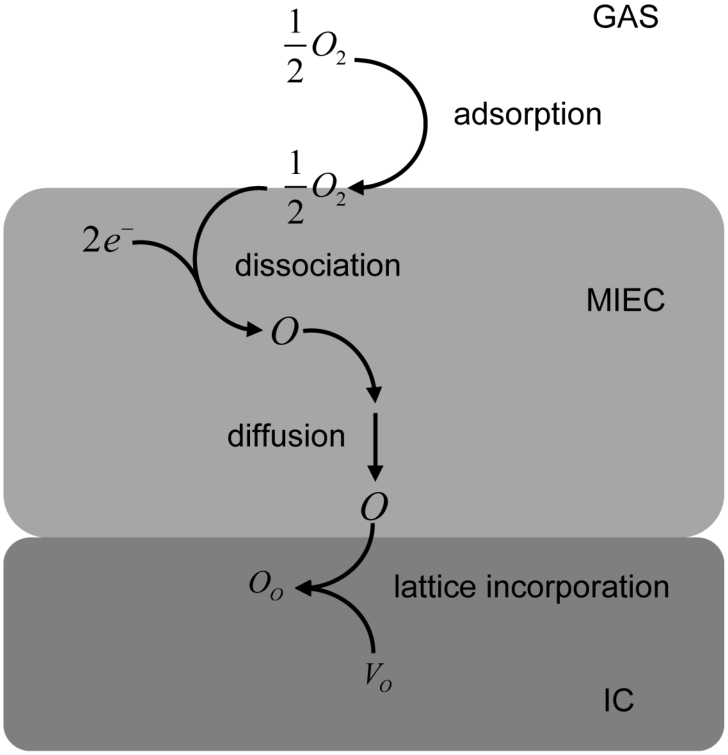

Figure 5.2 The process of oxygen reduction in SOFC cathode MIEC catalyst layer. Three phases are shown here: gas phase, mixed ionic and electronic conductor (MIEC) phase, and ionic conductor phase (IC).

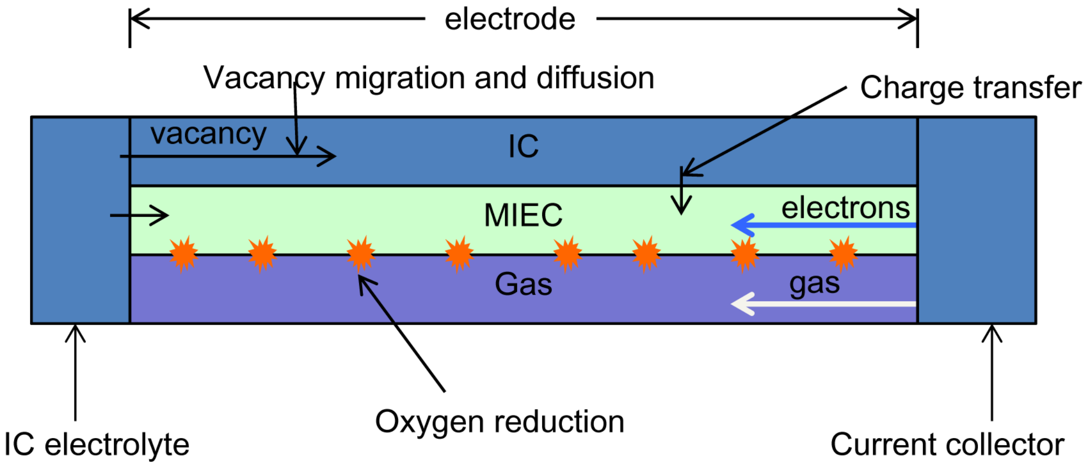

Figure 5.3 SOFC electrode processes

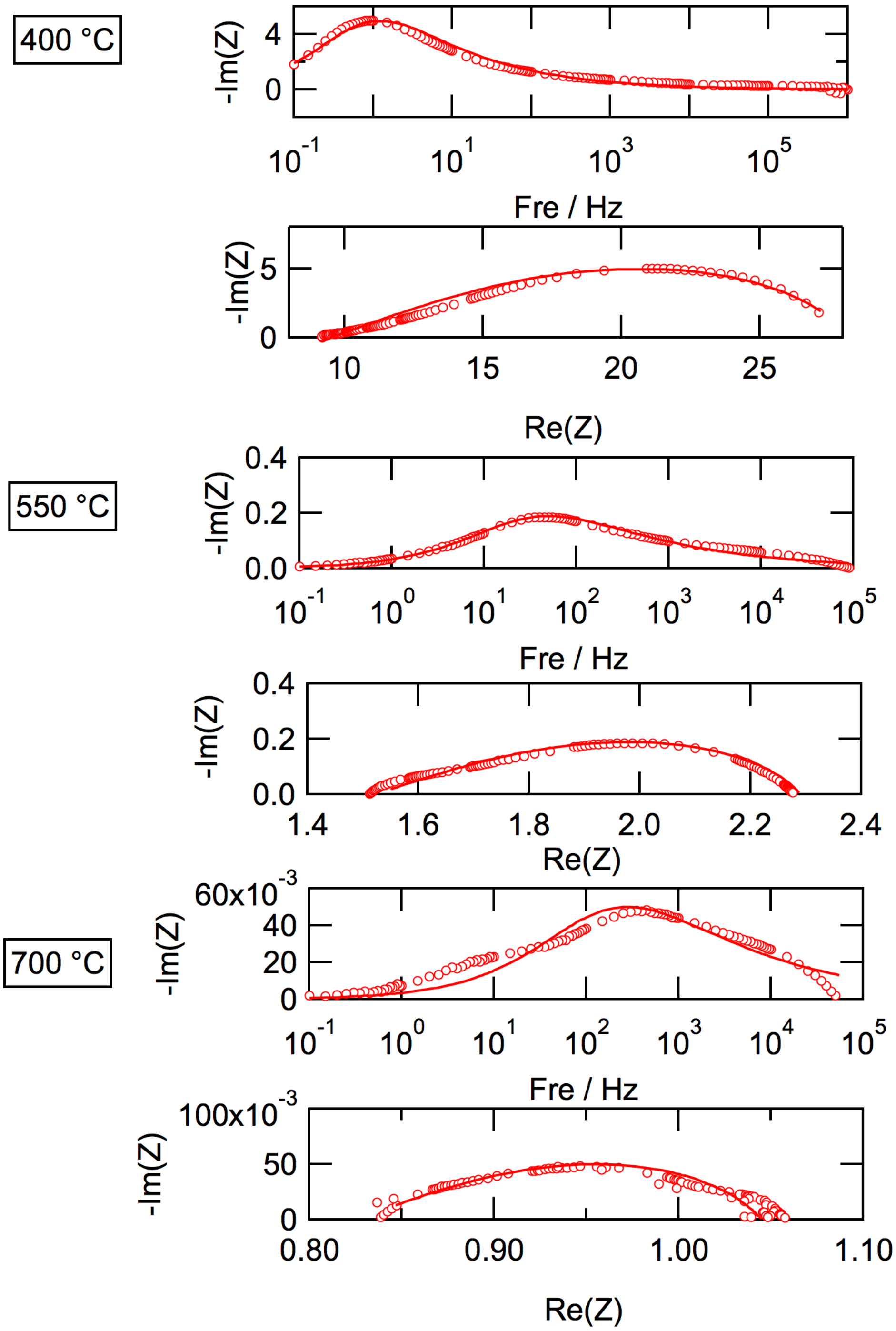

Figure 5.4 Impedance fitting of analytical SOFC cathode model to SSC-GDC experimental data at 13.7 % MIEC infiltration volume at varying temperatures from 400 °C to 700 °C.

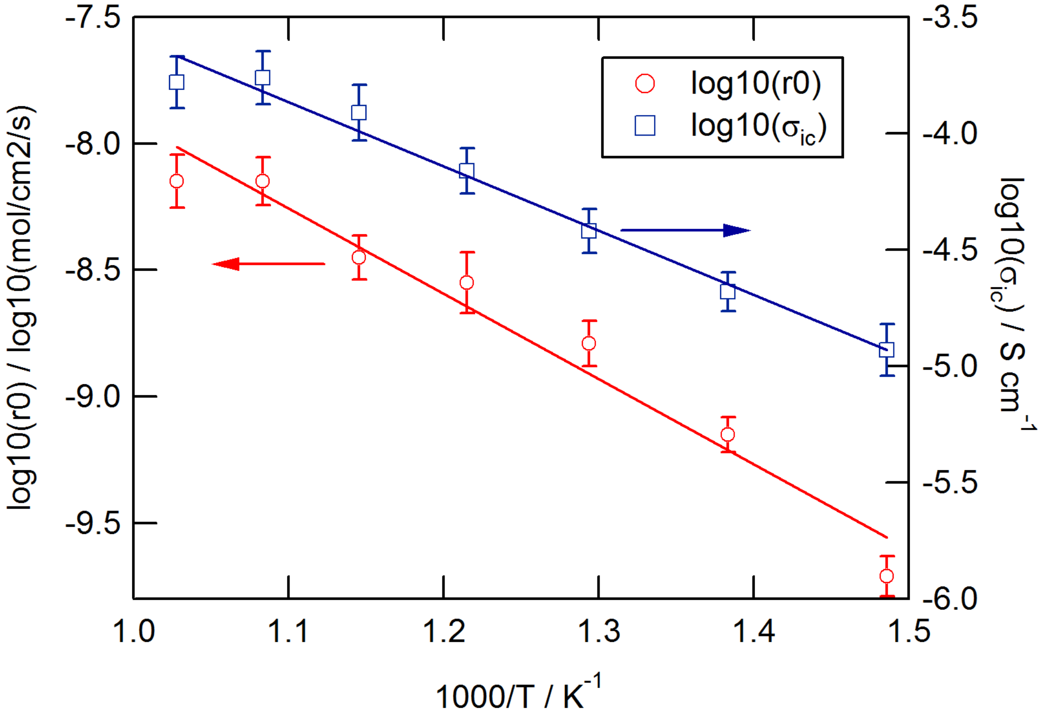

Figure 5.5 Summary of fitted IC conductivity and reaction constant vs. temperature at 13.7 vol%. The slope of fitted line is -3.37 ± 0.3 for xr_0 and -2.75 ± 0.18 for σ_{ic}.

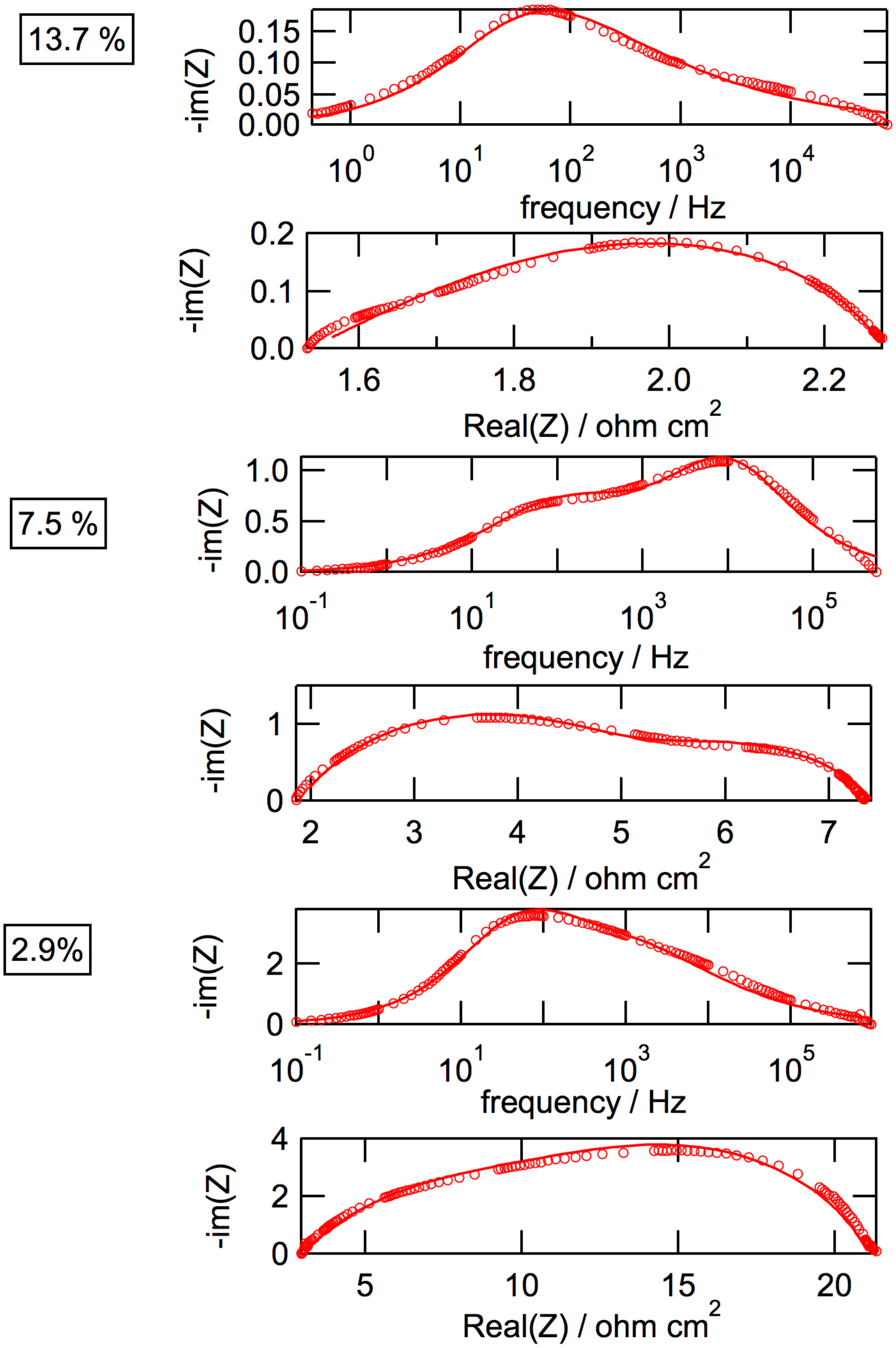

Figure 5.6 Nyquist and Bode plot of low MIEC loading model fitting to SSC-GDC symmetric cell data from 2.0 % to 15.5 vol % at 550 °C. Out of the seven loadings fitted, only three loading percentage were shown here in this figure.

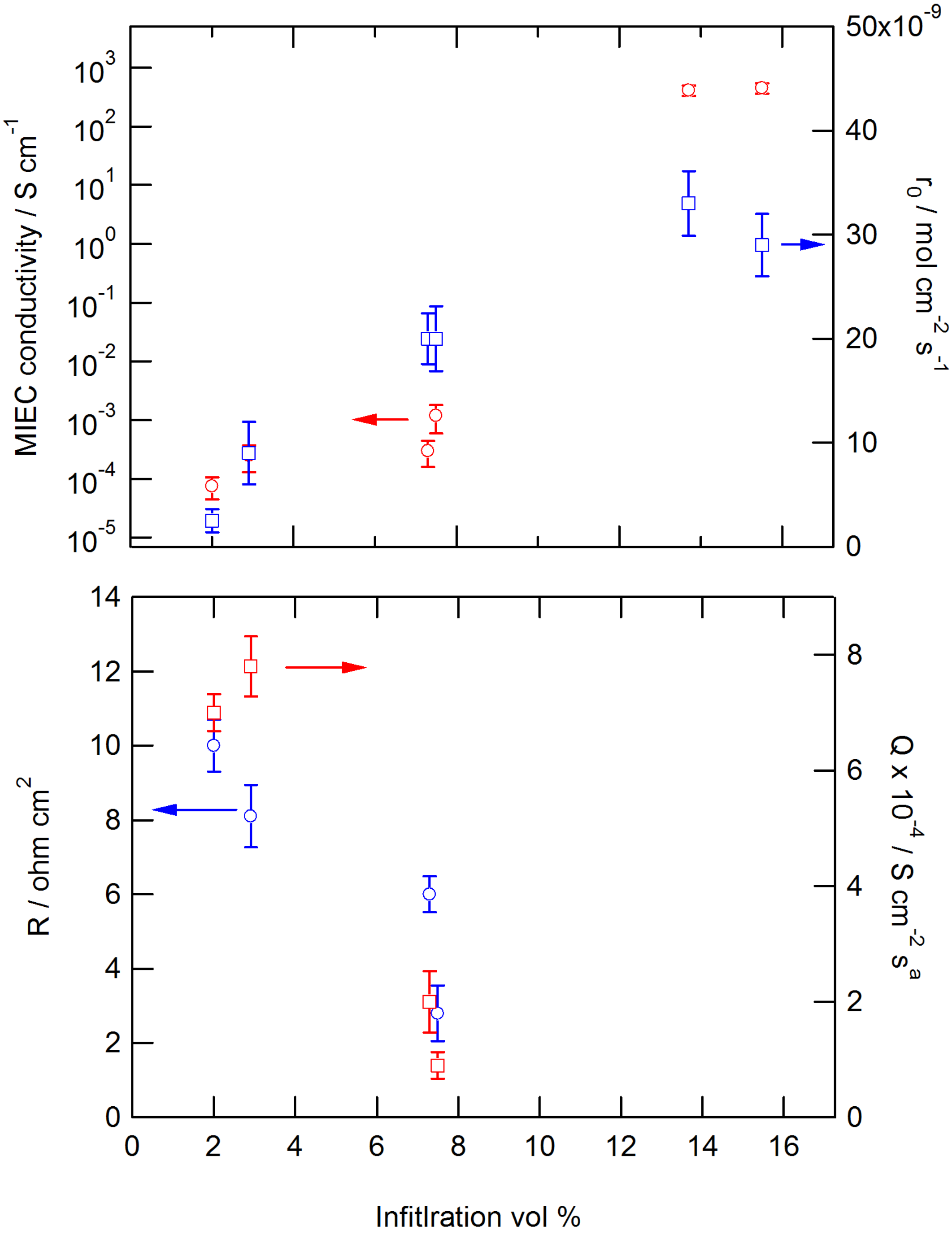

Figure 5.7 Fitting results for MIEC conductivity and reaction constant.

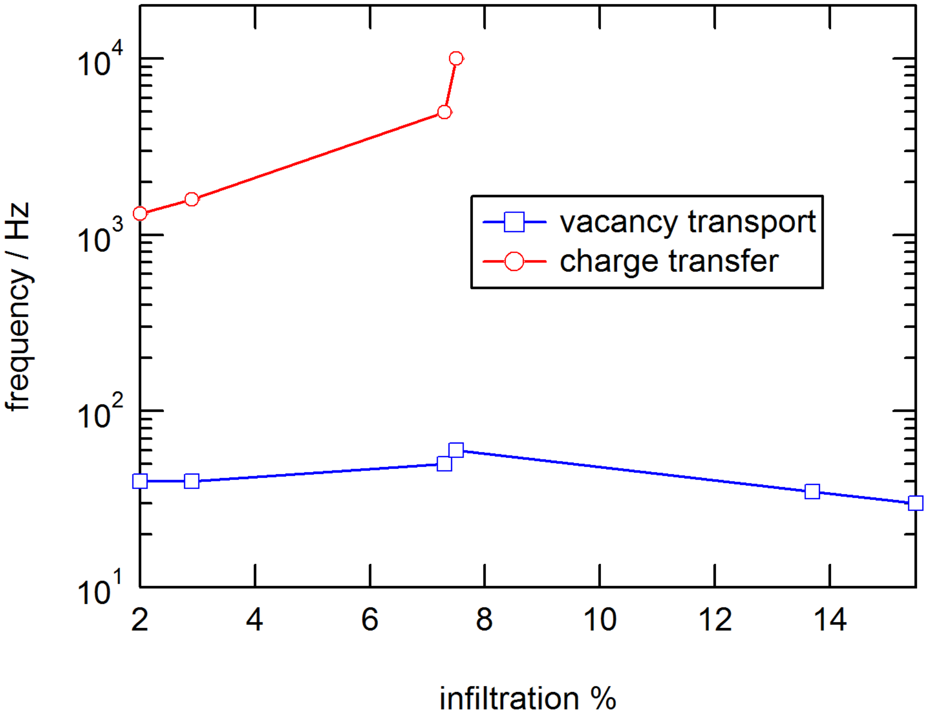

Figure 5.8 Peak frequency comparison at varying loadings. Charge transfer peak frequency were read only at low infiltrations since high infiltration has very insignificant peak on Nyquist plot, making it hard to read.

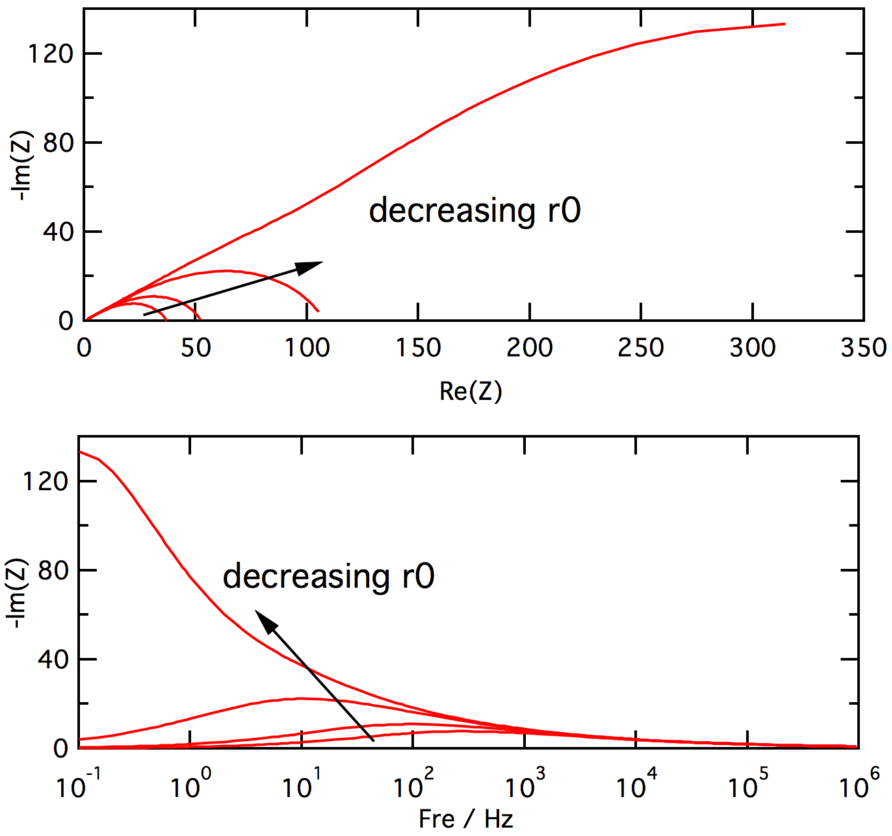

Figure 5.9 Impedance response trend with varying oxygen surface exchange reaction constant. Reaction rate constant r_0 took values of 1×10^{-11}, 1.2×10^{-10}, 5×10^{-10}, 1×10^{-9} mol cm^{-2} s^{-1}. All the other parameters were based on the baseline parameter values.

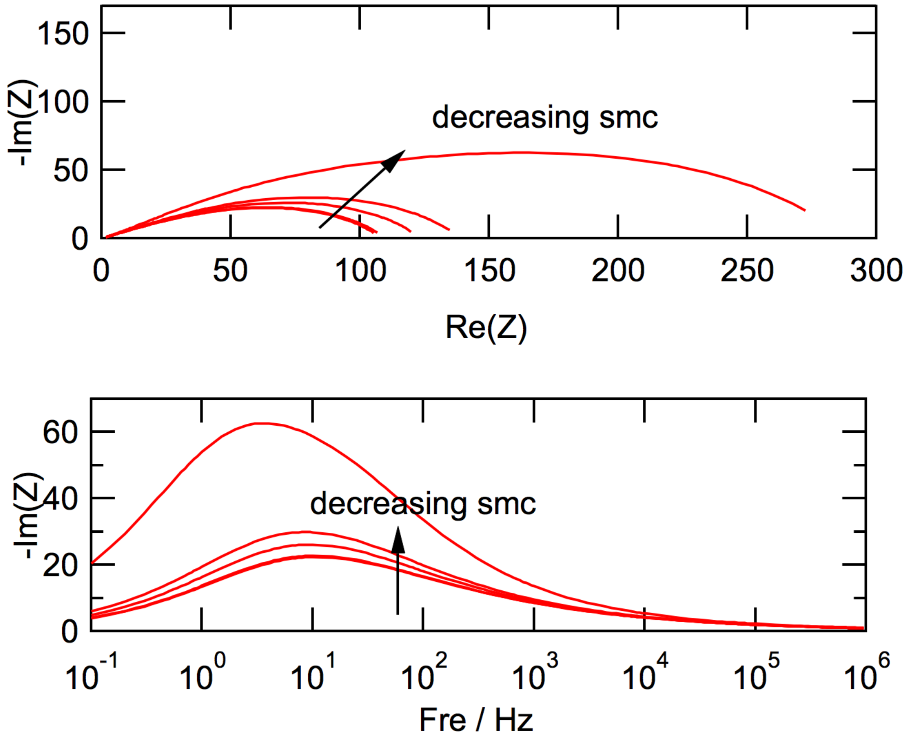

Figure 5.10 Effect of MIEC conductivity on impedance responses. Conductivity values are 1, 1 × 10^{-3}, 1 × 10^{-4}, 1 × 10^{-5}, 5 × 10^{-5}, and 1 × 10^{-6} S cm^{-1}. All the other parameters were based on the baseline parameter values.

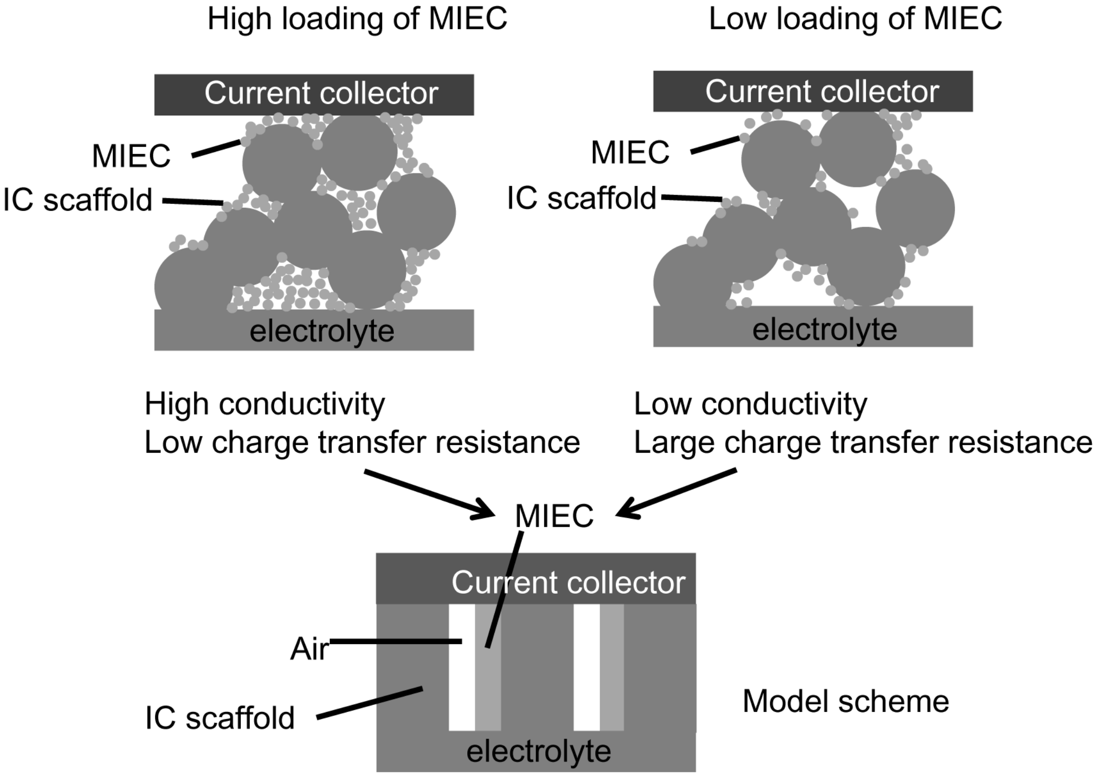

Figure 5.11 Schematic of percolation theory

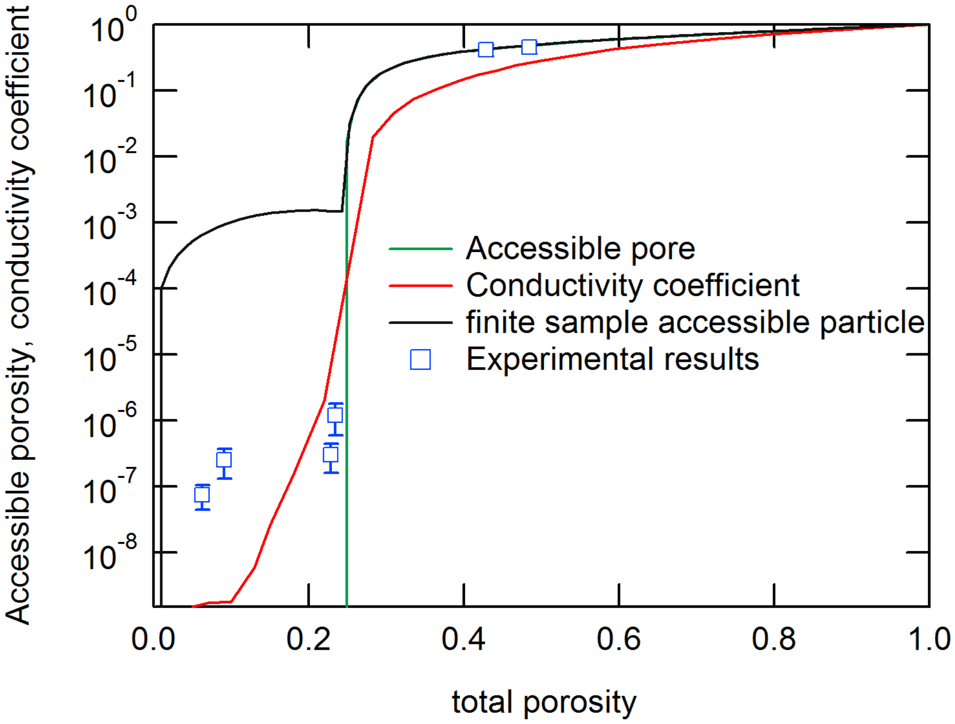

Figure 5.12 Fraction of accessible porosity and effective conductivity as a function of MIEC volume fraction. Bethe lattice approximation has coordination number equal to 5.

REFERENCES

References

1. S.B. Adler, "Factors governing oxygen reduction in solid oxide fuel cell cathodes." *Chemical Reviews*, **104**(10), 4791-843 (2004).

2. J. Mizusaki, "A Chemical Diffusion-Controlled Electrode Reaction at the Compact $La_{1-x}Sr_xMnO_3$ Stabilized Zirconia Interface in Oxygen Atmospheres" *Journal of The Electrochemical Society*, **143**(10), 3065 (1996).

3. S. Adler, "Limitations of charge-transfer models for mixed-conducting oxygen electrodes" *Solid State Ionics*, **135**(1-4), 603-612 (2000).

4. J.D. Nicholas and S. a. Barnett, "Finite-element modeling of idealized infiltrated composite solid oxide fuel cell cathodes" *Journal of The Electrochemical Society*, **156**(4), B458 (2009).

5. V.A.C. Haanappel et al., "Optimisation of processing and microstructural parameters of LSM cathodes to improve the electrochemical performance of anode-supported SOFCs" *Journal of Power Sources*, **141**(2), 216-226 (2005).

6. J. Fleig, "On the width of the electrochemically active region in mixed conducting solid oxide fuel cell cathodes" *Journal of Power Sources*, **105**(2), 228-238 (2002).

7. S. Wang, "High temperature properties of $La_{0.6}Sr_{0.4}Co_{0.8}Fe_{0.2}O_{3-\delta}$ phase structure and electrical conductivity" *Solid State Ionics*, **159**(1-2), 71-78 (2003).

8. S. Linderoth, N. Bonanos, K.V. Jensen and J.B. Bilde-Sørensen, "Effect of NiO-to-Ni Transformation on Conductivity and Structure of Yttria-Stabilized ZrO_2" *Journal of the American Ceramic Society*, **84**(11), 2652-2656 (2001).

9. J. Fleig, "The polarization of mixed conducting SOFC cathodes: Effects of surface reaction coefficient, ionic conductivity and geometry" *Journal of the European Ceramic Society*, **24**(6), 1343-1347 (2004).

10. A. Svensson, "A mathematical model of the porous SOFC cathode" *Solid State Ionics*, **86-88**(96), 1211-1216 (1996).

11. A.M. Svensson, "Mathematical Modeling of Oxygen Exchange and Transport in Air-Perovskite-Yttria-Stabilized Zirconia Interface Regions" *Journal of The Electrochemical Society*, **145**(4), 1390 (1998).

12. A.M. Svensson, "Mathematical Modeling of Oxygen Exchange and Transport in Air-Perovskite-YSZ Interface Regions" *Journal of The Electrochemical Society*, **144**(8), 2719 (1997).

13. J.D. Nicholas and S. a. Barnett, "Measurements and Modeling of $Sm_{0.5}Sr_{0.5}CoO_{3-x}$–$Ce_{0.9}Gd_{0.1}O_{1.95}$ SOFC Cathodes Produced Using Infiltrate Solution Additives" *Journal of The Electrochemical Society*, **157**(4), B536 (2010).

14. S. Kakac, a Pramuanjaroenkij and X. Zhou, "A review of numerical modeling of solid oxide fuel cells" *International Journal of Hydrogen Energy*, **32**(7), 761-786 (2007).

15. X. Chen, "Simulation of a composite cathode in solid oxide fuel cells" *Electrochimica Acta*, **49**(11), 1851-1861 (2004).

16. Y. Shi, H. Wang and N. Cai, "Direct two-dimensional electrochemical impedance spectra simulation for solid oxide fuel cell" *Journal of Power Sources*, **208**24-34 (2012).

17. S. Sunde, "Simulations of Composite Electrodes in Fuel Cells" *Journal of Electroceramics*, **5**(2), 153-182 (2000).

18. J. Fleig et al., "Thin Film Microelectrodes in SOFC Electrode Research" *Fuel Cells*, **6**(3-4), 284-292 (2006).

19. C.W. Tanner, "The Effect of Porous Composite Electrode Structure on Solid Oxide Fuel Cell Performance" *Journal of The Electrochemical Society*, **144**(1), 21 (1997).

20. M. Sahimi, "*Applications of percolation theory*" 258 (Taylor & Francis: 1994).

21. J.S. Newman and K.E. Thomas-Alyea, "*Electrochemical systems*" 647 (Wiley-IEEE: 2004).

22. J.S. Newman and K.E. Thomas-Alyea, "*Electrochemical systems*" 647 (Wiley-IEEE: 2004).

23. S.B. Adler, "Electrode Kinetics of Porous Mixed-Conducting Oxygen Electrodes" *Journal of The Electrochemical Society*, **143**(11), 3554 (1996).

24. M.E. Orazem and B. Tribollet, "*Electrochemical Impedance Spectroscopy*" *Analysis*, (2008).

25. M.E. Orazem and B. Tribollet, "*Electrochemical impedance spectroscopy*" 523 (Wiley-Interscience: 2008).

26. W.M. Saltzman and R. Langer, "Transport rates of proteins in porous materials with known microgeometry." *Biophysical journal*, **55**(1), 163-71 (1989).

27. R.G. Larson, L.E. Scriven and H.T. Davis, "Percolation theory of residual phases in porous media" *Nature*, **268**(5619), 409-413 (1977).

28. M.E. Fisher and J.W. Essam, "Some Cluster Size and Percolation Problems" *Journal of Mathematical Physics*, **2**(4), 609 (1961).

29. R.B. Stinchcombe, "The branching model for percolation theory and electrical conductivity" *Journal of Physics C: Solid State Physics*, **6**(1), L1-L5 (1973).

30. K.K. Mohanty, J.M. Ottino and H.T. Davis, "Reaction and transport in disordered composite media: Introduction of percolation concepts" *Chemical Engineering Science*, **37**(6), 905-924 (1982).

31. S. Reyes, "Estimation of effective transport coefficients in porous solids based on percolation concepts" *Chemical Engineering Science*, **40**(9), 1723-1734 (1985).

Chapter 6 Summary

Porous electrode is a fundamental component for modern fuel cell systems. The current work tried to synthesize carbon based porous electrodes and used biocatalyst as test platform to assess their possible applications. Porous rotating disk electrode and composite solid oxide fuel cell have been modeled to study transport and kinetics mechanisms.

Carbon fiber microelectrodes (CFME) were fabricated to mimic the microenvironment of carbon fiber paper based porous electrodes. They are also miniature electrodes for small-scale applications. Carbon nanotubes (CNTs) were treated to introduce carboxylate group on the surface to enhance hydrophilicity, and *N,N*-dimenthylformamide (DMF) organic solvent was used to make CNT suspensions. Carbon nanotubes (CNTs) coated on CFME formed a homogeneously intertwined matrix. Biocatalysts applied fully infiltrate this matrix to form a composite, with a 6.4 fold increase of glucose oxidation current comparing to CNT free control CFMEs. This work opened up a way to study carbon fiber based porous electrodes. Subsequently, the coating process for coating CNTs needs to be scaled up to widen its applications. Dispersion of CNTs with surfactants, and/or other solvents needs to be studied for a more homogeneous and faster casting of CNT porous matrix. Fabrication technique for CFMES shall be improved to eliminate the observed internal resistances.

Based on the CNT based porous matrix, polystyrene beads were used as template to tune the porous structure to accommodate biomolecule transport. The macro-pores enhanced the fuel transport and the current densities were doubled due to the improvement. Template tuning of macro-porosity is a promising candidate to improve high surface area porous materials. However, it has been observed that the dispersion of template polystyrene beads did not form uniform suspension with CNTs in DMF. The dispersion of PS/CNT thus shall be studied and optimized to ultimately improve the porous morphologies.

Porous rotating disk electrode (PRDE) is a system with analytically solved flow field. A model was proposed to include enzyme kinetics, diffusion and convection transport at varying rotations, as well as the electrolyte transport of substrate in electrolyte outside the porous media. This model was demonstrated to be able to fit to experimental data with very good accuracy by assuming and fitting certain kinetic and transport parameters. The current model extends the understanding towards the behavior of PRDE systems. The assumed parameter values limited the study of enzymatic PRDEs, thus parameter value inputs from other experiments, like thin film bioelectrodes, is key to facilitate further understandings. It is also important to the current model to test with PRDEs made of other catalysts and different porosities.

Composite solid oxide fuel cell cathodes with insufficient mixed ionic and electronic conductor (MIEC) loadings at varying temperatures were modeled with the MIEC conductivity and oxygen surface exchange reaction rate fitted to experimental data. Percolation theory was utilized to explain the fitted trends. This model is the first to explain the observed increasing polarization resistance when MIEC is insufficiently loaded. The next step in this modeling work is to find the effect of various design parameters, including electrode thickness, MIEC particle size, MIEC volume fraction, temperature, and non-zero currents.

In summary, this dissertation presents various porous electrodes applied to biocatalysis and solid oxide fuel cell oxygen reductions. Carbon nanotubes were successfully dispersed and formed a porous media that’s effective in increasing the surface area and facilitate mediated glucose oxidations. Polystyrene beads as templates introduced macro-pores at 500 nm into carbon nanotube porous matrix, leading to a double of current density comparing to macro-pore free cases. Focused ion beam cut open the macro-pore embedding matrix, revealing uniform distribution of macro-pores and infiltrated biocatalytic hydrogels. Modeling work has been done for porous rotating disk electrode by considering diffusion and convection at all the rotations, generating very good fit to carbonaceous form monolith electrode coated with biocatalysts. Solid oxide fuel cell composite cathode has been modeled to fit to impedance responses. Both cases with sufficient or insufficient mixed ionic and electronic conductor within cathode volume were studied. The model showed consistent trend with observation and percolation theories.

APPENDIX

A.1 Velocity field in electrolyte outside of PRDE

It was proposed by Stuart that the velocity field outside of a RDE can be found by solving the following dimensionless boundary value problem:[1]

$$\begin{aligned} &F^2 - G^2 + HF' = F'' \\ &2FG + HG' = G'' \\ &2F + H' = 0 \end{aligned} \tag{1}$$

with boundary condition:

$$\begin{aligned} &@\zeta = 0, F = 0, G = 1, H = -a \\ &@\zeta = \infty, F = G = 0 \end{aligned} \tag{2}$$

where all the variables are dimensionless, with definition:

$$\begin{aligned} &u = r\omega F(\zeta) \\ &v = r\omega G(\zeta) \\ &w = (v\omega)^{\frac{1}{2}} H(\zeta) \\ &\zeta = (\omega / v)^{\frac{1}{2}} z \end{aligned} \tag{3}$$

where u,v, and w are radial, angular, and axial velocities respectively. ω and v are rotation rate and kinematic viscosity. From these definitions, a length $(v/\omega)^{\frac{1}{2}}$, time ω^{-1}, and thus a velocity $(v\omega)^{\frac{1}{2}}$ are scaling factors for this problem.

The variable *a* corresponds to the RDE surface suction speed. When $a = 0$, the solution reduces to the flat surface RDE case, which leads to the well-known Levich equation. In a PRDE system, parameter *a* is directly related to rotation speed and porous media permeability, as shown in Eq. 3.

Although Stuart proposed the boundary value problem setup, he was not able to give a general numerical solution due to the limited calculation power. Here we explore the solution with numerical calculations.

As a result of the general example, Figure A.1 shows the numerically calculated *H* at varying values of suction speed, *a*. As a general trend, it can be seen that, with increasing suction, axial velocity varations decrease. A maximum velocity is reached at large distance $\zeta = 1$, corresponding to the physical distance $(\nu / \omega)^{\frac{1}{2}}$

A simplification can be implemented given that the diffusion boundary layer thickness is usually only of order $\zeta = 0.01$, and H is therefore close to $-a$. At this distance interval, the velocity profile is shown in Figure A.2. The velocity profile under this range can be well represented by a parabolic curve, with the second-order coefficient a function of *a*:

$$\begin{aligned} H &= -a - a_1\zeta^2 \\ a_1 &= -0.049 \bullet a^3 + 0.0060 \bullet a^2 - 0.078 \bullet a + 0.50 \end{aligned} \tag{4}$$

This expression therefore describes convection external to the PRDE, with the only input being suction parameter, *a*, calculated from Eq. 4.1.

Thus the final expression for velocity in electrolyte is:

$$q_{ze} = \sqrt{\omega \nu}\left(-a - a_1 \frac{\omega}{\nu}(z-h)^2\right) \quad (5)$$

It should be noted that the expression for q_{ze} calculation is only for large Schmidt number, Sc, and small dimensionless distance, ζ, from the PRDE/electrolyte interface, which is defined as:

$$\zeta = \sqrt{\frac{\omega}{\nu}}(z-h) \quad (6)$$

For aqueous systems, $Sc \sim 1000$, and ζ

A.2 Derivation of SOFC matrix equation

Starting from equation:

$$\frac{\partial^2 c}{\partial \xi^2} = K \bullet c \quad (7)$$

the general solution for c can be expressed as:

$$c = A_1 e^{-\sqrt{K}\xi} + A_2 e^{\sqrt{K}\xi} \quad (8)$$

where A_1 and A_2 are coefficient constants that can be defined from boundary conditions. Based on the solution above, the general solution for μ_e is:

$$\mu_e = \frac{\mu er}{K} c + A_3 \xi + A_4 \quad (9)$$

From boundary condition equation:

$$c - 2\mu_e = 0\Big|_{\xi=0} \tag{10}$$

The following equation can be derived:

$$\left(1 - \frac{2\mu er}{K}\right)A_1 + \left(1 - \frac{2\mu er}{K}\right)A_2 - 2A_4 = 0 \tag{9}$$

From boundary condition equation:

$$\nabla\mu_e = 0\Big|_{\xi=0} \tag{12}$$

it can be derived:

$$\frac{\mu er}{-\sqrt{K}}A_1 + \frac{\mu er}{\sqrt{K}}A_2 + A_3 = 0 \tag{13}$$

From boundary condition equation:

$$\nabla\left(c - 2\mu_e\right) = 0\Big|_{\xi=1} \tag{14}$$

it can be derived:

$$\left(-\sqrt{K} + \frac{2\mu er}{\sqrt{K}}\right)e^{-\sqrt{K}} \bullet A_1 + \left(\sqrt{K} - \frac{2\mu er}{\sqrt{K}}\right)e^{\sqrt{K}} \bullet A_2 - 2A_3 = 0 \tag{11}$$

From boundary condition equation:

$$\mu_e = \mu_{e,applied} \tag{15}$$

it can be derived:

$$\frac{\mu er}{K} e^{-\sqrt{K}} \bullet A_1 + \frac{\mu er}{K} e^{\sqrt{K}} \bullet A_2 + A_3 + A_4 = \mu_{e0} \tag{12}$$

Notice that equation (9) through (12) are linear equations for unknowns of A_i. Combination of these four equations yields matrix equation:

$$\begin{bmatrix} 1-\dfrac{2\mu er}{K} & 1-\dfrac{2\mu er}{K} & 0 & -2 \\ \dfrac{\mu er}{-\sqrt{K}} & \dfrac{\mu er}{\sqrt{K}} & 1 & 0 \\ \left(-\sqrt{K}+\dfrac{2\mu er}{\sqrt{K}}\right)e^{-\sqrt{K}} & \left(\sqrt{K}-\dfrac{2\mu er}{\sqrt{K}}\right)e^{\sqrt{K}} & -2 & 0 \\ \dfrac{\mu er}{K}e^{-\sqrt{K}} & \dfrac{\mu er}{K}e^{\sqrt{K}} & 1 & 1 \end{bmatrix} \bullet \begin{bmatrix} A_1 \\ A_2 \\ A_3 \\ A_4 \end{bmatrix} = \begin{bmatrix} 0 \\ 0 \\ 0 \\ \mu_{e0} \end{bmatrix} \tag{17}$$

A.3 Porous rotating disk electrode model Matlab code

All the following codes should be put into the current working folder under Matlab to work. Every section has the location of the file,with “~” representing the work folder. For example, “~/@profile/calc.m” means “calc.m” is put into the subfolder “@profile” of the current working folder.

A.3.1 Flow field with surface suction (~/stuart.m)

The following code is for the calculation of dimensionless velocity field within the electrolyte (not in the PRDE).

```
classdef stuart < handle
% dimensionless axial velocity H in electrolyte
%
% creation: s = stuart(a,zinf); s = stuart(a); s = stuart;
% z is zeta here;  = sqrt(w/v)*height
% zinf: zinf for estimation. It is NOT the actual calculation
zinf.
% This option is used only for better precision of evaluation.
%
% ==== properties ====
% input:
% a - suction parameter
% zinf=0.3 - zeta infinity for evaluation, calculation infinite
is
% at zinff, which is a totally different private property
%
% output:
% H: axial velocity series. = qz/sqrt(v*w)
% zinf: evaluation range
% z: z series based on zinf
%
% options:
% msgon = false
%
% ==== methods ====
% calc - calculation of H. Any change in other parameters has to
be
% followed with the excution of this function to take effect.
%
% doPlot - make plot
%
% version:
% stuart-1.4 : improve evaluation resolution near surface at
large zinf
% dependence:
%


    properties
        a % suction parameter
        zinf % estimation
        H % axial velocity series
        msgon = false
    end

    properties (Dependent = true)
        z % depend on zinf. z series
    end
```

```
    properties (SetAccess = private)
        zinff = 5% large int boundary
    end

    methods
        % constructor
        function s = stuart(a,zinf)
            if nargin < 2, zinf = 0.3; end
            if nargin < 1, a = 0; end

            s.a = a;
            s.zinf = zinf;
            s.calc();
        end

        % dependent variable methods

        function value = get.z(s)
            if s.zinff >= s.zinf % V1.4
                value = linspace(0,s.zinf,500);
            else
                value = [linspace(0,s.zinff,50) ...
                        linspace(s.zinff+(s.zinf-
s.zinff)/500,s.zinf,480)];
            end
        end

        function calc(s)
            if s.zinf < 0
                % upper limit can not be < 0
                error('stuart:intervalChk','wrong interval
range');

                % use 0.4 as threshold
            elseif s.zinf < 0.4 && s.a < 1
                % small zeta upper limit
                s.H = s.low_int();
            else
                % large zeta upper limit
                s.H = s.large_int();
            end
        end

        function H = low_int(s)
            % Based on numerical results
            if s.msgon, disp('stuart:low_int'); end
            a1= -0.049279 * s.a^3 + 0.0060009 * s.a^2 -...
```

```
                0.078468 * s.a + 0.50476;

            % return value
            H = -s.a - a1*s.z.^2;
        end

        function H = large_int(s)
            if s.msgon, disp('stuart:large_int'); end

            % to guarantee smooth fitting...
            % note: the bvp eq. is not stable for large zinff
            % zinff, the value used for numerical calc

            if s.a > 8
                if s.a > 100
                    if s.a > 1000
                        s.zinff = 0.01;
                    else
                        s.zinff = 0.1;
                    end
                else
                    s.zinff = 1;
                end

            end

            % calculation
            zfit = linspace(0,s.zinff,5);
            solinit = bvpinit(zfit,[1 1 1 1 1]);
            sol = bvp4c(@ge,@bc,solinit);

            % return value
            zs = s.z; % generate zs based on zinf, could be  %
%short
            u = zeros(5,length(zs));
            u(:,zs<=s.zinff) = deval(sol,zs(zs<=s.zinff));
            temp = deval(sol,s.zinff);

% sometimes zinf > zinff, but for zinf > 5, bvp4c crashes for
% such high values. To accout for such issue, we approximate
% higher values with u(z=5)
            for i = 1:5
                u(i,zs>s.zinff) = temp(i);
            end

            H = u(5,:);

            function dudz = ge(z,u)
```

```
                F = u(1); Fp = u(2);
                G = u(3); Gp = u(4);
                H = u(5);
                dudz = [Fp
                        F.^2 - G.^2 + H*Fp
                        Gp
                        2*F.*G + H.*Gp
                        -2*F];
            end % ge

            function res = bc(ua,ub)
                res = [ua(1)
                       ua(3) - 1
                       ua(5) + s.a
                       ub(1)
                       ub(3)];
            end % bc
        end % large_int

        function doPlot(s)
            plot(s.z,s.H);
            xlabel('zeta');
            ylabel('axial velocity H');
        end % doPlot

    end % methods

end % classdef
```

A.3.2 Ping pong bi bi kinetics (~/ppbb.m)

```
classdef ppbb < handle
% ppbb kinetics
%
% creation: m = ppbb(in); m = ppbb;
% all c [=] mol/cm3, rate [=] mol/cm^3/s
%
% ==== properties ====
% in = inp - inp obj, parameter control
%
% methods:
% rate = rxn(c) - rxn rate calc.
% doPlot(cinf) - demo rate from [0 cinf]
%
% version:
% ppbb-1.0
% dependence:
% inp-1

    properties
        in = inp;
    end

    methods
        function self = ppbb(in)
            if nargin < 1
                self.in = inp;
            else
                self.in = in;
            end
        end

        function rate = rxn(self,c)
            % Reaction rate calculation
            %
            % rate [=] mol/cm^3/s; c [=] mol/cm^3 [=] 1e-6 mM

            % dimensionless potential
            eta = (self.in.E-self.in.Er)*self.in.n*...
self.in.F/self.in.R/self.in.T;

            % mol/cm^3, active mediator concentration
            M = exp(eta)/(1+exp(eta))*self.in.Mt;

            % Ping pong bi bi.
```

```
            % rxn rate, mol/cm^3/s
            rate(c>0) = 
self.in.Vmax.*M.*c(c>0)./(M.*c(c>0)+c(c>0).*...

self.in.Km+M.*self.in.Ks);
            rate(c<=0) = 0;
            % use this out(c>0) syntax for c array calculation;

        end

        function out = doPlot(self,cinf)
            % give cinf [=] mol/cm3
            c_series = linspace(0,cinf,100);
            rxn_series = self.rxn(c_series);
            plot(c_series,rxn_series);
            xlabel('concentration / mol/cm^3');
            ylabel('rxn rate / mol/cm^3/s');
            figure(gcf);
            out.c_series = c_series;
            out.rxn_series = rxn_series;
        end
    end % methods

end % classdef
```

A.3.3 Input parameter value assignment (~/input.m)

```
classdef inp
% Input class definition.
%


    properties
        % Kinetic parameters. To be used in ppbb.m
            Ks = 10.6e-5; %mol/cm3
            Vmax = 4.1e-7; %mol/cm3/s
            Mt = 660e-6; % mol/cm^3;
            Km = 81.6e-6; % mol/cm^3, Michaelis constant,
%Harshal
            Er = 0.55; % V vs. SHE, redox potential for
%mediator;

            % experimentally controlled parameters
            c_inf = 100e-6; %mol/cm^3, bulk concentration
            w = 10; % /s, rotation rate
            E = 1; %V, electrochemical potential vs. SHE
            T = 300; %K, temperature

            % intrinsic parameters
            %-- transport --
            k = 5.24e-11;
%cm^2, permeability for porous media. Ref: Millington1961.

            v = 0.01;
% cm^2/s, 0.01 for water; kinematic viscosity in hydrogel.

% To be fitted. D = 7e-6; %cm^2/s, glucose bulk diffusivity.**
            D = 8.4e-6;

            %== Deff calc ==
     %porosity of carbonaceous monolith, Flexer2011
            porosity = 0.74;
     %to be fitted. Diffusivity decrease in hydrogel,Gehrke1997
            K_hydrogel = 0.6;


            %-- geometry --
            h = 0.1; %cm, PRDE thickness
            Radius = 0.25; %cm, radius. It is not used actually.

    end
```

```
    properties (Constant)
                %-- constants --
            n = 4; % equivalent glucose oxidation electrons
            F = 96485; %C/mol, Faraday constant
            R = 8.314; %J/K/mol, gas constant
    end
end % classdef
```

A.3.4 Fitting to experimental results (~/expfit.m)

```
classdef expfit < handle
% this is for rotation variation only
%
% ==== creation ====
% f_high = expfit([xy],[fitstr],[initval]);
%
% ==== properties ====
% input:
% xy - data to be fitted. xy(:,1) rotation w, xy(:,2) curr
density
% fitstr: cell array containing parameter names to be fitted
% initval: initial guess values for the parameters.
%
% e.g.
% fitstr = {'Ks','K_hydrogel','k','Vmax'};
% initval = [9.96e-5, 0.81, 5.16e-11, 3.92e-7];
% xy = high loading experimental data
%
% output:
% fitval % fitted parameter values
% fiter % fitted parameter error estimation
% w_s % evaluated w series for plotting
% curr_s % curr series for plotting
% result - fitfun2 initial returned struct (advanced users)
%
% onew - intermediate calc result for one w
%
% ==== methods ====
% fit() - carry out fitting procedure. Extremely time consuming.
% wplot() - sqrt(w) vs. curr with exp and fitted results. Use it
% after
%           fit() was executed;
%
% version:
% expfit-1.1
% dependence:
% inp-1, profile-1
```

```
    properties
        xy % exp data, xy(:,1) rotation w, xy(:,2) curr density
        fitstr
          % fit string array containing parameter name to
          % be fitted
        initval % initial guess value for parameters
        onew % profile object for one w
    end

    properties (SetAccess = protected)
        fitval % fitted parameter values
        fiter % fitted parameter error estimation
        inpu % fitting only
        params % fitting only
        in = inp % initial generated inp obj for fitting
        result % fitfun2 initial returned struct
        w_s % evaluated w series for plotting
        curr_s % curr series for plotting
    end

    methods
        % === constructor ===
        function s = expfit(xy,fitstr,initval)
            % fitstr is a string array
            % xy(:,1): rotation; xy(:,2): current density

   % the following is using high loading data as example
            if nargin < 3
                initval = [9.96e-5, 0.81, 5.16e-11, 3.92e-7];
            end

            if nargin < 2
                fitstr = {'Ks','K_hydrogel','k','Vmax'};
            end

            if nargin < 1
                xy = ...
                    [50.818506  3.47085
                    103.999204  3.60538
                    206.106221  3.87444
                    314.0976398 4.27803
                    415.996816  4.76233
                    518.5776473 5.30045
                    622.5274503 5.70404
                    725.2626025 6.05381
                    835.8401388 6.26906
                    935.9989548 6.4574
```

```
          1035.436555 6.59193];
      end

      s.xy = xy;
      s.fitstr = fitstr;
      s.initval = initval;

      s.onew = profile(s.in);

      % fitting parameter
      s.init();
    end

    function init(s)
      s.inpu.w = 20; % place holder
      s.params(1).data = 'w';

      for i = 1:length(s.fitstr)
        eval(['s.inpu.' s.fitstr{i} '='
num2str(s.initval(i)) ';']);
        eval(['s.fitval.' s.fitstr{i} '='
num2str(s.initval(i)) ';']);
        eval(['s.params(' num2str(i+1) ').param='''
s.fitstr{i} ''';']);
        eval(['s.params(' num2str(i+1) ').init='
num2str(s.initval(i)) ';']);
      end
    end

    function fit(s)


% fitting procedure, result will also be printed after this line
      s.result =...
        funfit2(@s.fitfun,s.xy,s.inpu,s.params,true);

      for i = 1:length(s.fitstr)
        eval(['s.fitval.' s.fitstr{i} '='...
           num2str(s.result.pf(i)) ';']);
        eval(['s.fiter.' s.fitstr{i} '='...
          num2str(s.result.ci(i,2) - s.result.pf(i))
';']);
      end

      % result evaluation
      rw = max(s.xy(:,1));
      lw = min(s.xy(:,1));
      s.w_s = linspace(lw,rw,20);
```

```
            s.curr_s = zeros(size(s.w_s));
            calc_in = s.fitval;
            for i = 1:length(s.w_s)
                disp(['calculating ' num2str(i) 'th of i...']);
                calc_in.w = s.w_s(i);
                s.curr_s(i) = s.fitfun(calc_in);
            end

        end

        % fitfun definition for funfit2
        function curr = fitfun(s,inpu)
            s.in.w = inpu.w;
            for i = 1:length(s.fitstr)
                eval(['s.in.' s.fitstr{i} '= inpu.' s.fitstr{i}
';']);
            end

            s.onew.in = s.in;

            curr = s.onew.current;
        end

        % === utility ===
        function wplot(s)
            figure;
            plot(sqrt(s.w_s),s.curr_s,'-',...
                sqrt(s.xy(:,1)),s.xy(:,2),'o');
            xlabel('sqrt of rotation / s-1/2');
            ylabel('current density / mA cm-2');
            legend('fitted','experimental');
        end
    end

end % classdef
```

A.3.5 Concentration profile generation

Basic class definition (~/@profile/profile.m)

```
classdef profile < handle
% Calculate concentration profile with both electrolyte and PRDE
%
% creation: m = profile(in); m = profile;
% in: a "inp" object. If not given ,use inp default values.
%
% ==== properties ====
% input:
% in - inp obj, input paramter
% kinetics = ppbb - available kinetics obj.
%
% dependent:
% a - suction. depend: in. = (w/v)^1.5*2*k*h;
% zinf - z infinity. depend: in
% Deff - effective diffusivity in PRDE. depend: in
%
% output:
% sol - solved sol structure;
% z_series % evaluation from z to zinf
% c_series % evaluation from z to zinf
% current %mA/cm2, output current
%
% ==== methods ====
% qzplot() - velocity plot
% cplot() - concentration plot
% calc() - automatically carried out everytime obj.in is
changed.
%
% version:
% profile-1.4
% dependence:
% ppbb-1, inp-1, stuart-1
%
% to do:
% update aa and la to newest result




    properties
        kinetics = ppbb
        diffusion_inclusion = true
    end
```

```
% see "Listening for Changes to Property Values" for details
    properties (SetObservable, AbortSet)
        in % input parameter
    end

    properties (Dependent, Hidden)
        zinf % calculated infinity for numerical calculation
        Deff % effective diffusivity, cm2/s
    end

    properties (SetAccess = protected) % mostly results
        sol % numerically solved struct
        z_series % evaluation from z to zinf
        c_series % evaluation from z to zinf
        cp_series % derivitive of c from z to zinf
        current %mA/cm2, output current
        a % suction parameter
    end

    properties (SetAccess = private)
        % previously calculated zinf location
        % a
        aa =
[0,0.0344827586206897,0.0689655172413793,0.103448275862069,0.137
931034482759,0.172413793103448,0.206896551724138,0.2413793103448
28,0.275862068965517,0.310344827586207,0.344827586206897,0.37931
0344827586,0.413793103448276,0.448275862068966,0.482758620689655
,0.517241379310345,0.551724137931035,0.586206896551724,0.6206896
55172414,0.655172413793103,0.689655172413793,0.724137931034483,0
.758620689655172,0.793103448275862,0.827586206896552,0.862068965
517241,0.896551724137931,0.931034482758621,0.965517241379310,1;]
;
        % zinf location
        la =
[0.235754455445545,0.0874527452745274,0.0462088208820882,0.03102
87828782878,0.0233165316531653,0.0186659665966597,0.015562556255
6256,0.0133438943894389,0.0116805280528053,0.0103806380638064,0.
00934488448844885,0.00849639963996400,0.00778757875787579,0.0071
8901890189019,0.00667614761476148,0.00623258325832583,0.00584194
419441944,0.00549918991899190,0.00519423942394239,0.004920092009
20092,0.00467310731073107,0.00445160516051605,0.004249704970497
5,0.00406348634863486,0.00389490949094910,0.00374005400540054,0.
00359499949995000,0.00346170617061706,0.00333821382138214,0.0032
2452245224522;];

        % stuart class object for velocity flow in electrolyte
        h_electrolyte
```

```
    end

    methods
        %% === constructor ===
        function s = profile(in)
            % initialize
            if nargin < 1, in = inp; end

            s.in = in;
            s.a =
(s.in.w/s.in.v)^1.5*2*s.in.k*s.in.h*s.in.porosity;
            s.h_electrolyte = ...
                stuart(s.a,s.z2zeta(s.zinf-s.in.h));

            if s.a > max(s.aa)
                error('a value out of bound!');
            end

            % calculation of profile
            s.calc;

            % listen to in and a value change
            addlistener(s,'in','PostSet',@s.in_postset);
        end

        function in_postset(s,~,~) % if "in" changes
            s.kinetics.in = s.in; % link handle
            s.a =
(s.in.w/s.in.v)^1.5*2*s.in.k*s.in.h*s.in.porosity;
            s.h_electrolyte.zinf = s.z2zeta(s.zinf-s.in.h);
            s.h_electrolyte.a = s.a;
            s.h_electrolyte.calc;

            % conditional calculation
            if s.diffusion_inclusion
                s.calc;
            else
                s.calc_no_diffusion;
            end
        end

        % === dependent properties ===
        function value = get.zinf(s)
            value = s.in.h +...
                    s.zeta2z(interp1(s.aa,s.la,s.a));
        end

        function value = get.Deff(s)
```

```
            % correct for both hydryogel and monolith
            % cm^2/s
            value = s.in.D*s.in.porosity^1.5*s.in.K_hydrogel;
        end


        %% === utilities ===
        function z = zeta2z(s,zeta)
            z = sqrt(s.in.v/s.in.w)*zeta;
        end

        function zeta = z2zeta(s,z)
            % convert z to dimensionless zeta
            zeta = z/sqrt(s.in.v/s.in.w);
        end

        function [z_series q_series] = qzplot(s)
            % show the velocity profile
            z = linspace(0,s.zinf,400);
            qz(z <= s.in.h) = s.qz_porous(z(z <= s.in.h));
            qz(z > s.in.h) = s.qz_electrolyte(z(z > s.in.h));
            figure;
            plot(z,qz);
            xlabel('distance / cm');
            ylabel('velocity / cm s-1');
            figure(gcf);
            z_series = z;
            q_series = qz;
        end

        function cplot(s)
            % concentration profile plot
            figure;
            plot(s.z_series,s.c_series);
            xlabel('height z / cm');ylabel('concentration /
mol/cm3/s');
            figure(gcf);
        end

        %% === qz profile ===
        function out = qz_porous(s,z)
        % calculate the axial velocity

            % cm/s, z-axis velocity within PRDE
            out = -s.in.k*s.in.w^2/s.in.v*2.*z;
        end

        function out = qz_electrolyte(s,z)
```

```
        % Calculate
        % conversion factor H to w
            f = sqrt(s.in.v*s.in.w);
            out =
f*interp1(s.h_electrolyte.z,s.h_electrolyte.H,...
                            s.z2zeta(z-s.in.h));

        end

    end % methods

end % classdef
```

No diffusion included (~/@profile/calc_no_diffusion.m)

```
function calc_no_diffusion(s)
% calculation without considering diffusion with ode45
% note: coordination system change:
% z = 0 is electrolyte/PRDE interface
% z = h is PRDE backend

h = s.in.h; % electrode thickness
cinf = s.in.c_inf; % bulk concentration

zspan = linspace(0,h*0.99999,100);
R = @(c) s.kinetics.rxn(c); % rxn rate
qz = @(z) -s.qz_porous(h-z); % flow field rate

[zs,c] = ode45(@ode,zspan,cinf);

% try to plot in a way that's consistent with previous
definition of
% coordinates

z_series = fliplr((h - zs)');
c_series = fliplr(c');

% current density calculation
s.current = s.in.n*s.in.F*trapz(z_series,R(c_series))*1e3;
%mA/cm2

% return value
s.z_series = z_series;
s.c_series = c_series;


    function dc = ode(z,c)
        dc = -R(c)./qz(z);
    end

end
```

Diffusion included in all rotations (~/@profile/calc.m)

```
function calc(self)
% numerical solution of concentration profile
% automatically calculated when profile.in is changed.
% c in PRDE here is defined as the actual liquid phase
concentration, not
% the nominal concentraiton, which in this case shall be
porosity*c

    %% double entry at h
    h = self.in.h;
    zinf = self.zinf;
    xinit = ...
        [linspace(0,h,100) linspace(h,zinf,10)];
    % is multipoint BVP problem definition

    % inline definition, cannot be put after bvp4c!
    R = @(c) self.kinetics.rxn(c);

    % u = [c, c']
    solinit = bvpinit(xinit,[self.in.c_inf 0]);
    sol = bvp4c(@ode,@bc,solinit);
    self.sol = sol;

    %% post calculation analysis
    self.z_series = ...
            [linspace(0,self.in.h)...
            linspace(self.in.h+(self.zinf-
self.in.h)/100,self.zinf,20)];
        % why define
        % this way? Because later trapz(z,R) is used.
        % If linspace(0,zinf,100) was used, the
        % integration will take different resolution
        % in z = [0 in.h], thus leading to different
        % result with varying zinf values. (a painful
        % finding in zinf justification process)

    % avoid warning
    warning('off');
    u = deval(sol,self.z_series);
    warning('on');
    self.c_series = u(1,:);
    self.cp_series = u(2,:);
```

```
    % output current
    zint = self.z_series(self.z_series <= self.in.h);
    cint = self.c_series(self.z_series <= self.in.h);
    self.current = ...
        self.in.n*self.in.F*trapz(zint,R(cint))*1e3; %mA/cm2

    %% function def

    function dudz = ode(z,u,region)
      c = u(1); dcdz = u(2);
      dudz(1) = dcdz;
      switch region
          case 1 % z in porous electrode
            dudz(2) = 1/self.Deff*self.in.porosity*(R(c)+...
                self.qz_porous(z)*dcdz);
          case 2 % z in electrolyte
            dudz(2) = 1/self.in.D*self.qz_electrolyte(z)*dcdz;
      end

    end

    function res = bc(uL,uR)
      res = [ uR(1,2) - self.in.c_inf
              uR(1,1) - uL(1,2)
              self.Deff*uL(2,1) - self.in.D*uL(2,2)
              uL(2,1)];
    end
end
```

A.3.6 Limiting current case calculation

Basic class definition (~/@lmtcal/lmtcal.m)

```
classdef lmtcal < handle
% Zero surface concentration case calculation (Limiting
Calculation)
%
% creation: s = lmtcal(a, Sc); s = lmtcal(a); s = lmtcal();
%
% ==== properties =====
% input:
% Sc - Schimidt number, a - surface suction parameter
% Sc = v/D, a = qz/sqrt(v*w)
%
% output:
% z_s - zeta series, c_s - concentration series, cp_s - c % %
%derivative series
% z = sqrt(w/v)*height, the dimensionless length
% c = C/C_inf, dimensionless concentration
% n - nondimensional mass transfer. = 1/Sc*cp_s(@surface);
% l - current 0.99c position
% l_prime - slope projected boundary layer
% H - current stuart object with velocity profile within
%solution.
% version - object version
%
% lvalid options:
% RelTolX - lvalid relevant zeta tolerance: s.RelTolX*s.zinf
% TolFun - c value tolerance
%
% ==== methods ====
% lvalid - recalculation of boundary layer. It will adjust
s.zinf to s.l
% once the calculation is done. Any change in input parameter
%value has to
% accompany the excution of this method.
%
% doPlot - plot concentration profile
%
% calc - numerical calc function, used in lvalid. Could also be
%used when
% you know a valid zinf
%
% version:
% lmtcal-1.0
% dependency:
```

```
% stuart-1

    properties
        %input
        Sc % Schmidt number
        % lvalid options
    end

    properties (Hidden)
        RelTolX = 10 % relative tolerance in lvalid
        TolFun = 1e-3 % function value tolerance
    end

    properties (SetAccess = protected)
        %output
        n % surface mass transfer rate
        l % 0.99c boundary layer thickness
        l_prime % slope boundary layer thickness
        H % stuart object
        zinfo % old value zinf, for listener

        % solution series
        z_s;
        c_s;
        cp_s;
    end

    properties (SetObservable, AbortSet)
        zinf % infinity place
        a % suction paramter
    end

    methods (Static)

    end

    methods
        % == constructor ==
        function s = lmtcal(a, Sc)
            if nargin < 2, Sc = 1000; end
            if nargin < 1, a = 0.1; end
            s.Sc = Sc;
            s.a = a;
            s.l = 1/Sc;
            s.zinf = s.l;
            s.zinfo = s.zinf;
            s.H = stuart(a,s.zinf);
```

```
            addlistener(s,'zinf','PostSet',@s.zinf_postset);
            addlistener(s,'a','PostSet',@s.a_postset);

            s.lvalid;
        end

        function zinf_postset(s,~,~)
            if s.zinf > s.zinfo
                s.H.zinf = s.zinf;
                s.H.calc;
                s.zinfo = s.zinf;
            end
        end

        function a_postset(s,~,~)
            s.H.a = s.a;
            s.H.calc;
        end

        function value = q(s,z)
            % axial velocity quick evaluation based on H
            value = interp1(s.H.z,s.H.H,z);
        end


        function lvalid(s)
            disp('validating zinf...');
            s.zinf = 1/s.Sc;
            options =
optimset('TolX',s.RelTolX*s.zinf,'TolFun',s.TolFun,...
                              'MaxFunEvals',20);
            fminbnd(@f,s.zinf,s.zinf*1000,options);

            s.zinf = s.l;
            s.calc;

            function value = f(zinf)
                s.zinf = zinf;
                s.calc;
                value = -s.l; %c0.99 l, negative to use
%fminsearch
            end
        end % lvalid

        function doPlot(s)
            figure;
            plot(s.z_s,s.c_s);
            xlabel('non-D distance');ylabel('non-D c');
```

```
            figure(gcf);
        end
    end
end
```

Numerical calculation (~/@lmtcal/calc.m)

```
function calc(s)
% Numerically calculate the concentration profile
%
% calculation
solinit = bvpinit(linspace(0,s.zinf,100),[1 1]);
sol = bvp4c(@ge,@bc,solinit);

% post-evaluation
z = linspace(0,s.zinf,10000);
u = deval(sol,z);

c = u(1,:);
cp = u(2,:);
[d id] = min(abs(c - 0.99));
s.l = z(id);

s.z_s = z;
s.c_s = c;
s.cp_s = cp;

s.n = 1/s.Sc*s.cp_s(1);
s.l_prime = 1/s.cp_s(1);

% governing eq
    function dudz = ge(z,u)
        dudz = [u(2)
                s.Sc*s.q(z)*u(2)];
    end

% boundary condition
    function res = bc(ua,ub)
        res = [ua(1)
               ub(1)-1];
    end

end % calc
```

A.3.7 Fitting execution (~/runfitting.m)

```
%% Diffusion/convection fitting to porous rotating disk
%electrode

%% Experimental value input
% In this section the low and high hyrogel loading experimental
%results
% were generated.
clear all;

xy_low = ...
[104.8883223    1.59459
156.9608066 1.72973
262.6798148 1.86486
368.2676141 2.02703
419.553289  2.13514
574.2301616 2.24324
731.4590703 2.35135
786.230384  2.35135
837.2168641 2.40541];

xy_high = ...
[50.818506  3.47085
103.999204  3.60538
206.106221  3.87444
314.0976398 4.27803
415.996816  4.76233
518.5776473 5.30045
622.5274503 5.70404
725.2626025 6.05381
835.8401388 6.26906
935.9989548 6.4574
1035.436555 6.59193];

%%
% fitstr is cell array containing parameter names to be fitted
fitstr = {'Ks','K_hydrogel','k','Vmax'};
initval = [9.96e-5, 0.81, 5.16e-11, 3.92e-7];

%%
% expfit is the class dealing with fitting.

% class instance creation
f_high = expfit(xy_high,fitstr,initval);
f_low = expfit(xy_low,fitstr,initval);
```

```
% call method expfit.fit to carry out the fitting procedure
%% high loading fitting
f_high.fit;

%% low loading fitting
f_low.fit;

%% Result demonstration
w_exp_high = xy_high(:,1);
curr_exp_high = xy_high(:,2);
w_exp_low = xy_low(:,1);
curr_exp_low = xy_low(:,2);

plot(sqrt(w_exp_high),curr_exp_high,'or',sqrt(w_exp_low),curr_ex
p_low,'ob',...

sqrt(f_high.w_s),f_high.curr_s,sqrt(f_low.w_s),f_low.curr_s);
xlabel('sqrt of rotation / s-1/2');
ylabel('current density / mA cm-2');
```

A.3.8 Parameter variation studies (~/paracalc.m)

```
% calculation of parameter effects on the final current based on
profile

%% initialization
h = profile; % creating profile calculator

%% potential effect

h.in.w = 10; % /s, control the rotation rate

E_series = linspace(0.45,0.6,40); % 0.55 is redox potential
i_series = zeros(size(E_series));

for i = 1:length(E_series)
    disp(['calc...' num2str(i) ' of '
num2str(length(E_series))]);
    h.in.E = E_series(i); % h calc is done too
    i_series(i) = h.current;
end

plot(E_series,i_series);

%% substrate concentration

h.in.w = 1; % /s, control rotation

c_inf_series = linspace(0,100e-6,20); % 0.55 is redox potential
i_series = zeros(size(c_inf_series));

for i = 1:length(c_inf_series)
    disp(['calc...' num2str(i) ' of '
num2str(length(c_inf_series))]);
    h.in.c_inf = c_inf_series(i); % h calc is done too
    i_series(i) = h.current;
end

plot(c_inf_series,i_series);

%% permeability effect


rot_series = linspace(2,35,20).^2; % rotation series
i_series = zeros(size(rot_series)); % current matrix predef

for i = 1:length(rot_series)
```

```
    disp(['calc...' num2str(i) ' of '
num2str(length(rot_series))]);
    h.in.w = rot_series(i);
    i_series(i) = h.current;
end

sq_rot_series = sqrt(rot_series); % sqrt of rotation for %
%plotting

plot(sq_rot_series,i_series);
```

A.3.9 Limiting current case table (~/lmttable.m)

```
Sc_s = logspace(2,5,15);
a_s = logspace(-5,-2,15);
r = ones(15,15);

% zinf for every Sc;
zinf0 = zeros(size(Sc_s));

m = lmtcal;

for i = 1:length(Sc_s)
    disp(['===== calculating i = ' num2str(i) '=======']);
    m.Sc = Sc_s(i);
    m.a = a_s(1);
    m.lvalid;
    zinf0(i) = m.zinf;
    r(i,1) = m.n;
    for j = 2:length(a_s)
        disp(['calculating j =' num2str(j)]);
        m.a = a_s(j);
        m.calc;
        r(i,j) = m.n;
    end
end

% normalize to a = 0;
m.a = 0;
for i = 1:length(Sc_s)
    m.Sc = Sc_s(i);
    m.lvalid;
    Sc_normf(i) = m.n; % normalization factor
end

for i = 1:15
```

```
    r_norm(i,:) = r(i,:)./Sc_normf(i,1);
end

save('lmttable2')
```

A.4 SOFC Cathode model

A.4.1 Input structure, base (~/inpbase.m)

```
classdef inpbase < handle
% version 2.1 - incorporated related data
% dedicated get method for sic
% ref: see "../data_source/"
% SSC-GDC is what we want to focus on

    properties
        % fitting parameters
        beta = 1; % time constant dispersion
        Rel = 2 % electrolyte resistance, used in handfit.m

        % Materials switch
        miec = 'SSC' % [*] = 'SSC' or 'LSCF'

        % ----- transport properties ------

        % Gas
        xinf = 0.2 % [*] unitless | volume fraction of oxygen in
%bulk | no ref

        % vacancy
        Dv = 1e-5 % cm2/s | MC vacancy diffusivity |
%Svensson1997:1e-4 to 1e-8
        Cinf = 1e-5 % mol/cm3, 1e-5 to 1e-7 | vacancy
%concentration | Svensson1997

        % electric
        smc = 1000 % S/cm | electrical conductivity in LSCF |
%Wang2003

        % reaction and interface
        r0 = 1e-10 % mol/cm2/s, reversible reaction rate,
%tentative value
        Ri = 0.25 % ohm cm2, contact resistance between GDC/SSC,
%Baumann2007
        Ci = 40e-6 % F/cm2, interfacial capacitance
```

```
        % geometries
        eic = 0.68 % ionic conductor volume fraction. From (1 -
%porosity)
        emc = 0.14 % mixed conductor volume fraction, from
%Nicholas draft
        amc = 2e4 % cm2/cm3, surface area. Nicholas2009
        aic = 2e4 % cm2/cm3, MC/IC interfacial area

        % length parameters for film model
        Lic = 10e-4 % cm, ionic conductor thickness
        Lmc = 10e-4 % cm, mixed conductor thickness
        Lgas = 20e-4 % cm, gas phase boundary layer thickness

        % parameters for porous electrode model
        L = 24e-4 % cm | cathode thickness | Nicholas2010

        % ------ constants -------
        % rxn and charge equivalent
        nv = 1 % vacancy rxn stoichiometry
        nelectron = 2 % electron rxn stoichiometry

        no = 1/2 % oxygen rxn stoichiometry
        zv = 2 % vacancy equivalent
        ze = -1 % electron equivalent

        % constants
        F = 96485 % C/mol, Faraday constant
        R = 8.314 % J/mol/K, gas constant
        T = 1000 % K, temperature
        P = 1e5 % Pa, atmophere pressure
    end

    properties (Dependent = true)
        Cg % [*] mol/cm3, gas bulk concentration
        Cgp % porous cathode gas concentration
        Dgp % porous cathode gas diffusivity
        egas % mixed conductor volume fraction

        Rct % LSCF surface charge transfer resistance, f(T)
        Dg % [*] cm2/s | gas diffusivity | Marrero1972
    end

    methods

        function V = get.Dg(s)
            % oxygen diffusivity
            V = 1.3e-5*s.T^1.724; % cm2/s
        end
```

```
        function V = get.Cg(s)
            % bulk gas concentration
            V = s.P/s.R/s.T*1e-6; % mol/cm3, 12 mM for air
        end

        function V = get.Rct(s)
            V = 10^(18518/s.T-16.65); % ohm cm2
        end

        function V = get.Cgp(s)
            V = s.Cg*s.egas;
        end

        function V = get.egas(s)
            V = 1 - s.emc - s.eic;
        end

        function V = get.Dgp(s)
            % Bruggman approximation
            V = s.Dg * s.egas^1.5;
        end


    end
end
```

A.4.2 Input parameter, with IC conductivity calculated from literature (~/inp.m)

```
classdef inp < inpbase
% fully loyal to literature

    properties(Dependent = true)
        sic % GDC Ionic conductor conductivity
    end

    methods
                %% dependent property definition
        function V = get.sic(s)
            V = 10^(-2602.54/s.T+1.517); % S/cm
        end
    end

end %classdef
```

A.4.3 Calculation of impedance at one frequency (~/onewbase.m)

```
classdef onewbase < handle
% interfacial capacitance and resistance
% results are dimensional

properties
    % input
    in % input structure
    fre = 1; % Hz, frequency

    % ===== output ======
    Z % ohm cm2, impedance

    % ===== reduced parameters =====
    i2 % struct for intermediate params, s.i22i3 is used to calc
%i3 from i2
       % i2 is used to reveal the internal relation between i3
%parameters
    i3 % struct for final nonD params

    % debugging purpose
    sol

    % handfitting
    handfitting = false; % control whether do handfitting
    sic = 0.0821
    Rct = 73.79;
    Dgp = 0.0634;
end

methods
    function s = onewbase()
        s.in = inph; % this cannot happen in default value
                    % since I need to refer to different set of
data
        s.param;
    end

    function param(s)

        % assign all input structure parameters locally
        % refer to inp.m for the list of parameters
        % calculation of i2 series

        names = fieldnames(s.in);
        for i = 1:length(names)
```

```
        % take all fields, including dependent variables in.
        eval([char(names(i)) '= s.in.' char(names(i)) ';']);
    end

    if s.handfitting
    sic = s.sic;
    Rct = s.Rct;
    Dgp = s.Dgp;
    end

    % derived parameters
    s.i2.mu1n = aic*L*L/eic/sic;

    s.i2.ct = L*L/Dv;
    s.i2.cr2 = 1/emc/Cinf;
    s.i2.cr3 = nv*amc*r0;



    s.i2.cn3 = aic*R*T/(zv*F)^2;



    s.i2.muer1 = (ze*F)^2*L/R/T;
    s.i2.muer2 = nelectron*amc*r0;



    s.i2.xt = L*L/Dg;
    s.i2.xr2 = 1/egas/Cg/xinf;
    s.i2.xr3 = no*amc*r0;

    s.i2.nt = Ci*Ri;
    s.i2.Ri = Ri;

    %s.i2.zz = L/smc;

    s.i2.nmodule = sqrt(1/Ri/Ri+(2*pi*s.fre*Ci)^2);

    % Z calculation
    s.i2.zz = L*R*T/ze/zv/F/F;
    s.i2.zmu2 = emc*Dv*Cinf;
    s.i2.zmu1 = eic*sic*R*T/(zv*F)^2;

    % calculation for i3
    s.i22i3;

end
```

```
function i22i3(s)
    names = fieldnames(s.i2);

    for i = 1:length(names)
        eval([char(names(i)) '= s.i2.' char(names(i)) ';']);
    end

    cr = ct*cr2*cr3;
    cn = ct*cr2*cn3;
    muer = muer1*muer2*s.in.L/s.in.smc;
    xr = xt*xr2*xr3;

    % the contents of i3 is defined here
    s.i3.mu1n = mu1n;
    s.i3.ct = ct;
    s.i3.cr = cr;
    s.i3.cn = cn;
    s.i3.muer = muer;
    s.i3.xt = xt;
    s.i3.xr = xr;
    s.i3.nt = nt;
    s.i3.Ri = Ri;
    s.i3.zz = zz;
    s.i3.zmu2 = zmu2;
    s.i3.zmu1 = zmu1;
end

function easy_param(s)
    % for quick calc to verify code.
    % it is the same as Gerisher type of curve
    s.i2.mu1n = 1e2;

    s.i2.ct = 1e2;
    s.i2.cr2 = 1;
    s.i2.cr3 = 1;

    s.i2.cn3 = 1;

    s.i2.muer1 = 1;
    s.i2.muer2 = 1;

    s.i2.xt = 1;
    s.i2.xr2 = 1;
    s.i2.xr3 = 1;

    % no RiCi
    s.i2.nt = 1e-3;
```

```
        s.i2.Ri = 1e-3;

        % calculation of final parameters
        s.i22i3;
    end

    function demo_param(s,type)
 % switch between different types to generate EIS curve
 % first generate the baseline, also reverse any change that may
 % have done before.
        s.param;

        switch type
            case 'gerisher'
            % parameter sets that's realisticly possible to have
                % Gerisher. Good as handfitting starting point.
                s.i2.ct = 100;
                s.i2.cr3 = .14e-5;
                s.i2.cn3 = 6e-9;
            case 'finite_v'
                s.i2.ct = 1;
        end

        s.i22i3;
    end


end

end % classdef
```

A.4.4 Genertion of electrical impedance spectroscopy (~/eis.m)

```
classdef eis < handle
% usage:
% m = eis; m.calc;
%
% for handfitting:
%
% m.h.in.[para_name] = [value]; m.h.param; m.calc;

    properties
        % input
        fre = logspace(-4,4,20) % frequency range to fit to
        verbose = false;
        % output
        Z % impedance
        h % one fre object handle
        Zreal
        Zimag
    end % properties

    methods

        function s = eis()
            s.h = gerisher;
        end

    function calc(s)
        s.Z = zeros(size(s.fre));
        for i = 1:length(s.fre)
            if s.verbose
            disp(['calc... ' num2str(i) ' of '
num2str(length(s.fre))]);
            end
            s.h.fre = s.fre(i);
            s.h.calc;
            s.Z(i) = s.h.Z;
        end

        % make sure the output Z
        s.Zreal = real(s.Z); s.Zimag = imag(s.Z);
    end % calc

    function plotz(s)
        % plot Zreal vs. Zimag

        subplot(2,1,1);
```

```
        plot(s.Zreal, s.Zimag);
        xlabel('real(Z) / ohm cm2');ylabel('-imag(Z) / ohm
cm2');
        axis equal;
        delta = (max(s.Zreal) - min(s.Zreal))/5;
        xmin = min(s.Zreal) - delta;
        xmax = max(s.Zreal) + delta;
        ymin = 0;
        ymax = max(s.Zimag) + delta;
        axis([xmin xmax ymin ymax]);
        set(gca,'FontSize',14);

        % plot frequency related info
        subplot(2,1,2);
        semilogx(s.fre,s.Zimag);
        xlabel('frequency / Hz'); ylabel('-Zimg');
        set(gca,'FontSize',14);

        figure(gcf);
    end % plotz

    end % methods

end % classdef
```

Comprehensive model including all transport and kinetic phenomena (~/comp.m)

```
classdef comp < base
% comprehensive model

    methods
        function calc(s)
        w = 2*pi*s.fre;
        mue0 = 1; % nonD potential modulation

        % nonD parameters passing from s.i3, to speed up calc
        mu1n = s.i3.mu1n;
        ct = s.i3.ct;
        cr = s.i3.cr;
        cn = s.i3.cn;
```

```
muer = s.i3.muer;
xt = s.i3.xt;
xr = s.i3.xr;
nt = s.i3.nt;
zz = s.i3.zz;
zmu1 = s.i3.zmu1;
zmu2 = s.i3.zmu2;
Ri = s.i3.Ri;

% solution
y = linspace(0,1);
solinit = bvpinit(y,[1 1 1 1 1 1 1 1]);
sol = bvp4c(@ge,@bc,solinit);

% post analysis
ys = linspace(0,1);
us = deval(sol,ys);
mu1_s = us(1,:);
mu1p_s = us(2,:);
mu2_s = us(3,:);
mu2p_s = us(4,:);
mue_s = us(5,:);
muep_s = us(6,:);
x_s = us(7,:);
xp_s = us(8,:);

Z = zz*mue0/(zmu2*mu2p_s(1)+zmu1*mu1p_s(1));

% impedance
s.Z = conj(Z);

% bvp def
function dudy = ge(y,u)
    % diff variable def
    mu1 = u(1);
    mu1p = u(2);
    mu2 = u(3);
    mu2p = u(4);
    mue = u(5);
    muep = u(6);
    x = u(7);
    xp = u(8);

    % dependent variable def
    c = mu2 + 2*mue;
    n = 1/s.in.Ri*(1+nt*1j*w)*(mu1-mu2);
    r = c+x/2;
```

```
            dudy = [mu1p % mu1
                    mu1n*n
                    mu2p % mu2
                    ct*1j*w*c + cr*r - cn*n
                    muep % mue
                    muer*r
                    xp % x
                    xt*1j*w*x+xr*r];

        end

        function res = bc(uL,uR)
            % def Left @ y = 0
            mu1L = uL(1); mu2L = uL(3); muepL = uL(6); xpL =
uL(8);
            % def Right @ y = L
            mu1pR = uR(2); mu2pR = uR(4); mueR = uR(5); xR =
uR(7);

            res = [mu1L % left
                   mu2L
                   muepL
                   xpL
                   mu1pR % right
                   mu2pR
                   mueR - mue0
                   xR];
        end
    end
    end

end % classdef
```

A.4.5 Limited MIEC conductivity and oxygen vacancy diffusivity (~/se.m)

```
classdef se < onewbase
    % electron conductivity limited + gerisher

    properties
        easycal = true

        % profile
        ys
        c_s
        cp_s
        mue_s
        muep_s

        % calculation inter resuls
        M
    end

    methods
        function s = se()
            s.in = inph;
            s.param;
        end

        function Z = calcZ(s)
            % Cathode only calculation
            mue0 = 1; % nonD potential modulation
            w = 2*pi*s.fre;
            cr = s.i3.cr;
            ct = s.i3.ct;
            beta = s.in.beta;
            cn = s.i3.cn;
            mu1n = s.i3.mu1n;
            muer = s.i3.muer;
            zz = s.i3.zz;
            zmu1 = s.i3.zmu1;
            zmu2 = s.i3.zmu2;

            % see labnote #6 p47 for K def
            K = (ct*(1j*w)^beta + (1+cn/mu1n)*muer + cr) / (1 +
cn/mu1n);



            if s.easycal
            % use matrix to calculate the response, see labnote
```

```
#6 p57  \
                Ks = sqrt(K);
                M = [(1-2*muer/K) (1-2*muer/K) 0 -2;
                      -muer/Ks muer/Ks 1 0;
                      (-Ks+2*muer/Ks)*exp(-Ks) (Ks-
2*muer/Ks)*exp(Ks) -2 0;
                      muer/K*exp(-Ks) muer/K*exp(Ks) 1 1];

                s.M = M;

                V = [0;0;0;mue0];

                A = M\V; % calculation of parameters

                % post analysis
                ys = linspace(0,1);
                c_s = A(1).*exp(-Ks.*ys) + A(2).*exp(Ks.*ys);
                cp_s = Ks.*(-A(1).*exp(-
Ks.*ys)+A(2).*exp(Ks.*ys));
                mue_s = muer./K.*c_s + A(3).*ys + A(4);
                muep_s = muer*(-A(1)/Ks.*exp(-Ks.*ys) +
A(2)/Ks*exp(Ks.*ys))+A(3);

            else

                % start solving
                y = linspace(0,1);
                solinit = bvpinit(y,[1 1 1 1]);
                sol = bvp4c(@ge,@bc,solinit);

                % post analysis
                ys = linspace(0,1);
                us = deval(sol,ys);
                c_s = us(1,:);
                cp_s = us(2,:);
                mue_s = us(3,:);
                muep_s = us(4,:);


            end %if

            s.ys = ys;
            s.c_s = c_s;
            s.cp_s = cp_s;
            s.mue_s = mue_s;
            s.muep_s = muep_s;

            Zt = zz*mue0/((zmu2+zmu1)*(cp_s(1)-2*muep_s(1)));
```

```
            Z = conj(Zt);


            % function def for numerical calc
             function dudy = ge(y,u)
                c = u(1);
                cp = u(2);
                mue = u(3);
                muep = u(4);

                dudy = [cp
                        c*K
                        muep
                        muer*c];
             end % ge

            function res = bc(uL,uR)
                res = [uL(1)-2*uL(3)
                       uL(4)
                       uR(2) - 2*uR(4)
                       uR(3) - mue0];
            end % bc
        end

        function calc(s)
            % use calc on top of calcZ to enable inheritance
modification
            % overload this method in inherited seq.m
            s.Z = s.calcZ;
        end % calc
    end% methods

end % classdef
```

A.4.6 *Constant phase element added at low infiltration (~/seq.m)*

```
classdef seq < se
    % se with constant phase element R/Q

    methods
        function calc(s)
            R1 = s.in.R1;
            Q1 = s.in.Q1;
            alpha = s.in.alpha;
            w = 2*pi*s.fre;

            Z_se = s.calcZ;

            % added R/Q element, conj to make it > 0
            Z_con_phase = conj(R1/(1+R1*Q1*(w*1j)^alpha));

            % sum up to get final Z
            s.Z = Z_se + Z_con_phase;
        end

    end

end % classdef
```

A.4.7 *Finite oxygen vacancy diffusivity (~/gerisher.m)*

```
classdef gerisher < onewbase
    % no R,C.

    methods
        function calc(s)

            mue0 = 1; % nonD potential modulation
            w = 2*pi*s.fre;
            cr = s.i3.cr;
            ct = s.i3.ct;
            beta = s.in.beta;
            cn = s.i3.cn;
            mu1n = s.i3.mu1n;
            zz = s.i3.zz;
            zmu1 = s.i3.zmu1;
            zmu2 = s.i3.zmu2;
```

```
            % start solving
            y = linspace(0,1);
            solinit = bvpinit(y,[1 1]);
            sol = bvp4c(@ge,@bc,solinit);

            % post analysis
            ys = linspace(0,1);
            us = deval(sol,ys);
            c_s = us(1,:);
            cp_s = us(2,:);

            Z = zz*mue0/((zmu2+zmu1)*cp_s(1));
            s.Z = conj(Z);

            function dudy = ge(y,u)
                c = u(1);
                cp = u(2);
                dudy = [cp
                        c*(cr+ct*(1j*w)^beta)/(1+cn/mu1n)];

            end

            function res = bc(uL,uR)
                res = [uL(1)-2*mue0
                       uR(2)];
            end
        end
    end

end %classdef
```

A.5 Figures

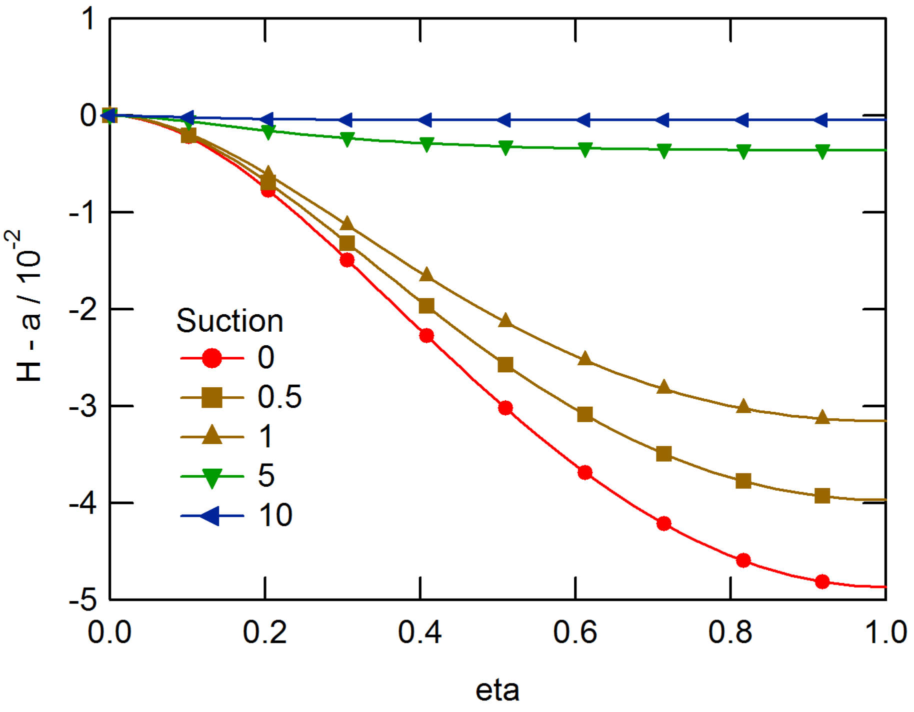

Figure A.1 Axial velocity with varying suction parameter *a* value from 0 to 10. The vertical axis is showing *(H – a)* for an easier comparison

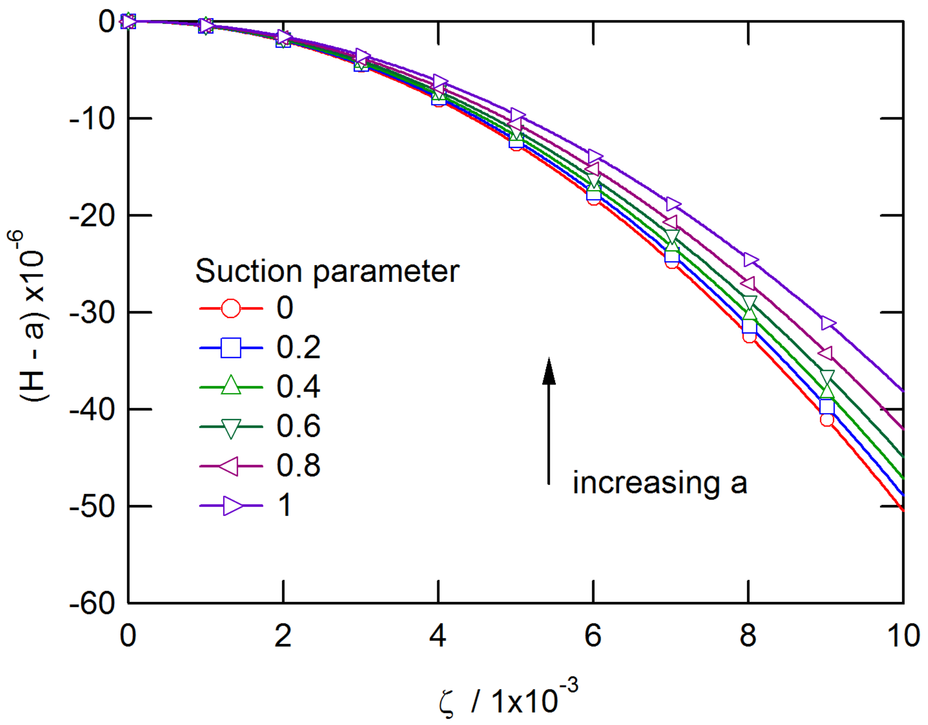

Figure A.2 Small distance eta (ζ) velocity profile with varying *a* from 0 to 1.

REFERENCES

References

1. J.T. Stuart, "On the effects of uniform suction on the steady flow due to a rotating disk" *The Quarterly Journal of Mechanics and Applied Mathematics*, **7**(4), 446-457 (1954).